Budapest University of Technology and Economics
Institute of Nuclear Techniques

Simulation of runaway electron dynamics in tokamak disruptions

Ph.D. Thesis

Author: Soma Olasz

Supervisor: Dr. Gergő Pokol

Budapest

2025

Contents

Chapter 1

Introduction

The concept of utilizing the energy from nuclear reactions arose in the early 20th century. The first successful demonstrations of releasing nuclear energy exploited the splitting, or fission of unstable atomic nuclei in the form of the Chicago pile [1], the first artificial nuclear reactor and the atomic bomb [2]. The realization of these achievements was made possible by the existence of the chain reaction when the neutron generated during a fission reaction can be used to induce a subsequent reaction. This mechanism is routinely used in present-day nuclear reactors and makes the exploitation of fission more viable than fusion.

Nuclear fusion is the combination of two, usually light, atomic nuclei. The reaction can release energy if the reaction product has a smaller mass than the overall mass of the reactants. This generally happens for light elements. This has been first utilized in military use by developing the hydrogen bomb [3] in the 1950s. The development of commercial use of fusion for energy generation also started at the same time, first with the proposal of so-called pinch devices, where externally driven currents were used to compress the plasma to achieve fusion [4]. Two other concepts were also introduced, both of which are still relevant today. The tokamak was proposed in the USSR [5], while the stellarator concept was developed in the US [6]. Inertial confinement fusion followed soon after, first as an idea in the early 1960s [7] and proposed implementation in 1972 [8]. The development of fusion reactors for commercial utilization is still underway as the absence of the chain reaction makes the realization of fusion energy challenging compared to fission.

The fusion research of the European Union focuses on the realization of generating electricity from fusion following the tokamak concept due to its simplicity over the stellarator design. The demonstration of energy production from fusion is developed according to the European Roadmap for Fusion Energy [9] with short-, medium- and long-term term goals defined. Two major milestones given in the roadmap are the participation in the building and the exploitation of ITER (International Thermonuclear Experimental Reactor) [10], planned as the first reactor scale fusion machine and the planning and building of DEMO [11] as the first demonstration of fusion energy produced on the grid.

1.1 Nuclear Fusion

Nuclear fusion can happen when two nuclei collide and approach each other close enough that the attractive strong nuclear force can overcome the repelling Coulomb force. The length scale for this is around 10^{-15} m [12]. The reaction can result in either the release of energy, for some small nuclei, or requires energy input, in case of large nuclei.

The binding energy per nucleus of the different nuclei is shown in Figure 1.1. It represents the energy corresponding to the mass deficit of the nucleus compared to the sum of the mass of its constituent nucleons. In Figure 1.1 we can see a general trend of increasing binding energy per nucleus as we go for the heavier elements from hydrogen until the minimum of the curve located at iron. The combination of these smaller nuclei can result in nuclei with stronger binding energy as energy is released from the reaction equivalent to the mass difference between the reactants and the product. We can see the opposite trend on the heavier nucleus side of the graph. As we go from iron to the heavier elements, the binding energy decreases, meaning the nucleus is less tightly bound. Fusion of elements in this region hence requires the input of energy, while fission releases energy.

Another noteworthy aspect of Figure 1.1 is the more tightly bound nuclei in the low atomic mass region, such as helium, beryllium, carbon, or oxygen. These nuclei are outliers from the general trend of the isotopes, meaning that they are more stable than both their neighbours. Generating any of these elements through fusion produces more energy than it would for example producing lithium.

For generation of fusion energy, several reactions have been considered, each considering light nuclei [14].

$$^2\mathrm{D} + {}^3\mathrm{T} \rightarrow {}^4\mathrm{He} + \mathrm{n} + 17.59\ MeV, \tag{1.1}$$
$$^2\mathrm{D} + {}^3\mathrm{He} \rightarrow {}^4\mathrm{He} + \mathrm{p} + 18.35\ MeV, \tag{1.2}$$
$$^2\mathrm{D} + {}^2\mathrm{D} \rightarrow {}^3\mathrm{He} + \mathrm{n} + 3.27\ MeV, \tag{1.3}$$
$$^2\mathrm{D} + {}^2\mathrm{D} \rightarrow {}^3\mathrm{T} + \mathrm{p} + 4.03\ MeV \tag{1.4}$$

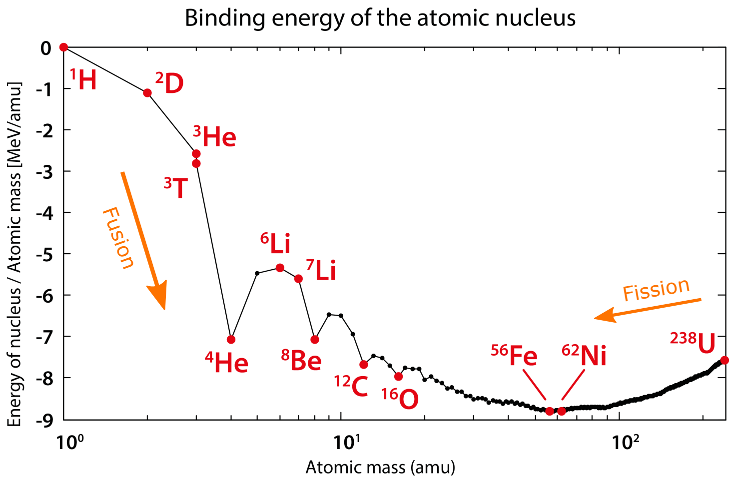

Figure 1.1: *The binding energy of the elements normalized to the atomic mass [13].*

The first two reactions are favourable in terms of the released energy, since the created ^{4}He is among the extremely tightly bound nuclei on Figure 1.1. These reactions however use tritium (^{3}H or T) or helium three (^{3}He or D) isotopes as fuel. Tritium is a radioactive isotope of hydrogen, with a half-life of 12.3 yrs, resulting in a limited supply readily available in reserve [15]. ^{3}He is also scarcely available on Earth [16], but significant reserves are available on the Lunar surface, generated by solar wind [17]. Deuterium (^{2}H) is abundantly available however, from the ocean where the ratio of deuterium to hydrogen is 1 : 6700 [18]. The deuterium-deuterium reactions are more favourable in terms of fuel availability but produce less energy. Another often investigated reaction is the proton-boron fusion [19]

$$p + {}^{11}\mathrm{B} \rightarrow 3{}^{4}\mathrm{He} + 8.7\ MeV, \tag{1.5}$$

because it produces only alpha particles and has no neutron radiation. This is a huge advantage over the D-T reaction, but the required plasma temperature is ten times of the temperature for the D-T reaction [20], which makes practical implementation challenging.

The probability of the various reactions in a medium in thermal equilibrium can be described by the rate coefficient, shown in Figure 1.2. We can see that the maximum probability of the various reactions is located at different temperatures, with reaction (1.1) having the maximum probability at the lowest temperatures, making it the most viable for controlled fusion. The temperature in the figure is measured in keV, where 1 eV = 11606 K. The necessary temperature for fusion reaction to occur is in the order of 10 keV or around 10^7 K.

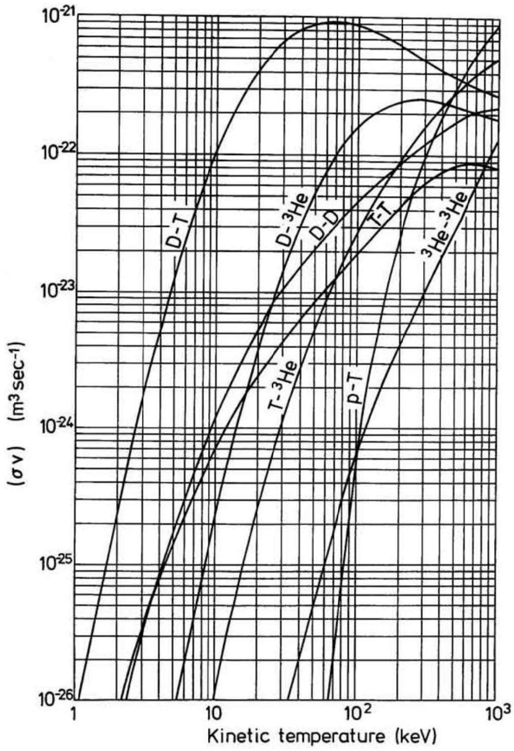

Figure 1.2: *The rate coefficient of the various reactions viable for fusion energy production. Note the logarithmic scales [21].*

The electron binding energy of the hydrogen isotopes in the proposed fusion reactions is in the order of 10 eV. The keV temperatures required for fusion reactions are enough to remove the bound electrons from around the atomic nuclei, meaning that the fusion fuel will be ionized. The ionized gas is called a plasma and it has to be contained in an isolated environment to achieve controlled fusion.

Another issue with reaction (1.1) is the lack of available tritium reserves. To achieve commercially viable fusion the available tritium reserves are insufficient [22], self-sufficiency in future fusion reactors is mandatory. Tritium can be generated from lithium atoms using neutrons as [23]

$$^{6}\mathrm{Li} + \mathrm{n}(thermal) \rightarrow {}^{4}\mathrm{He} + {}^{3}\mathrm{H} + 4.78\ MeV \tag{1.6}$$

$$^{7}\mathrm{Li} + \mathrm{n}(fast) \rightarrow {}^{4}\mathrm{He} + {}^{3}\mathrm{H} + \mathrm{n}(thermal) - 2.47\ MeV. \tag{1.7}$$

This is proposed to be used in so-called breeding blankets in future reactors [24, 25] using the neutron from the D-T reaction.

The criteria of a self-sustainable fusion reaction called burning, where the energy generated from fusion reactions is more than the energy losses is given by the Lawson criterion [26]. The Lawson criterion requires $n_e\tau_E \geq 1.5 \times 10^{20}$ sm^{-3} with n_e being the electron density and τ_e the energy confinement time and the ion temperature taken to be around $T_i = 25$ keV as the most optimal for reaction rates. This expression can be generalized with the removal of the temperature constraints to give the fusion triple product $n_eT_i\tau_E \geq 3 \times 10^{21}$ s keV m^{-3} to achieve ignition in power plants with ion temperature around ~ 20 keV [27].

Two separate concepts are being developed for reaching the ignition criterion relying on fundamentally different methods to generate favourable circumstances for fusion to occur. One is called inertial confinement fusion (ICF) which relies on achieving fusion by the compression of the D-T fuel using high energy lasers [8]. The necessary conditions are reached by the rapid compression and ignition of the fuel pellets [28, 29]. This approach aims to achieve the Lawson criterion by increasing the density.

The other, more explored concept utilizes the charged nature of the plasma state of the matter to confine the hot fuel in a magnetic field. This is referred to as magnetic confinement fusion (MCF). Charged particles experience the Lorentz force when they have a velocity component perpendicular to a magnetic field resulting in a helical motion around the magnetic field lines. MCF devices generate a magnetic geometry where the magnetic field lines connect inside the machine, hence confining the particles and preventing the collision of the hot plasma and the wall of the device. The approach of magnetic confinement aims to maximize the energy confinement time to reach the Lawson criterion with relatively small densities.

1.2 Magnetic confinement concepts

The two most used magnetic confinement concepts are the tokamak and the stellarator. Both machines generate magnetic fields in a toroidal geometry to confine the plasma, but there are some fundamental differences. A simple toroidal geometry can be achieved by taking a solenoid and connecting its two ends. The magnetic field created in such a way will not be homogeneous, however, as it was in a straight solenoid. The magnetic field is stronger on the inner side of the torus, due to the increased density of the magnetic field lines. The gradient and the curvature of the magnetic field generate an overall drift of the particles which results in an unstable plasma

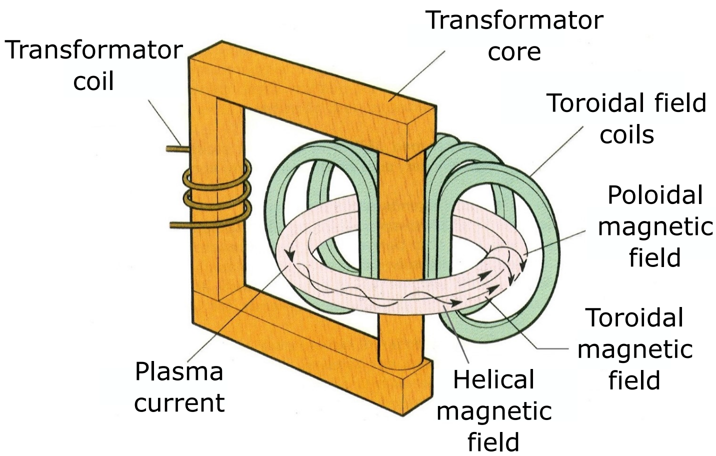

Figure 1.3: *The schematic view of the tokamak [31].*

state [30]. There are two major MCF devices depending on the method of dealing with this instability: the tokamak and the stellarator.

Tokamak Tokamaks use the technically simpler approach to stabilize the plasma. The lack of equilibrium in the plasma arises from the vertical charge separation of particles due to the ∇B and curvature drifts. The charge separation induces an electric field which exerts an $E \times B$ force on the plasma pushing it onto the tokamak wall. The simplest method to short-circuit the induced electric field is the twisting of the magnetic field lines. Connecting the top and the bottom of the plasma with the field lines enables particles to travel unhindered by the restrictive Lorentz force, hence eliminating the charge separation.

A tokamak achieves this, so-called helical magnetic field geometry, by inducing an additional toroidal current in the plasma, as shown in Figure 1.3. The plasma current generates a magnetic field around the plasma column, in the so-called poloidal direction. The toroidal component of the magnetic field is created by electromagnets, indicated with green in the figure. The superposition of the toroidal and poloidal field components is the desired helical field. The degree of twisting is described by the safety factor or q. In leading order it gives the number of toroidal rotations required for a poloidal turn.

The additional toroidal plasma current is most commonly induced in the tokamak using the transformer effect, using the plasma as the secondary coil. Plasmas are excellent conductors as they consist of charged particles. The resistivity of plasmas can be given by the so-called Spitzer resistivity [32]

$$\eta_S = \frac{m_e}{n_e e^2}\nu_{ei} \approx 0.51\frac{m_e^{1/2} e^2 \ln\Lambda}{3\varepsilon_0^2(2\pi T_e)^{3/2}} \tag{1.8}$$

with m_e being the electron mass, n_e the electron density, e the elementary charge, ν_{ei} the electron-ion collision frequency, $\ln\Lambda$ the Coulomb logarithm, ε_0 the vacuum permittivity and T_e the electron temperature in units of energy. The most notable feature of the Spitzer resistivity is the $T^{-3/2}$ temperature dependence causing the plasma to be a better conductor as temperature increases.

It can be shown that the magnetic induction lines are located on nested surfaces in the tokamak, called flux surfaces. The formation of the flux surface structure is caused by the toroidal symmetry and the $\nabla \cdot \vec{B} = 0$ requirement. The pressure, and consequetly the density and the temperature are equalized along these surfaces [33] since the particle transport along the magnetic field lines is unrestricted. The pressure gradient can be shown to be perpendicular to the magnetic field lines, $\nabla p \perp B$ and to the current density lines $\nabla p \perp J$, hence both the magnetic lines and the current lines run on nested surfaces. The transport perpendicular to the flux surfaces is significantly smaller than the parallel transport.

Stellarator Stellarators use a different approach to generate the magnetic geometry necessary to confine the fusion plasma. Instead of using the plasma to externally drive current to generate parts of the magnetic field required for confinement, stellarators use only external coils. A schematic picture of a stellarator is shown in Figure 1.4. The required magnetic field is generated using the toroidal magnetic field coils shown in red and the helical magnetic field coils in green. The resulting magnetic field is less symmetric compared to a tokamak.

Present-day stellarators, for example the Wendelstein 7-X [35], use a modular approach, where the helical and toroidal field coils are combined in effects to generate the necessary magnetic field. The design of such coils [36] is a challenging engineering problem and the accurate 3-D modeling of the plasma is required to ensure different requirements, such as nested flux surfaces, are met in the final device. The simplicity of the tokamak design compared to stellarators made them the more favoured MCF device concept in early fusion research. Stellarators have advantages over tokamaks, however, in other aspects, such as the lack of externally driven plasma current makes them more stable and they can be operated indefinitely in contrast to tokamaks where the necessity of the driving of plasma current limits operation time in most scenarios until the current in the central solenoid is driven up to its maxi-

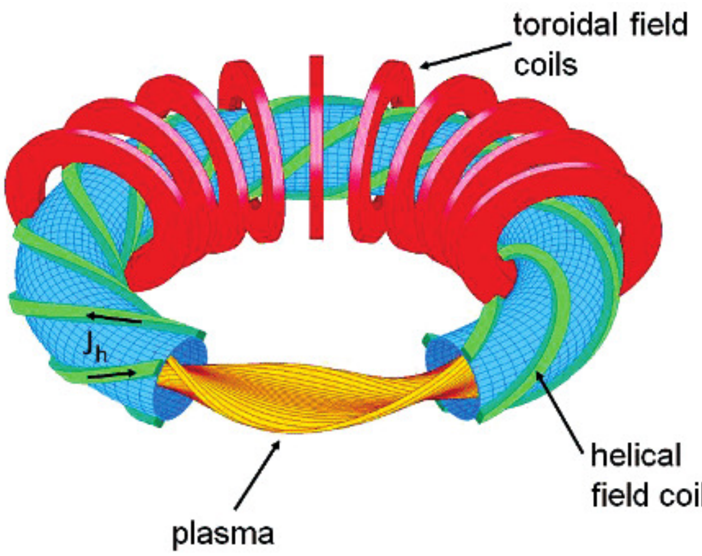

Figure 1.4: *The schematic view of the classical stellarator [34].*

mum. The lack of externally driven toroidal current means that significant runaway electron generation is not present in stellarators.

1.3 Thesis Outline

In this thesis, I introduce the work I have done in runaway electron modeling and integrated modeling focusing on the utilization of kinetic models. The aim of my PhD was to improve the integrated modeling of runaway electron dynamics and help the validation of models against experimental results and other codes. The work is structured as follows.

Chapter 2 gives the theoretical background of runaway electrons. It starts with the kinetic description of plasmas, with a focus on the collision dynamics between the plasma constituents. The derivation of a few collision operators is given and it is shown how the collision dynamics leads to the possibility of runaway electron generation. In Section 2.2 the various runaway electron generation methods are introduced and the main scenarios are described when runaway electron generation is a threat. The chapter ends with the introduction of runaway electron detection and mitigation methods.

Chapter 3 introduces the different runaway electron models used throughout this work, with a focus on the unique aspects of each code. I introduce two simple, so-called fluid models, Runaway Fluid and Runaway Indicator, used in integrated modeling workflow, the European Transport Simulator (ETS).

ETS is a simulation tool developed to couple different physical models in a single workflow to simulate full tokamak discharges. This approach of coupling different codes in a single program is called integrated modeling. The two different kinetic codes are introduced next, NORSE (NOn-linear Relativistic Solver for Electrons) is used in integrated modeling, while DREAM (Disruption and Runaway Electron Analysis Mode) is used for simulating self-consistent disruption scenarios. Finally, the SOFT (Synchrotron-detecting Orbit Following Toolkit) runaway electron radiation model is described.

Chapter 4 describes the results obtained with the codes described in Chapter 3. It features the development of a dedicated integrated modeling workflow and its use for studying runaway electron dynamics in rapidly varying parameters in Section 4.1. The development of integrated modeling with kinetic models is introduced and its use for simulation with experimental data is demonstrated in Section 4.2. Section 4.3 describes the utilization of the ETS workflow for disruption simulation with comparison against other integrated modeling results and experimental results and finally, the modeling of runaway electron radiation in the JT-60SA tokamak is described in Section 4.4.

Chapter 5 summarizes the results and the thesis statements are listed in Chapter 6.

Chapter 2

Runaway electron physics

The theoretical background for understanding runaway electron generation in plasmas is introduced in this chapter. First, the description of particle collisions in plasmas is derived starting from the introduction of single Coulomb collisions between charged particles and finishing with the relativistic collision operator describing the collision of relativistic particles with a Maxwellian background plasma. It is shown how these collision dynamics leads to the generation of runaway electrons. The derivation of the collision operators closely follows the derivation in the first three chapters of *Collisional transport in magnetized plasmas* by P. Helander and D. J. Sigmar [37]. Next, the main runaway electron generation methods are introduced. The chapter ends with introducing the main cases when runaway electron generation occurs, the different methods used for detecting them, and the mitigation methods used for minimizing the impact of these relativistic particles.

2.1 Kinetic plasma theory

The kinetic description of plasmas treats the plasma components statistically through distribution functions in the six-dimensional space for each plasma species f_a, where [37]

$$f_a(\mathbf{r}, \mathbf{v}, t) d^3r d^3v, \tag{2.1}$$

expresses the number of particles from species a in a given volume element d^3rd^3v at a given time t. The density of particles in real space can be found by integrating the distribution function over velocity

$$n_a(\mathbf{r}, t) = \int f_a(\mathbf{r}, \mathbf{v}, t) d^3v. \tag{2.2}$$

Plasmas consist of charged particles, as discussed in Section 1.1, hence the motion of particles is governed by the Lorentz force. The requirement of conservation of particles in phase space and the equation of motion gives the so-called Vlasov equation

$$\frac{\partial f_a}{\partial t} + \mathbf{v} \cdot \nabla f_a + \frac{q_a}{m_a}(\mathbf{E} + \mathbf{v} \times \mathbf{B}) \cdot \frac{\partial f_a}{\partial \mathbf{v}} = 0. \tag{2.3}$$

The first term describes the temporal evolution of the distribution function, the second term describes convection effects and the third term describes the change in the distribution due to the macroscopic electric and magnetic fields in the plasma – effectively the influence of the Lorentz force. As we will see later, plasma particles are only affected by fields and other particles on a characteristic length scale called the Debye length. The electric and magnetic fields on this length are greatly influenced by other particles, especially on lengths comparable to the Debye length. These small-scale fluctuations are the effects of collisions between particles, which are ignored in the Vlasov equation. The kinetic equation with the effects of collisions included is often called the Fokker-Planck equation

$$\frac{\partial f_a}{\partial t} + \mathbf{v} \cdot \nabla f_a + \frac{q_a}{m_a}(\mathbf{E} + \mathbf{v} \times \mathbf{B}) \cdot \frac{\partial f_a}{\partial \mathbf{v}} = C_a(f_a), \tag{2.4}$$

where $\mathbf{E}$ and $\mathbf{B}$ denote average fields over large length scales and $C_a(f_a)$ Fokker-Planck collision operator describes the effects of collisions on the distribution function f_a. Several requirements must be fulfilled by the collision operator [37]:

- Collisions must conserve density and only change the velocity of the participating particles.
- Momentum and energy conservation must be satisfied.
- The collisions described by C_a must drive the distribution functions towards the Maxwellian distribution and must vanish if the two particle populations are Maxwellians with identical mean velocity and temperature.

2.1.1 Coulomb collisions

To derive a suitable form of the collision operator we have to look at the collisional processes in plasmas. Plasmas are made up of charged particles, hence the interaction between the plasma species is dominantly governed by long-range Coulomb collisions. This is fundamentally different from collisions

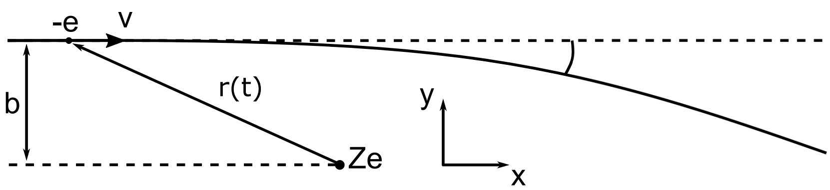

Figure 2.1: *The Coulomb collision. The Figure is based on Fig 1.1 in [37].*

in neutral gases as we know from the kinetic gas theory, where particles collide as solid bodies with small impact parameters. In plasmas, the long-range Coulomb force causes mostly small-angle collisions [37]. As seen in Figure 2.1 the distance between a charged ion with charge $e_i = Ze$ can be written as

$$r(t) = \sqrt{b^2 + v^2t^2}, \tag{2.5}$$

so the magnitude of the Coulomb force takes the form

$$\frac{e_i e}{4\pi\varepsilon_0 r^2(t)} = \frac{e_i e}{4\pi\varepsilon_0 (b^2 + v^2t^2)}. \tag{2.6}$$

We can calculate the vertical momentum change due to the Coulomb force as

$$\begin{aligned} m_e \Delta v_y &= \int_{-\infty}^{\infty} \frac{e_i e}{4\pi\varepsilon_0 (b^2 + v^2t^2)^{1/2}} \frac{b}{r(t)} dt \\ &= \frac{e_i e}{4\pi\varepsilon_0} \int_{-\infty}^{\infty} \frac{b}{(b^2 + v^2t^2)^{3/2}} dt \\ &= \frac{e_i e}{2\pi\varepsilon_0 b v} \end{aligned} \tag{2.7}$$

The deflection angle can be calculated from the initial velocity, $v = v_{Te}$ and the change in the vertical velocity

$$\alpha \approx \frac{\Delta v_y}{v} = \frac{e_i e}{2\pi\varepsilon_0 m_e b v_{Te}^2} = \frac{b_{min}}{b}, \tag{2.8}$$

where $b_{min} = \frac{e_i e}{2\pi\varepsilon_0 m_e v_{Te}^2}$ and in the approximation we have used that $\alpha \sim \tan\alpha$ for small angles, which is true for large b. The impact parameter can be estimated by finding the distance between the plasma particles where they start to 'feel' each other's Coulomb field.

The particles in the plasma will respond to the electric field of the other plasma constituents by slightly getting displaced towards oppositely charged particles and repulsed by the same charges. The electric field of an ion will be shielded by the surrounding electrons on large distances. This shielding process is called Debye shielding, and the characteristic length scale on which the resulting effective field of the ion vanishes is called the Debye length. It can be given as [32]

$$\lambda_D = \sqrt{\frac{\varepsilon_0 T}{ne^2}}, \tag{2.9}$$

where the temperature is measured in Joules. The Debye length can be used as the maximum distance where the particles can interact, so it is the maximum of the impact parameter b. On longer length scales the potential of the target particle is shielded from the colliding particle. Then, if we consider the possible impact parameters between the limits b_{min} and λ_D, we find that the collisions with large impact parameters dominate, in other words, small angle collisions are more frequent than large angle collisions [37].

We can define the plasma parameter Λ as the number of particles inside a square of sides equal to the Debye length,

$$\Lambda \equiv \frac{\lambda_D}{b_{min}} \sim n\lambda_D^3 \gg 1, \tag{2.10}$$

which can be shown to be much larger than unity in fusion plasmas [32]. When this is satisfied, large impact parameter collisions will dominate, and the deflection angle will be small.

The natural logarithm of the plasma parameter is the Coulomb logarithm, which will appear in the detailed description of collisions in plasmas. Since the plasma parameter is required to be much larger than unity for small angle collisions to be dominant, the Coulomb logarithm is also larger than unity. In fusion plasmas $\ln\Lambda$ generally has a value between 10 and 20 [32], showing that small angle collisions indeed dominate in tokamaks and stellarators.

2.1.2 The collision operator

With all this knowledge we can start the derivation of the collision operator in the Fokker-Planck equation (2.4). This operator is called the Fokker-Planck collision operator and is valid when small-angle collisions dominate. Since the velocity of the particles only gradually changes during collisions, we will see that the result is a diffusion in velocity space [37]. The derivation of the collision operators closely follows *Collisional transport in magnetized plasmas* by P. Helander and D. J. Sigmar [37]. The Einstein summation convention is used in the following derivation.

Let us consider a 1D plasma species with distribution denoted by $f(x, v, t)$ and the probability of suffering a collision which changes the velocity of one particle from v to $v + \Delta v$ in time Δt denoted by $F(v, \Delta v)$. We can then write the distribution function at time $t + \Delta t$ as

$$f(v, t + \Delta t) = \int f(v - \Delta v, t)F(v - \Delta v, \Delta v)d\Delta v, \tag{2.11}$$

with suppressed x dependence for simplicity. As we have shown in the previous sections, collisions dominantly result in small angle deflections, so Δv will peak around $\delta v = 0$ if Δt is small. Then we can expand $f(v - \Delta v, t)$ and $F(v - \Delta v, \Delta v)$ in $v - \Delta v$

$$\begin{aligned} f(v, t + \Delta t) = \int \Big(f(v, t)F(v, \Delta v) - \Delta v \frac{\partial f(v, t)F(v, \Delta v)}{\partial v} \\ + \frac{(\Delta v)^2}{2} \frac{\partial^2 f(v, t)F(v, \Delta v)}{\partial v^2} - \cdots \Big) d\Delta v. \end{aligned} \tag{2.12}$$

The sum of all probabilities equals 1

$$\int F(v, \Delta v)d\Delta v = 1, \tag{2.13}$$

and we can write the expectation values for Δv and Δv^2 as

$$\langle \Delta v \rangle = \int F(v, \Delta v)\Delta v d\Delta v, \tag{2.14}$$

$$\langle (\Delta v)^2 \rangle = \int F(v, \Delta v)(\Delta v)^2 d\Delta v. \tag{2.15}$$

Hence we can write the collision operator as

$$\begin{aligned} C(f) = \frac{\partial f(v, t)}{\partial t}\Big|_{collisions} = \lim_{\Delta t \to 0} \frac{f(v, t + \Delta t) - f(v, t)}{\Delta t} = \\ = -\frac{\partial}{\partial v}\left(\frac{\langle \Delta v \rangle}{\Delta t} f \right) + \frac{\partial^2}{\partial v^2}\left(\frac{\langle (\Delta v)^2 \rangle}{2\Delta t} f \right) - \cdots . \end{aligned} \tag{2.16}$$

The first term in the last part contains the average change of the distribution function in v while the second term is a diffusive term causing the distribution to spread out. It has a diffusion coefficient [37]

$$\frac{\langle (\Delta v)^2 \rangle}{2\Delta t} \frac{(stepsize)^2}{timestepsize}. \tag{2.17}$$

The three-dimensional generalization gives

$$C(f) = -\nabla_v \cdot \mathbf{j}, \tag{2.18}$$

where ∇_v is the divergence in velocity space and j can be written as

$$j_k^{ab} \equiv \frac{\langle \Delta v_k \rangle^{ab}}{\Delta t} f - \frac{\partial}{\partial v_l} \left(\frac{\langle \Delta v_k \Delta v_l \rangle^{ab}}{2\Delta t} f \right) \tag{2.19}$$

with the diffusion coefficient being replaced by the tensor $\langle \Delta v_k \Delta v_l \rangle / 2\Delta t$ and with summation over the index l.

The higher order terms have been neglected here as they are smaller by a factor of $1/\ln\Lambda$ where $\ln\Lambda$ is in the order of $10-20$ as mentioned at the end of the previous section. The first term here describes the drag force experienced by the particles due to collisions while the second term, as we have discussed, is a diffusive term spreading the particles in velocity space. The resultant distribution function tends towards a Maxwellian distribution function.

Plasmas generally have multiple species which all can collide with every other species. If we want to describe the effects of all the collisions on a distribution function we have to sum up the collisions between each species, in other words, the velocity space flux has to be written as

$$\mathbf{j}^a = \sum_b \mathbf{j}^{ab}, \tag{2.20}$$

where $\mathbf{j}^a$ represents the flux of species a due to collisions from all other species b, including themselves. [37]. The additive property of the flux means that the effects of collisions with multiple species can be added together in the collision operator

$$C_a(f_a) = \sum_b C_{ab}(f_a, f_b), \tag{2.21}$$

where $C_{ab}(f_a, f_b)$ represents the collisions of species a with species b.

The expectation value terms in Equation (2.19) can be written with the help of two tensors,

$$A_k^{ab} \equiv -\frac{\langle \Delta v_k \rangle^{ab}}{\Delta t} = \left(1 + \frac{m_a}{m_b}\right) L^{ab} \frac{\partial \varphi_b}{\partial v_k} \tag{2.22}$$

$$D_{kl}^{ab} \equiv \frac{\langle \Delta v_k \Delta v_l \rangle^{ab}}{2\Delta t} = -L^{ab} \frac{\partial^2 \psi_b}{\partial v_k \partial v_l}, \tag{2.23}$$

where the logarithmic factor L^{ab} is given as [38]

$$L^{ab} \equiv \left(\frac{e_a e_b}{m_a \varepsilon_0}\right)^2 \ln \Lambda, \tag{2.24}$$

and φ_b and ψ_b are the so-called Rosenbluth potentials [39] and are defined as

$$\varphi_b(\mathbf{v}) \equiv -\frac{1}{4\pi} \int \frac{1}{u} f_b(\mathbf{v}') d^3 v' \tag{2.25}$$

and

$$\psi_b(\mathbf{v}) \equiv -\frac{1}{8\pi} \int u f_b(\mathbf{v}') d^3 v', \tag{2.26}$$

where u is the relative velocity of the colliding particles.

The collision operator (2.18) then can be written in the form

$$C_{ab}(f_a, f_b) = \frac{\partial}{\partial v_k}\left[A_k^{ab} f_a + \frac{\partial}{\partial v_l}(D_{kl}^{ab} f_a)\right]. \tag{2.27}$$

The first term multiplied by the mass $-m_a A_k^{ab}$ is the average force felt by particles a when colliding with species b while the second term is a diffusion term with diffusion tensor of D_{kl}^{ab} [37]. The full derivation of the collision operator of this from can be found in [38].

It is useful to write a different form of the collision operator for the study of collisional dynamics with a Maxwellian background by using the relation between the Rosenbluth potentials

$$\nabla_v^2 \psi_b = \varphi_b. \tag{2.28}$$

to give the relation between A_k^{ab} and D_{kl}^{ab} as

$$A_k^{ab} = -\left(1 + \frac{m_a}{m_b}\right) \frac{\partial D_{kl}^{ab}}{\partial v_l}. \tag{2.29}$$

This allows us to write the collision operator directly with the Rosenbluth potentials

$$C_{ab}(f_a, f_b) = \ln \Lambda \left(\frac{e_a e_b}{m_a \varepsilon_0}\right)^2 \frac{\partial}{\partial v_k}\left(\frac{m_a}{m_b}\frac{\partial \varphi_b}{\partial v_k} f_a - \frac{\partial^2 \psi_b}{\partial v_k \partial v_l}\frac{\partial f_a}{\partial v_l}\right). \tag{2.30}$$

It can be shown that this form of the collision operator fulfills the requirements listed at the beginning of this chapter in Section 2.1. With this, we can move on to investigate the effects of particles colliding with a Maxwellian background and see how the runaway electron region arises in momentum space.

2.1.3 Collisions with a Maxwellian background

Let us start with the form of the collision operator derived last in the previous section, Equation (2.30). For this case, we take the target particle population f_b to be a Maxwellian at rest and thermal speed $v_{th} = \sqrt{2T_b/m_b}$. The temperature is measured in Joules throughout Chapter 2. Since the Maxwellian operator is isotropic the Rosenbluth potentials introduced earlier can only depend on the magnitude of the velocity and not on its direction [37]. This simplifies the collision operator since

$$\frac{\partial \varphi_b}{\partial v_k} = \frac{v_k}{v}\varphi_b' \tag{2.31}$$

and

$$\frac{\partial^2 \psi_b}{\partial v_l \partial v_l} = \frac{\partial^2 v}{\partial v_l \partial v_l}\psi_b' + \frac{v_k v_l}{v^2}\psi_b'' = W_{kl}\psi_b' + \frac{v_k v_l}{v^2}\psi_b'' \tag{2.32}$$

where $W_{kl} = (v^2\delta_{kl} - v_k v_l)/v^3$ and the prime denotes derivative of v. This allows the collision operator (2.30) to be written in the form

$$C_{ab}(f_a, f_{b0}) = L^{ab}\frac{\partial}{\partial v_k}\left[\frac{m_a}{m_b}\frac{v_k}{v}\varphi_b' f_a - \left(W_{kl}\psi_b' + \frac{v_k v_l}{v^2}\psi_b''\right)\frac{\partial f_a}{\partial v_l}\right], \tag{2.33}$$

where f_{b0} denotes the Maxwellian distribution. We can define the Lorentz operator for spherical coordinates in velocity space (v, θ, φ) as

$$\mathcal{L}(f_a) = \frac{1}{2}\left[\frac{1}{\sin\theta}\frac{\partial}{\partial\theta}\left(\sin\theta\frac{\partial f_a}{\partial\theta}\right) + \frac{1}{\sin^2\theta}\frac{\partial^2 f_a}{\partial\varphi^2}\right]. \tag{2.34}$$

It can be shown that the middle term in the collision operator can be written in terms of the Lorentz operator [37]

$$\frac{\partial}{\partial v_k}\left(W_{kl}\frac{\partial f_a}{\partial v_l}\right) = \frac{2}{v^3}\mathcal{L}(f_a), \tag{2.35}$$

and by using the formula for divergence on the vector relation

$$\nabla_v \cdot [\mathbf{A}(v)\mathbf{v}] = \frac{1}{v^2}\frac{\partial(v^3\mathbf{A})}{\partial v} \tag{2.36}$$

the collision operator can be written as

$$C_{ab}(f_a, f_{b0}) = -\frac{2L^{ab}}{v^3}\psi_b'\mathcal{L}(f_a) + \frac{L^{ab}}{v^2}\frac{\partial}{\partial v}\left[v^3\left(\frac{m_a}{m_b}\frac{\varphi_b'}{v}f_a - \frac{\psi''}{v}\frac{\partial f_a}{\partial v}\right)\right]. \tag{2.37}$$

The three different terms in this equation describe different physical responses to the collisions suffered by particles a. This can be highlighted by defining collision frequencies

$$\begin{aligned}
\nu_s^{ab}(v) &\equiv L^{ab}\left(1+\frac{m_a}{m_b}\right)\frac{\varphi_b'(v)}{v}, \\
\nu_D^{ab}(v) &\equiv -\frac{2L^{ab}}{v^3}\psi_b'(v), \\
\nu_\|^{ab}(v) &\equiv -2L^{ab}\frac{\psi_b''}{v^2},
\end{aligned} \tag{2.38}$$

where ν_s^{ab} is the slowing down frequency, ν_D^{ab} is the deflection frequency and $\nu_\|^{ab}$ is the parallel velocity diffusion frequency [37]. The introduction of these frequencies allows us to write the collision operator in the form

$$C_{ab}(f_a, f_{b0}) = \nu_D^{ab}\mathcal{L}(f_a) + \frac{1}{v^2}\frac{\partial}{\partial v}\left[v^3\left(\frac{m_a}{m_a+m_b}\nu_s^{ab}f_a + \frac{1}{2}\nu_\|^{ab}v\frac{\partial f_a}{\partial v}\right)\right]. \tag{2.39}$$

The different collision frequencies describe the rate of various physical processes caused by collisions with particle population b:

- *Slowing down frequency* Describes the rate at which the incoming particles are slowed down due to collisions.
- *Deflection frequency* Describes the rate at which the distribution function f_a becomes isotropic. The deflection frequency in the collision operator multiplies the Lorentz operator which only acts on the angular coordinates of the distribution function. It diffuses the particles on a sphere with constant v without changing the magnitude of the velocity.
- *Parallel velocity diffusion* Describes the diffusion rate of the particles parallel to their velocity vector.

Note that electrons are dominantly slowed down by collisions with other electrons, as seen from the collision operator (2.39). The slowing down term is multiplied by a factor of $m_a/(m_a+m_b)$ which results in a smaller slowing down term in the case of electron-ion collisions compared to electron-electron collisions. The physical reasoning for this is the large mass difference between ions and electrons does not change the magnitude of the velocity of the incoming electrons only its direction [37].

Next, we have to calculate the collision frequencies for a Maxwellian distribution. For this, we use the similarities between the electrostatic potential and the Rosenbluth potentials. The electrostatic potential Φ satisfies the Poisson equation

$$\nabla^2\Phi = -\frac{\rho}{\varepsilon_0} \tag{2.40}$$

with the solution for the potential being

$$\Phi(\mathbf{r}) = \int \frac{\rho(\mathbf{r}')}{4\pi\varepsilon_0|\mathbf{r}-\mathbf{r}'|}d^3r'. \tag{2.41}$$

Noticing the similarities between this and Equation (2.25) we can see that

$$\nabla_v^2\varphi_b = \frac{1}{v^2}\frac{\partial}{\partial v}\left(v^2\frac{\partial\varphi_b}{\partial v}\right) = f_b(v). \tag{2.42}$$

We can then integrate this equation for a Maxwellian distribution

$$f_{b0}(v) = \frac{n_b}{\pi^{3/2}v_{tb}^3}e^{-\frac{v}{v_{tb}}} \tag{2.43}$$

to get

$$\varphi_b'(v) = \frac{m_b n_b}{4\pi T_b}G(x_b), \tag{2.44}$$

where $x_b = v/v_{tb}$ is the velocity normalized to the thermal velocity of particle species b and n_b is the number density. $G(x_b)$ is the so-called Chandrasekhar function defined as

$$\begin{aligned} G(x) &\equiv \frac{\phi(x) - x\phi'(x)}{2x^2} \\ \phi(x) &\equiv \frac{2}{\sqrt{\pi}}\int_0^x e^{-y^2}dy \end{aligned} \tag{2.45}$$

where ϕ is the error function. The other Rosenbluth potential (2.26) can be found similarly from (2.28)

$$\nabla_v^2\psi_b = \frac{1}{v^2}\frac{\partial}{\partial v}\left(v^2\frac{\partial\psi_b}{\partial v}\right) = \varphi_b(v), \tag{2.46}$$

which when integrated gives

$$\psi_b'(v) = -\frac{n_b}{8\pi}[\phi(x_b) - G(x_b)]. \tag{2.47}$$

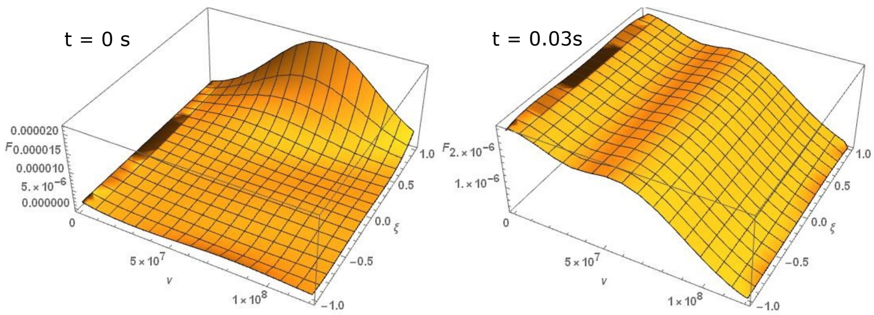

Figure 2.2: *The evolution of the electron distribution from Equation (2.39). The initial distribution is a Maxwellian distribution shifted along the parallel direction, as shown on the left. The distribution is plotted as a function of the magnitude of velocity and the pitch. The fastest process is the izotropization of the distribution function, as seen by the flattened curve along the ξ axis. The slowing down of the particle population is next, the peak of the distribution relocated to $v = 0$. The diffusion is the slowest process, as seen by the still present peak at the middle of the v axis.*

Substituting these back into the definitions for the various collision frequencies give

$$
\begin{aligned}
\nu_s^{ab}(v) &= \hat{\nu}_{ab}\frac{\phi(x_b) - G(x_b)}{x_a^3}, \\
\nu_D^{ab}(v) &= \hat{\nu}_{ab}\frac{2T_a}{T_b}\left(1 + \frac{m_b}{m_a}\right)\frac{G(x_b)}{x_a}, \\
\nu_\parallel^{ab}(v) &= 2\hat{\nu}_{ab}\frac{G(x_b)}{x_a^3}, \\
\hat{\nu}_{ab} &= \frac{n_b e_a^2 e_b^2 \ln\Lambda}{4\pi\varepsilon_0^2 m_a^2 v_{Ta}^3}
\end{aligned}
\tag{2.48}
$$

where $\hat{\nu}_{ab}$ is the basic collision frequency and $x_a = v/v_{Ta}$ similarly to x_b [37].

The three different collision frequencies affect the distribution function at different timescales. The fastest process for electrons is the isotropization of the population through the deflection of the particles. This can be seen in Figure 2.2. The figure shows the solution of Equation (2.39) I implemented in Mathematica. The Fokker-Planck equation was solved by expanding the distribution using Legendre polynomials as they are the eigenfunctions of the Lorentz operator (2.35). This has the advantage of decoupling the different collisional processes and enabling the investigation of the different timescales.

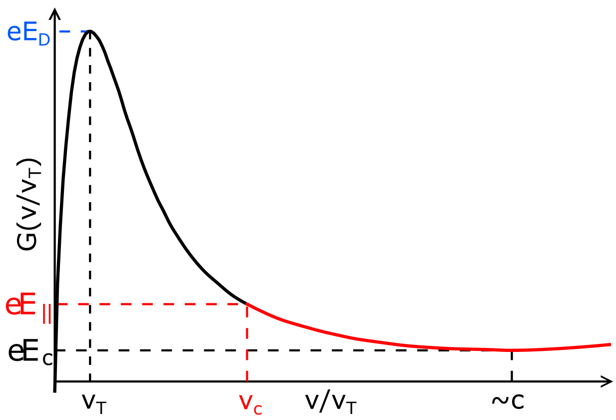

Figure 2.3: *The Chandrasekhar function has a maximum at thermal velocity and goes to a minimum at relativistic speeds. If an accelerating field is applied to the population, which is larger than the minimum field E_c, a region of the velocity space will be a runaway region, above a critical velocity v_c, where the particles can accelerate to high energies until relativistic effects intervene. The increase in the drag force at high velocities represents slowing down from additional effects, such as synchrotron and Bremsstrahlung radiation.*

Figure 2.2 shows an initial Maxwellian distribution function shifted in the parallel direction on the left, as indicated by the peak at $\xi = 1$ where $\xi = \cos\theta$, the cosine of the angle between the velocity vector and the magnetic field lines. After $t = 30$ ms the isotropization of the distribution function can be seen on the right panel, where the distribution function occupies the whole ξ range. The slowing down of the electron population has formed a peak in the distribution function to $v = 0$. The diffusion operates on a longer timescale as can be seen by the bump still present in the velocity v coordinate.

An interesting property of the Chandrasekhar function, shown in Figure 2.3 is found if we look at the function behaviour as $x \to 0$ and $x \to \infty$. In the small x limit it increases with the argument as $G(x) \to \frac{2x}{3\sqrt{\pi}}$ while in the large x limit it is proportional to the inverse of the argument squared $G(x) \to \frac{1}{2x^2}$. The maximum of $G(x_b)$ is found at $x_b = 1$, i.e. at thermal speeds. It decreases to a minimum at relativistic regions, where relativistic effects stop the particles from accelerating further.

An electric field which corresponds to the minimum value of the drag force at the speed of light is the minimum electric field required for runaway electron generation. A field lower than this so-called critical electric field E_c will not be larger than the drag force anywhere in the velocity space.

The critical electric field can be calculated as the friction force on electrons travelling at the speed of light [40]

$$E_c = \frac{n_e e^3 \ln \Lambda}{4\pi\varepsilon_0^2 m_e c^2}. \tag{2.49}$$

It was shown in practice often a larger electric field is required for runaway electron generation as the minimum value for the slowing down is increased by radiation and the primary runaway generation sources are sensitive to the temperature, as we will see later. This effective critical field can be three times as large as the critical field given above [41].

Another notable location on Figure 2.3 is the electric field corresponding to the maximum value of the drag force, indicated with E_D on the plot. Theoretically, if the electric field is larger than this E_D called the Dreicer field, then the whole velocity space becomes a runaway region where all the particles are accelerated to higher energies. In practice, it was shown that an electric field much lower than the Dreicer field is enough for this so-called slide-away [42], where all the electron population slides to a larger velocity. The Dreicer field can be calculated by equating the field to the maximum of the drag force

$$E_D = \frac{n_e e^2 \ln \Lambda}{4\pi\varepsilon_0^2 m_e v_{Te}^2}. \tag{2.50}$$

2.1.4 Linearized collision operator

The general collision operator derived previously is bilinear, meaning it satisfies [37]

$$\begin{aligned} C_{ab}(f_a + g_a, f_b) &= C_{ab}(f_a, f_b) + C_{ab}(g_a, f_b), \\ C_{ab}(f_a, f_b + g_b) &= C_{ab}(f_a, f_b) + C_{ab}(f_a, g_b), \\ C_{ab}(c_a f_a, c_b f_b) &= c_a c_b C_{ab}(f_a, f_b) \end{aligned} \tag{2.51}$$

for distribution functions f_a, f_b, g_a, g_b and constants c_a, c_b. These relations mean that for self-collisions the collision operator is non-linear, as

$$C_{aa}(2f_a) = C_{aa}(2f_a, 2f_a) = 4C_{aa}(f_a). \tag{2.52}$$

For distribution functions close to a Maxwellian,

$$f_a = f_{Ma} + f_{a1}, \tag{2.53}$$

where $f_{a1} \ll f_{Ma}$, the collision operator can be linearized for self-collisions

$$\begin{aligned} C_{aa}(f_a) &= C_{aa}(f_{Ma} + f_{a1}, f_{Ma} + f_{a1}) \\ &\simeq C_{aa}(f_{a1}, f_{Ma}) + C_{aa}(f_{Ma}, f_{a1}) \equiv C^l_{aa}(f_a), \end{aligned} \tag{2.54}$$

where the term $C_{aa}(f_{a1}, f_{a1})$ was neglected and $C_{aa}(f_{Ma}, f_{Ma}) = 0$ by definition. $C^l_{aa}(f_a)$ is the linearized collision operator for self-collisions and is valid for plasmas in near thermal equilibrium. It can be generalized for collisions between arbitrary species to give

$$C^l_{ab}(f_a, f_b) \equiv C_{ab}(f_{a1}, f_{b0}) + C_{ab}(f_{a0}, f_{b1}), \tag{2.55}$$

where f_{a0}, f_{b0} are Maxwellians for species a and b with the same flow velocity and temperature, to have $C_{ab}(f_{a0}, f_{b0})$ vanish. The linearized collision operator is often useful in kinetic models where the collisional dynamics are calculated for thermal plasmas.

2.1.5 Relativistic collision operator

So far we have neglected the relativistic effects when considering collisions between particles, but runaway electrons cannot be treated without considering relativity. Runaway electrons can reach several MeV energies in larger devices, so relativistic treatment is necessary. The derivation of the non-relativistic collision operator showed the existence of the runaway region due to the collisional dynamics, and many of the derivation steps will be used in the following derivation. To derive the relativistic collision operator we have to consider a very fast particle population a colliding with a much slower background plasma species b [37].

Let us start by writing the initial momentum and energy of the incoming particle

$$\begin{aligned} p = p_x &= \gamma m_a v \\ E_a &= \gamma m_a c^2 = \sqrt{m_a^2 c^4 + p^2 c^2} \end{aligned} \tag{2.56}$$

where m_a is the rest mass and relativistic mass factor is $\gamma = \sqrt{1 - v^2/c^2}$. The target particle has an initial energy

$$E_b = m_b c^2. \tag{2.57}$$

We can then write the post-collision energies for the two particles as

$$
\begin{aligned}
E_a' &= \sqrt{m_a^2 c^4 + (p_x + \Delta p_x)^2 c^2 + (\Delta p_\perp)^2 c^2}, \\
E_b' &= \sqrt{m_b^2 c^4 + (\Delta p_x)^2 c^2 + (\Delta p_\perp)^2 c^2},
\end{aligned}
\tag{2.58}
$$

with Δp_x and $\Delta p_\perp$ being the momenta exchanged in the collision in the parallel and perpendicular direction respectively. Let us consider cases where small momentum exchange occurs, we can then use the approximation $\sqrt{1+\epsilon} \simeq 1 + \epsilon/2$ to write

$$
\begin{aligned}
E_a' &= E_a \left(1 + \frac{2 p_x \Delta p_x + (\Delta p_\perp)^2}{2 E_a^2} c^2 \right), \\
E_b' &= E_b \left(1 + \frac{(\Delta p_x)^2 + (\Delta p_\perp)^2}{2 E_b^2} c^2 \right).
\end{aligned}
\tag{2.59}
$$

It can be shown that the parallel momentum exchange is much smaller in small-angle collisions than the perpendicular if we consider the energy conservation

$$
E_a' - E_a + E_b' - E_b = 0 \tag{2.60}
$$

and we neglect the parallel term in E_b we get

$$
\Delta p_x = -\left(1 + \frac{E_a}{E_b} \right) \frac{(\Delta p_{\perp)})^2}{2 p_x} \tag{2.61}
$$

which is much smaller if $\Delta p_\perp \ll p_x$.

The total resulting momentum change of particle a due to collisions with species b can be given as

$$
\begin{aligned}
\frac{\langle \Delta p_x \rangle^{ab}}{\Delta t} &= -\left(1 + \frac{E_a}{E_b} \right) \frac{m_a^2 c^3}{p_x v \hat{\tau}_{ab}} \\
\frac{\langle (\Delta p_\perp)^2 \rangle^{ab}}{\Delta t} &= \left(\frac{e_a e_b}{2 \pi \varepsilon_0 v} \right)^2 \int_{b_{min}}^{\lambda_D} \frac{n_b 2 \pi v db}{b} = \frac{2 m_a^2 c^3}{v \hat{\tau}_{ab}},
\end{aligned}
\tag{2.62}
$$

where $n_b v 2\pi b db$ is the number of collisions in unit time with impact parameter between b and $b + db$ and $\hat{\tau}_{ab}$ being the collision time at the speed of light

$$
\hat{\tau}_{ab} = \frac{4 \pi \varepsilon_0^2 m_a^2 c^3}{n_b e_a^2 e_b^2 \ln \Lambda}. \tag{2.63}
$$

Next, we have to transform the expectation values from a coordinate system aligned with the initial velocity to an arbitrary frame of reference, which results in

$$\begin{aligned}\frac{\langle \Delta p_k \rangle^{ab}}{\Delta t} &= -\left(1 + \frac{E_a}{E_b}\right) \frac{\gamma (m_a c)^3}{\hat{\tau}_{ab}} \frac{p_k}{p^3} \\ \frac{\langle (\Delta p_k \Delta p_l \rangle^{ab}}{\Delta t} &= \frac{\gamma (m_a c)^3}{\hat{\tau}_{ab}} P_{kl},\end{aligned} \tag{2.64}$$

with the introduction of the tensor

$$P_{kl} = \frac{p^2 \delta_{kl} - p_k p_l}{p^3} \tag{2.65}$$

and using that $p = \gamma m_a v$. With this, we can write down the relativistic collision operator (2.18)

$$\begin{aligned}C_{ab}(f_a) &= \frac{(m_a c)^3}{\hat{\tau}_{ab}} \frac{\partial}{\partial p_k} \left[\left(1 + \frac{E_a}{E_b}\right) \frac{\gamma p_k f_a}{p^3} + \frac{\partial}{\partial p_l} \left(\frac{\gamma P_{kl} f_a}{2} \right) \right] \\ &= \frac{(m_a c)^3}{\hat{\tau}_{ab}} \frac{\partial}{\partial p_k} \left(\frac{m_a}{m_b} \frac{\gamma^2 p_k f_a}{p^3} + \frac{P_{kl}}{2} \frac{\partial (\gamma f_a)}{\partial p_l} \right),\end{aligned} \tag{2.66}$$

where we have used that $\partial P_{kl} / \partial p_l = -2 p_k / p^3$.

Lastly, we can write the last term in the second line of the last equation in terms of the Lorentz operator similarly to (2.35) to get

$$C_{ab}(f_a) = \frac{(m_a c)^3}{\hat{\tau}_{ab}} \left[\frac{m_a}{m_b p^2} \frac{\partial}{\partial p} \left(\gamma^2 f_a\right) + \frac{\gamma}{p^3} \mathcal{L}(f_a) \right], \tag{2.67}$$

where $\gamma = \sqrt{1 + p^2 / m_a^2 c^2}$.

The first term in this collision operator corresponds to the slowing down of the fast particles due to collisions. The ratio of the masses of the colliding particles again appears in this term, meaning that fast electrons mainly slow down due to collisions with other electrons, as seen for the non-relativistic case. In the non-relativistic limit $\gamma = 1$ and $p = m_a v$ this term tends to our earlier results, but the relativistic friction force does not approach zero as did the Chandrasekhar function in the previous case. The second term corresponds to the angle scattering of the fast electrons through the Lorentz operator. This term also reproduces the non-relativistic case on low particle energies, while in the ultra-relativistic limit, it disappears. Physically this can be explained by the increased inertia of the incident particle due to the relativistic mass effect, resulting in larger force required to deflect the fast particles [37].

2.2 Runaway generation methods

Runaway electrons can be produced in various ways. We can characterize these methods into two different categories:

- **Primary generation** Primary generation methods are independent of the runaway electron population
- **Secondary generation** Secondary generation requires previously generated runaway electrons to be present.

We can distinguish four different primary generation methods, separated into non-nuclear and nuclear sources and a single secondary generation method.

2.2.1 Primary generation

Dreicer generation

The Dreicer generation was first described by H. Dreicer in 1959 [43] and 1960 in subsequent papers [44]. The Dreicer generation physically can be understood in the following way: when an electric field is applied to an electron population in a plasma it creates a region in velocity space where the collisional drag force cannot overcome the acceleration from the said electric field, given that it is larger than the critical electric field (2.49), see Figure 2.3. The part of the electron distribution function, which is located in the so-called runaway electron region is constantly accelerated resulting in a depletion of particles in velocity space at the boundary defined by the critical velocity v_c. This depletion is balanced by a diffusion into the runaway region, providing a steady generation of runaway electrons.

The Dreicer generation rate can be given by the formula derived in [40]

$$\gamma_D = \frac{Cn_e}{\hat{\tau}_{ee}}\left(\frac{E}{E_D}\right)^{-3/16(1+Z_{eff})h} \exp\left[-\lambda\frac{E_D}{4E} - \sqrt{\eta\frac{(1+Z_{eff})E_D}{E}}\right], \quad (2.68)$$

where $\hat{\tau}_{ee}$ is the runaway electron collision time (2.63), $Z_{eff} = \sum_i n_i Z_i/n_e$ is the effective charge of the plasma, C is a factor in the order of unity and the different factors appearing are

$$
\begin{aligned}
h &= \frac{1}{3}\frac{1}{\frac{E}{E_c}-1}\left[\frac{E}{E_c}+2\left(\frac{E}{E_c}-2\right)\sqrt{\frac{E}{E-E_c}}-\frac{Z_{eff}-7}{Z_{eff}+1}\right],\\
\lambda &= 8\frac{E^2}{E_c^2}\left[1-\frac{E_c}{2E}-\sqrt{1-\frac{E_c}{E}}\right],\\
\eta &= \frac{1}{4}\frac{E^2}{E_c(E-E_c)}\left[\frac{\pi}{2}-\arcsin\left(1-\frac{2E_c}{E}\right)\right]^2.
\end{aligned}
\tag{2.69}
$$

The Dreicer generation rate (2.68) is valid in steady-state plasmas where the different plasma parameters, such as density n_e, temperature T and electric field E are changing slowly. This is useful in so-called fluid modelling where the kinetic equation is not solved to calculate the electron distribution function, only "fluid-like" plasma parameters, such as n, T, and current density j are used to calculate the runaway electron generation rate. Note that the Dreicer generation is strongly dependent on the electron temperature through the Dreicer field E_D in the exponential factor.

It also misses several important aspects which can change the generation rate significantly. The Coulomb logarithm was taken to be constant when (2.68) was derived, but it was later shown that an energy dependent Coulomb logarithm has to be introduced when considering relativistic particles colliding with a thermal population at low temperatures [45, 46]. The presence of high-Z impurities can also change the generation rate by orders of magnitude due to the effect of partial screening. Partial screening is the phenomenon where partially ionized ions are present in the plasma and the bound electron layers shield the charge of the ion. Collisions heavily depend on the charge of participating particles and, since energetic electrons can penetrate the bound electron layers to some extent, it was shown that the extent of the penetration can significantly impact runaway electron dynamics [46]

To address these effects a neural network was trained on kinetic simulations to provide a more robust tool for fluid like Dreicer generation calculations [47]. The neural network has been shown to produce accurate results when high-Z impurities are present in the plasma and is routinely used in one of the simulation tools I used during my PhD studies.

Hot-tail generation

Hot-tail generation is an intrinsically transient process. It can occur in tokamaks when the plasma rapidly cools due to some instability. As I have shown in Equation (2.48) the collision frequency for particles faster than the thermal speed is smaller than that of the thermal population. In a scenario where the plasma experiences rapid cooling the high energy population of the electron distribution function will take longer to thermalize to the new temperature since thermalization occurs through collisions. As we saw in Section 1.2, plasma resistance increases as temperature drops causing current decay, and the changing current generates changing magnetic flux, which induces electric field through Fraday's law. The electric field is often large enough that a runaway electron region will be defined in velocity space which can overlap with the high energy tail of the pre-cooling Maxwellian. This will result in a large portion of the electron population finding itself running away [48, 38, 49].

Hot-tail generation is expected to be the dominant seed generation mechanism in future devices like ITER [50, 51] in so-called disruption scenarios, where the plasma rapidly cools due to radiation or instabilities, as described above. An analytical formula for hot-tail generation has been derived by H. Smith and E Verwichte [50], but it generally underestimates the runaway electron population from the hot-tail source. Due to the transient nature of this generation, it is usually calculated kinetically in simulations, by solving the Fokker-Planck equation (2.4).

Compton scattering

Compton scattering and tritium decay sources are considered nuclear sources of runaway electron generation. In currently operating devices the plasma is generated from deuterium without the addition of tritium - one machine capable of deuterium-tritium plasmas was JET [52] - and in such experiments the nuclear runaway electron generation is not present. When tritium is added to the plasma, however, high energy neutrons are generated from the fusion reaction (1.1) which can activate the plasma-facing components of the tokamak. These components generate high energy γ rays which can give electrons enough energy through Compton scattering to push them into the runaway region. The neutrons can also produce high energy photons, with energies in the MeV range, with a two step process, where the neutron is captured by the atomic nuclei, producing an excited state, which generates a photon when de-excited [53].

The runaway electron generation rate from Compton scattering can be calculated as [51]

$$\left.\frac{dn_r}{dt}\right|_{Compton} = n_e \int \Gamma_\gamma(E_\gamma)\sigma(E_\gamma)dE_\gamma, \tag{2.70}$$

where E_γ is the photon energy, Γ_γ is the gamma energy flux spectrum and σ is the Compton cross-section.

Tritium decay

Adding tritium to the plasma provides another runaway electron generation method besides Compton scattering of γ photons from the activated wall. Tritium decay occurs with a half-life of $t_{1/2} = 12.32$ years according to the reaction

$$^3\mathrm{H} \rightarrow ^3\mathrm{He} + \mathrm{e}^- + \bar{\nu}_\mathrm{e}, \tag{2.71}$$

producing an ^{3}He particle, and electron and an electron antineutrino and 18.6 keV energy released. The electron energy gained in the process can be sufficient to generate a runaway electron immediately. Since the electron energy is small, this process requires large electric field compared to other generation methods, but it can be occur in disruptions in large tokamaks.

The main problem with the nuclear sources is that they are independent of the plasma parameters and they cannot be suppressed and mitigated as the Dreicer and hot-tail sources. As we will see, the main source of runaway electrons is the avalanche generation, but it requires a runaway electron seed to be present from a primary source. In future reactors, where deuterium-tritium plasmas will be generated, runaway electron suppression might be impossible.

2.2.2 Secondary generation

Runaway electron generation in larger, high current tokamaks poses extreme risk because of the the avalanche generation. This can exponentially grow the runaway electron population and is heavily dependent on the tokamak current [54].

Avalanche generation is when runaway electrons already collide with the thermal population and provide enough energy to the slower electrons to push them into the runaway region. Hence the avalanche generation is proportional to the runaway electron population. The generation rate can be given as

$$\Gamma_A \equiv \frac{1}{n_r}\frac{\partial n_r}{\partial t} = \frac{1}{2\hat{\tau}_{ee}\ln\Lambda}\left(\frac{E}{E_c - 1}\right), \tag{2.72}$$

where n_r is the runaway electron density and $\hat{\tau}_{ee}$ is the collision time with the speed of light, (2.63), for electron-electron collisions.

The collisions resulting in the avalanching of the runaway electron populations cannot be described by the Fokker-Planck operator (2.4). During the derivation of the collision operator, we have used the fact that most collisions result in small angle deflections in velocity space, in other words, the velocities of the participating particles do not change significantly. This is not true for the secondary generation method as it can be seen from the physical description above. Kinetic description of the avalanche generation hence requires the consideration of large angle collisions [48, 55].

2.3 Runaway generation scenarios

Runaway electrons are typically generated in tokamaks when normal operation is disrupted. In steady tokamak discharges usually negligible runaway electron population is present [56], unless dedicated low-density discharges are carried out to study runaway electrons [57, 58]. There are two distinct phases in tokamak operation when runaway electron generation is a risk: at tokamak start-up and at the termination of the discharge.

The formation of a tokamak plasma requires sufficient ionization of the hydrogen and the ramp-up of the plasma current to form the necessary magnetic geometry. This is achieved in different phases generally called tokamak start-up. First, the plasma breakdown starts the ionization by inducing an electron avalanche through an applied electric field [59]. In this phase, the plasma has low ionization so the magnetic surfaces are not formed, and transport losses are dominant. The next phase is the burn-through phase where the transport and radiation losses are balanced by excessive heating, both auxiliary and ohmic heating, to continue the full ionization of the plasma. The plasma current ramp up is next, and it can be effectively achieved by applying an electric field. The magnetic surfaces are formed as the plasma current is increased, hence the transport losses are diminished [60].

The start-up of a tokamak has a few characteristics which are favourable for runaway electron generation, such as low density and potentially high electric fields. The friction force experienced by electrons (2.48) and consequently the critical field (2.49) is proportional to the density, hence low density enables easier runaway electron generation. The low plasma density can mostly be experienced in the burn-through phase, when the full ionization is not yet achieved. If a runaway electron seed is generated, and not lost during this phase, it can easily be multiplied when the current ramp up is initiated.

The dominant generation forms during the tokamak start-up are the Dreicer generation and the avalanche generation. Hot-tail generation is negligible since no rapid cooling is happening. Dreicer generation is sensitive to temperature, but it can provide a sufficient seed for large avalanche generation due to the strong applied electric field in the ramp up phase. Given these circumstances, without a proper understanding of the tokamak start-up process generating runaway electron dominated discharges was a risk in early devices.

The simulation of start-up runaway electron generation has gotten more focus recently, as it was shown that in future large-scale tokamaks, the process of creating the plasma can differ significantly from current devices [61, 62].

The other typical runaway electron generation regime in tokamak operation can occur at the end of the plasma. If, due to some instabilities, the confinement and the flux surface structure breaks and the plasma loses its energy rapidly, the environment can easily turn favourable for runaway processes. This sudden termination of a tokamak plasma is referred to as disruption.

Disruptions occur when the plasma temperature drops on a millisecond timescale. The drop in temperature results in increased plasma resistance (see Equation (1.8)) and decreasing plasma current. The electric field induced by the drop in plasma current can be sufficiently large to generate runaway electrons, in unmitigated disruptions a significant portion of the original plasma current can transform into runaway electron current [63]. This runaway beam can cause serious damage to the plasma-facing components even penetrate the tokamak wall and puncture the cooling pipes inside the first wall [64, 65]. The lack of net toroidal plasma current in a stellarator-type device means that runaway electron generation is not a problem during stellarator operation.

The major cause for disruptions is the increase of impurities in the plasma, which radiate significantly through line radiation if not fully ionized. Impurities can enter the confined region due to various reasons: intentional injection of large amounts of impurities (for dedicated disruption experiments [66]), loss of plasma control or various instabilities which result in the plasma touching the tokamak wall [67].

A disruption typically happens on a millisecond timescale and consists of three phases: a thermal quench, a current quench and a runaway plateau. The evolution of the temperature and various currents is shown in Figure 2.4 for a typical disruption. The first phase, shaded red on the plot is the thermal quench where the plasma temperature drops from several keV to a few eV in a few milliseconds. During the thermal quench typically a spike can be observed in the plasma current before it starts decaying. This increase is caused by the flattening of the current density profile due to the breakup of the magnetic surfaces during the disruption [68]. After the thermal quench and the current spike the current starts decaying in the so-called current quench phase. In this phase the plasma is already at temperatures in the eV range hence its conductivity is low. The drop in current induces a changing magnetic flux, which induces an electric field generating runaway electrons, as indicated by the green runaway electron current on the graph. By the end of the current quench the plasma current is entirely driven by runaway

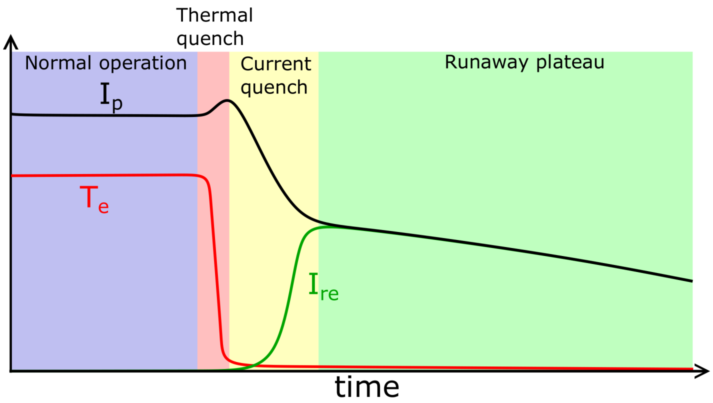

Figure 2.4: *The schematic evolution of a disruption in a tokamak. The three phases of the disruption and the initial normal operation regime are shaded in colors. The timescale of the disruption is in the order of milliseconds. The electron temperature T_e is shown in red, the plasma current I_p is in black and the runaway electron current I_{re} is in green.*

electrons, which decay on a timescale of a few $10 - 100$ ms. This decay is the so-called runaway plateau since it is much slower than the previous phases in the disruption, but it can have a fast final termination phase.

The dominant runaway electron generation methods during disruptions are hot-tail generation and avalanche generation. The nuclear sources can provide runaway electron seed for avalanche generation in case hot-tail and Dreicer generation are suppressed.

The confinement of the generated runaway electron beam depends on the magnetic field structure. In the thermal quench phase, when the magnetic field is stochastic and the field lines break, the losses can be significant. By the end of the thermal quench phase the magnetic surfaces can reform, increasing the confinement of the runaway electrons [69]. The controlled deconfinement of the runaway electron population is often key to avoid any damage to the device walls [66].

Disruptions can pose other risks to the device besides runaway electrons. The rapid cooling of the plasma is caused by intense radiation. The unmitigated deposition of the thermal energy of the plasma can lead to the melting of the plasma facing components in large tokamaks like ITER [70, 71] while stress in the structures of the vacuum vessel by electromagnetic forces also arise [72].

2.4 Runaway electron detection

Runaway electrons are generally detected in experiments by observing the emitted radiation [73, 74]. Runaway electrons can emit radiation through various processes: Bremsstrahlung and synchrotron radiation.

Bremsstrahlung radiation occurs when charged particles decelerate due to collisions with other plasma species or the first wall of the tokamak [75, 76]. It generally produces radiation in the hard X-ray range (HXR) and in the case of relativistic particles, it is highly anisotropic and is mainly directed along the velocity vector of the runaway electrons. The radiation can be used to gain information on the electron energy distribution function [75, 76].

Synchrotron radiation is produced by charged relativistic particles when moving in magnetic fields. A charged particle in a magnetic field moves in a gyromotion around the field line due to the Lorentz force if they have a velocity component perpendicular to the magnetic field. The acceleration from the circular motion generates radiation, which is called cyclotron radiation in general and synchrotron radiation for relativistic particles. It is highly anisotropic, as was Bremsstrahlung radiation in the relativistic case. Synchrotron radiation is also used to gain information on the electron distribution function since the anisotropy of the radiation can be used to get information on the pitch angle distribution of the electrons [77, 78, 79]. Pitch angle can be understood as the measure of how parallel the particle is travelling compared to the magnetic field, it is the angle between the velocity of the particle and the magnetic field line. The intensity of the synchrotron radiation strongly depends on the particle energy and its pitch angle.

The energy of a slightly relativsitic, supra-thermal electron distribution can be measured using the vertical electron cyclotron emission (ECE) diagnostic [80]. This measures the non-thermal electron cyclotron radiation through a vertical line of sight, and the electron energy can be calculated from the cyclotron frequency.

Alternative measurements of runaway electrons in tokamaks utilize the interaction of the plasma-facing components or probes with the runaway electron beam. When the highly energetic electrons are unconfined from the plasma volume, for example, due to the break-up of the magnetic surfaces, the collisions with the tokamak wall can produce high energy photons and neutrons through photonuclear reactions. These can be detected by neutron monitoring systems during disruptions when the neutrons produced by fusion reactions are not dominant [81].

Probes inserted into the plasma edge at various locations are also considered as a method to gain information on the runaway electron population. One design is the so-called Cherenkov-type probes, which enables the characterization of the energy distribution of the runaway electrons by employing multiple channels with minimum electron energy required for detection [82, 83].

2.5 Runaway electron mitigation

Runaway electrons pose the most threat when they are produced during the uncontrolled termination of tokamak plasmas. The minimization of the potential risk from disruptions is secured by several steps: disruption prediction, disruption avoidance and disruption mitigation [84].

Disruption prediction aims to forecast the occurrence of a disruption using adaptive learning techniques in real time [85, 86]. Once a disruption has been predicted, it can potentially be avoided by stabilizing the magnetic instabilities hence preventing the loss of thermal energy [87, 88]. If disruptions cannot be avoided, the mitigation of potential damage to the plasma-facing components is essential. The study of runaway electrons is relevant in the latter case, with two different approaches: runaway electron prevention and runaway electron mitigation. Since relying on complete avoidance of disruptions is unlikely, a mitigation method for disruptions is necessary.

The prevention of runaway electrons generally relies on the prevention of the formation of the runaway electron seed necessary for the avalanche method, since this is responsible for the creation of the majority of the runaway electron beam in large-current devices. The primary generation methods can be minimized by increasing the collisionality of the plasma by injection of material. For this purpose injection of noble gases, mainly argon and neon was considered in the form of Massive Gas Injection (MGI) [51, 89]. The idea of an MGI is to inject high Z impurities into the plasma in case of a disruption to increase the drag force on electrons and suppress runaway electron generation. It was shown however that gas injection of impurities was too slow and did not penetrate the plasma sufficiently in ITER [90]. Shattered pellet injection (SPI), where the injected material is frozen into solid pellets, and shatters before entering the plasma has been proved to successfully mitigate disruptions [91] and simulations have shown that SPI can successfully minimize runaway electron generation for ITER [92].

The presence of high Z impurities however causes a significant increase in the avalanche generation [93]. The physical reasoning is the following: the injected impurities are only partially ionized in the post-disruption plasma temperature, so only some of the electrons of the injected material will contribute to the increase in the friction force. In the avalanching process, on the other hand, the bound electrons are also participating. The increased friction cannot overcome the increase in target electrons for the avalanche generation and the resulting gain can be as large as tens of orders of magnitude [93].

The solution proposed was to inject SPI in two stages [92]. The first injection consists of deuterium with the purpose of diluting the plasma, so it can cool down without dissipating its thermal energy. This can effectively prevent hot-tail generation. The second injection is performed using noble gases, argon or neon to dissipate the thermal energy of the plasma isotropically to prevent damage to the first wall. The proposed two-stage pellet injector has been accepted for ITER for disruption mitigating purposes and has been tested in labortatory environment [94].

It is to be noted that in the presence of nuclear sources, see Sections 2.2.1 and 2.2.1, it is impossible to avoid runaway electron generation completely, as the avalanche process will always have the necessary seed through Compton scattering and tritium decay to generate significant runaway electron current. Hence the mitigation of the damage from runaway electrons is crucial.

One method proposed for this is the so-called resonant magnetic perturbation (RMP). During disruptions, another way of reducing the runaway electron risk is by enhancing the losses of particles. RMP achieves this by generating magnetic fields which disrupt the magnetic field structure of the tokamak and hence enhance the radial transport of particles. This method was studied experimentally on JT-60U [95] and TEXTOR [96] and allows for the depletion of the runaway electron population before the particles gain extreme energies from the electric field, but requires full stochastization of the plasma to avoid the formation of the runaway electron beam in the plasma centre.

Another approach considers the depletion of the formed runaway electron beam in a controlled manner. This is referred to as benign termination [66, 97]. This concept uses two phenomena to eliminate the runaway electron population: first, a low-Z material - usually deuterium - is injected into the plasma, which leads to an increase in the neutral pressure and recombines the low temperature plasma, called companion plasma, in which the runaway electron beam resides. Next, an MHD instability is triggered by lowering the edge safety factor. This instability expels the runaway electrons. The current carried by the runaway beam will be taken over by the Ohmic current in the cold companion plasma, resulting in high radiated power, and lower heat-loads on the plasma facing components [97].

The final defence planned on the DEMO reactor to mitigate runaway electron damage is the employment of so-called sacrificial limiters [98, 99]. These wall elements are planned to provide targets to the colliding runaway electron beam before the valuable first wall, hence preventing the energetic electron population from reaching the plasma-facing components.

Chapter 3

Modeling infrastructure

In this chapter, I will introduce the models I have used to simulate runaway electron generation. Two types of codes are used in runaway electron modeling: kinetic codes and so-called fluid codes. The kinetic codes solve the kinetic equation (2.4) with different collision operators for C_a to obtain the electron distribution function. They are typically computationally expensive, but more accurate than fluid models. Fluid models use basic plasma parameters such as density n, temperature T, current density j and electric field E to calculate runaway electron generation with steady-state generation formulas like (2.68) and (2.72). Fluid codes are computationally less expensive than kinetic codes, but generally less accurate.

3.1 Modeling tools

I have used several different models with various levels of complexity to study runaway electron generation. Runaway Fluid and Runaway Indicator [100] are the simplest codes and were developed at the Budapest University of Technology and Economics. They are part of a larger workflow called European Transport Simulator (ETS) which was developed in the European Integrated Modeling (EU-IM) framework [101]. They were used in integrated modeling efforts to study runaway electron dynamics. The NORSE [42], DREAM [102, 103] and SOFT [104, 105] are models developed at the Chalmers University of Technology. I used NORSE in the integrated modeling framework [100], used DREAM for self-consistent disruption simulations and SOFT for modeling the radiation from runaway electrons in disruptions. In the following, I will describe each code in more detail.

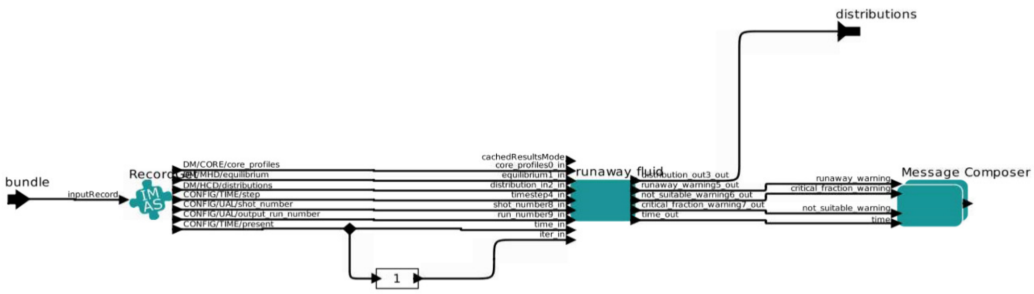

Figure 3.1: *The IMAS version of the Runaway Fluid code in Kepler.*

3.1.1 Integrated modeling

Integrated modeling is a concept of coupling different physical models into a complex simulation to achieve a more realistic description of physics. The coupling of codes is done in so-called graphical workflows, such as the European Transport Simulator (ETS). The communication between different codes is enabled by the introduction of a standardized data structure, which all codes use to get input from and write output to.

The standardized data structure in the European Integrated Modeling (EU-IM) framework is called Consistent Physical Objects (CPO) [106]. The different physical quantities in this data structure have specific locations in a tree structure. The communication of the codes and the CPO structure is also standardized, making the integration of codes into the framework simple. An upgraded version of the EU-IM framework based on the same concept is the ITER Integrated Modeling and Analysis Suite (IMAS) [107] which uses Interface Data Structures (IDS) instead of CPO-s.

The workflows where the physical models are coupled are created in a graphical workflow engine called Kepler [108]. The codes are imported into Kepler in the form of so-called actors. To generate actors from the codes written in different languages it is required to follow the input and output convention of the standardized data structures. The actors then can be pulled into the Kepler workspace, where the defined input and output ports can be connected between the different actors to build the workflows.

An example of an actor in Kepler can be seen in Figure 3.1. The blue boxes are the actors with the input ports appearing on the left of the boxes and the output ports on the right. The actor Message Composer is a so-called composite actor which contains a similar level as seen in the figure.

The main workflow developed in Kepler is the ETS, shown in Figure 3.2. ETS is a complex workflow design to simulate tokamak discharges. It has three separate parts: a start-up, a time loop and a post-processing. Start-up

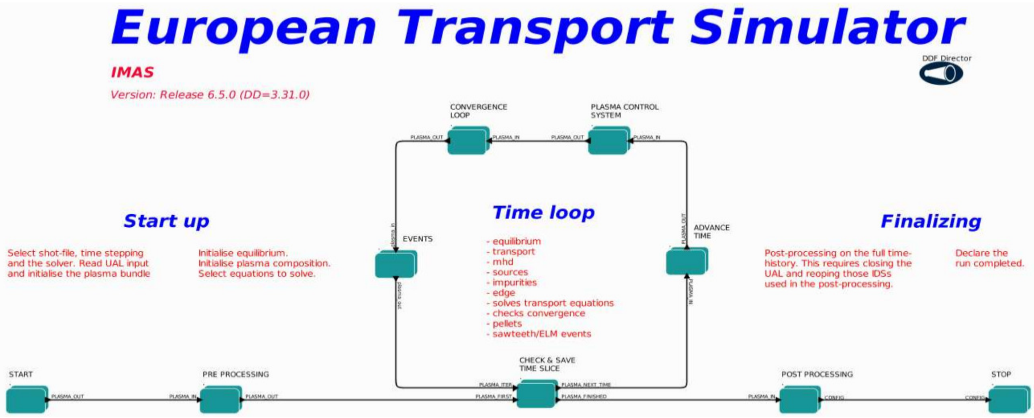

Figure 3.2: *The IMAS version of the European Transport Simulator (ETS) Kepler workflow.*

handles the reading and bundling of the input CPO/IDS used to start the simulation while the post-processing handles the writing of the calculated data into a different CPO/IDS. The time loop contains the Convergence Loop composite actor which contains different physics models which use the bundled data from the input to simulate different physical processes such as current drive, particle transport processes, heating, impurity evolution and runaway electrons. The loop works as follows: the first composite actor advances the time so the time loop calculates the plasma state in the $t + dt$ time compared to the input data. If any plasma controls are enabled in the simulation setup they are handled in the next actor. The convergence loop composite actor contains the physics codes which calculate the plasma quantities for the new time step. The solution is iterated until a convergence is reached. Then different events can be simulated and finally the output is saved and the next time step starts.

ETS contains multiple codes for simulating some physical processes which are interchangeable with each other. This flexibility can be used to simulate situations requiring different approximations. The codes communicate in ETS via the bundle, a temporary instance of a CPO/IDS database, each code writes its output into this and the next code uses the new data.

Runaway Fluid and Runaway Indicator are included in the ETS workflow. The former is located in the Convergence Loop, in the Heating and Current Drive sub-actor, while the latter is in the Events actor. Both codes are written in C++ but they have different functionality. ETS was not developed for exclusively simulating runaway electron dynamics, so the Runaway Indicator was designed to indicate if the electric field in the plasma is larger than the critical electric field (2.49). It also calculates the Dreicer growth rate (2.68) to indicate if it is too large for accurate modeling with fluid codes. It is located in ETS after the Convergence loop so it calculates the critical field based on the plasma parameters in the new time step.

If the Runaway Indicator indicates that runaway electron generation is possible Runaway Fluid can be used to calculate the runaway electron population. Runaway Fluid includes Dreicer and avalanche generation rates introduced in Section 2.2. It includes two additional generation rates for Dreicer generation, one in low temperature cases [40]

$$\gamma_{D,nr} = \frac{Cn_e}{\hat{\tau}_{ee}} \left(\frac{E}{E_D} \right)^{-3/16(1+Z_{eff})} \exp\left[-\frac{E_D}{4E} - \sqrt{(1+Z_{eff})\frac{E_D}{E}} \right], \tag{3.1}$$

and one for cases with high normalized electric field E/E_c

$$\gamma_{D,hf} = \gamma_{D,nr} \exp\left[-\frac{T_e}{mc^2} \left(\frac{1}{8} \left(\frac{E_D}{E} \right)^2 + \frac{2}{3} \left(\frac{E_D}{E} \right)^2 / 3\sqrt{1+Z_{eff}} \right) \right]. \tag{3.2}$$

The avalanche generation can be modified to include a low threshold electric field E_0, below which avalanche generation is not possible. This is shown to arise when a momentum conserving approach is used to calculate the avalanche generation [109] and can be estimated as

$$E_0 \approx 1 + \frac{\frac{Z_{eff}+1}{\sqrt{\bar{\tau_{rad}}}}}{\sqrt[6]{\frac{1}{8} + \frac{(Z_{eff}+1)^2}{\bar{\tau_{rad}}}}} \tag{3.3}$$

where $\bar{\tau_{rad}}$ is the normalized time of synchrotron losses given as

$$\bar{\tau_{rad}} \equiv \frac{\tau_{rad}}{\hat{\tau}_{ee}} = \frac{1}{\hat{\tau}_{ee}} \frac{6\pi\varepsilon_0 m_0^3 c^3}{e^4 B^2}. \tag{3.4}$$

It was shown that both the avalanche and Dreicer generation rates can be modified by the effects of toroidicity in a tokamak [110], reducing the generation rate. The toroidicity correction from [110] is also implemented in Runaway Fluid as

$$\frac{\gamma_D}{\gamma_{D,cyl}} = 1 - 1.2\sqrt{\frac{2\epsilon}{1+\epsilon}} \tag{3.5}$$

for the Dreicer generation and

$$\frac{\gamma_A}{\gamma_{A,cyl}} = \frac{(1-\epsilon)^2}{\pi\sqrt{\epsilon E/E_c}} \tag{3.6}$$

for the avalanche generation. $\epsilon = a/R$ is the inverse aspect ratio in both these correction formulae, where a is the minor and R is the major radius of the tokamak and the γ_{cyl} generation rates are the reduced generation rates due to toroidal effects.

The output of Runaway Fluid includes the generation rates, the runaway electron density and the runaway electron current density calculated with the assumption that all runaway electrons travel with the speed of light. These quantities are all calculated for each radial location.

While both Runaway Indicator and Runaway Fluid were implemented in the CPO version of ETS, I have developed the IMAS integration for these codes. This included the mapping of the input and output variables onto the updated data structure, generating and adding the actors into ETS and testing the implementation.

I integrated the kinetic code NORSE (NOn-linear Relativistic Solver for Electrons) [42] in the EU-IM framework. NORSE was developed in MATLAB to simulate scenarios with large electric fields, comparable to the Dreicer field. In such cases, the whole electron distribution function distorts from a Maxwellian in an event called slide-away. The simulation of such events is enabled in NORSE by the implementation of a non-linear collision operator, compared to the linearized Fokker-Planck operator, (2.54), generally used in other kinetic codes. NORSE also includes the slowing down effects from synchrotron radiation. The distribution function is calculated on one spatial dimension (r) and two momentum space coordinates ($p_\parallel$ and $p_\perp$).

Integrated modeling enables the coupling of different codes by simplifying communication between models using a standardized data structure and access to the said data structure. One of the main advantages of this approach is the easy interchangeability of the different physics models integrated into the framework. The price of this modularity is the complexity of larger workflows and the lack of inherent physical consistency.

3.1.2 Disruption modeling tool

ETS was not developed to simulate disruptions but rather tokamak flattop operation. A dedicated disruption simulation code was developed at the Chalmers University of Technology called Disruption and Runaway Electron Analysis Model (DREAM) [102]. DREAM is capable of simulation tokamak disruptions while evolving the plasma self-consistently, without the evolution of the magnetic geometry, and calculating the runaway electron population either in fluid mode, kinetically, or in mixed mode.

Most of the background plasma parameters are solved using a 1-D transport equation

$$\frac{\partial X}{\partial t} = \frac{1}{V'}\frac{\partial}{\partial r}\left[V'\left(-\langle A^r\rangle X + \langle D^{rr}\rangle \frac{\partial X}{\partial r}\right)\right] + \langle S\rangle \tag{3.7}$$

where V' is the spatial Jacobian and $\langle X\rangle$ indicates spatial flux surface averages. The plasma temperature is evolved including effects of temperature advection and diffusion, collisional heat transfer and radiation losses. The evolution of the ion species is modeled by rate equations for each charge state while the electron density is calculated by maintaining the quasineutrality of the plasma. The current density and electric field are evolved by the mean-field equation of the poloidal flux. Generally the code calculates the plasma profiles in 1 dimension, along the mid-plane outer radius, but it is also possible to calculate the plasma evolution on realistic two-dimensional magnetic geometry. The full equations governing background plasma evolution can be found in [102].

DREAM solves the bounce-averaged kinetic equation of the form similar to Equation (2.27) for the electron population

$$\frac{\partial f}{\partial t} = \frac{1}{\mathcal{V}'}\frac{\partial}{\partial z^m}\left[\mathcal{V}'\left(-\{A^m\} f + \{D^{mn}\} \frac{\partial f}{\partial z^n}\right)\right] + \{S\} \tag{3.8}$$

where z^i are the phase-space coordinates, A describes advection effects and D describes diffusive terms [102]. The advection term contains the acceleration from the electric field, collisional friction, synchrotron radiation reaction force and radial transport. The diffusion term describes both momentum space diffusion and radial diffusion. S is a source term, describing the knock-on collision operator for avalanche generation and a particle source. The curly brackets indicate bounce-averaging over three angle coordinates, the toroidal angle ϕ, the gyrophase ζ and the poloidal angle θ

$$\{X\} = \frac{1}{\mathcal{V}'}\int_0^{2\pi} d\zeta \int_0^{2\pi} d\phi \oint d\theta \sqrt{g} X, \tag{3.9}$$

$$\mathcal{V}' = \int_0^{2\pi} d\zeta \int_0^{2\pi} d\phi \oint d\theta \sqrt{g}, \tag{3.10}$$

where $\sqrt{g}$ is the metric of the phase-space coordinate system [102].

The novelty of DREAM is how it handles the electron population. It separates the thermal electron population, called cold electrons in DREAM,

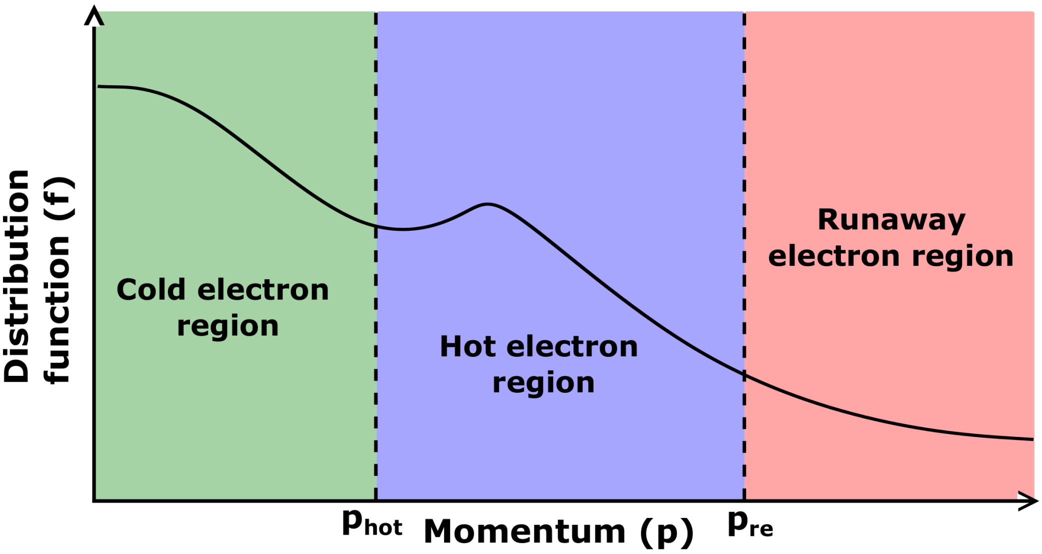

Figure 3.3: *The division of the momentum space by DREAM. The figure is based on Figure 1 from [102].*

and the suprathermal fast electrons, the latter being further split into hot electrons and runaway electrons, to separate momentum space regions, each with unique resolution, as shown in Figure 3.3. DREAM can be run in different modes: the fully kinetic mode, where all of the momentum space is resolved kinetically by solving the kinetic equation (3.8, or in superthermal mode where only the non-Maxwellian part of the distribution function is calculated kinetically and the thermal population is evolved using fluid models to save on the computational costs. It is also possible to solve for the hot and/or runaway electron population using fluid mode, in this case, DREAM solves a fully fluid system. The cold electrons are calculated in suprathermal and fully fluid mode as

$$\langle n_{cold} \rangle = \langle n_{free} \rangle - \langle n_{hot} \rangle - \langle n_{re} \rangle, \tag{3.11}$$

where $\langle n_{free} \rangle$ is the total number of free electrons in the plasma, $\langle n_{hot} \rangle$ are the hot electrons and $\langle n_{re} \rangle$ are the runaway electrons. DREAM can calculate all five of the different runaway electron generation methods. For fluid Dreicer generation it uses the neural network for high Z impurities [46] and the formula for avalanche generation includes the effects of high Z impurities as well [93].

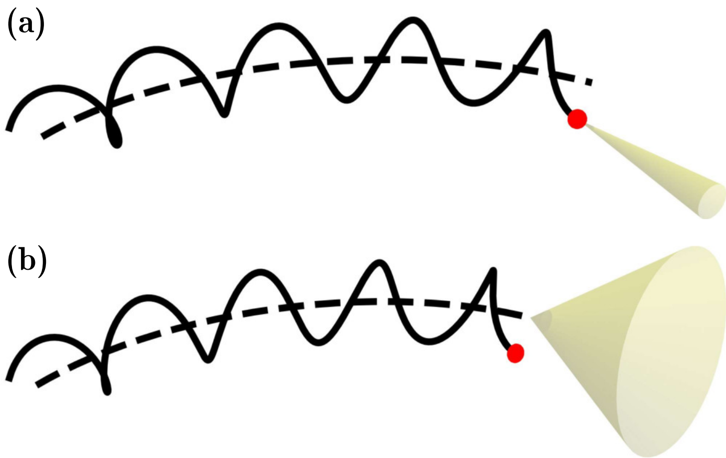

Figure 3.4: *The visualization of the cone approximation. Synchrotron radiation is highly directional along the particle velocity vector, as shown in panel (a). The cone approximation accumulates the total radiation from the gyromotion of particles around the magnetic field line as the surface of a thin cone originating from the guiding center with opening angle equivalent to the particle pitch angle, as shown in panel (b). The image is taken from [111].*

3.1.3 Radiation modeling tool

The radiation from runaway electrons can be simulated with the SOFT (Synchrotron-detecting Orbit Following Toolkit) synthetic diagnostic framework [104]. SOFT is capable of calculating the synchrotron radiation from an electron distribution function as seen by a specified detector.

The synchrotron radiation in SOFT is calculated using the so-called cone approximation, shown in Figure 3.4. Charged particles in magnetic fields are travelling in helical trajectories wound around the magnetic field lines due to the Lorentz force. The synchrotron radiation is highly directional along the velocity vector of the motion. In the cone approximation, the radiation is calculated on the surface of a cone with an opening angle equal to the particle pitch angle, centered on the guiding center of the helical motion.

SOFT calculates the tokamak geometry as a circular torus defined by given minor and major radii, and the magnetic field geometry can be given either as an analytical formula or can be imported from numerical solvers. The detector location, viewing direction, entrance pupil, field of view angle and spectral range also have to be specified.

Chapter 4

Modeling results

The utilization of the models introduced in Chapter 3 is described below. Sections 4.1, 4.2, 4.3 describe my modeling in integrated modeling frameworks using two dedicated workflows: a dedicated runaway electron workflow and the European Transport Simulator (ETS). Section 4.4 gives the results I obtained in modeling the radiation of runaway electrons generated in potential disruptions on JT-60SA tokamak.

4.1 The Dreicer generation in rapidly changing plasmas

The reduced computational costs of fluid models are paid back in a tradeoff for accuracy, especially in transient scenarios. Integrated modeling tools generally use the simpler fluid models to calculate runaway electron dynamics, such as Runaway Fluid and Runaway Indicator, and the analytic formulas given in Section 2.2 are used in another integrated modeling code called ASTRA-STRAHL [112]. Kinetic runaway electron modeling developed significantly in the recent year, with codes like DREAM [102], and NORSE [42], but the complexity of kinetic models so far prevented their integration into integrated modeling.

The reduced kinetic models use the analytic expressions (2.68, 2.72) for runaway electron generation. These expressions were derived for stationary plasma parameters and can be inaccurate for rapid plasma evolution. The kinetic model NORSE was integrated into the EU-IM framework to assess the time scales of plasma evolution requiring more accurate kinetic models.

The actors in Kepler workflows can be written in a selected set of languages supported by the EU-IM infrastructure: C/C++, Fortran, Java, Matlab, Python [113]. NORSE is written in Matlab language, but the integration

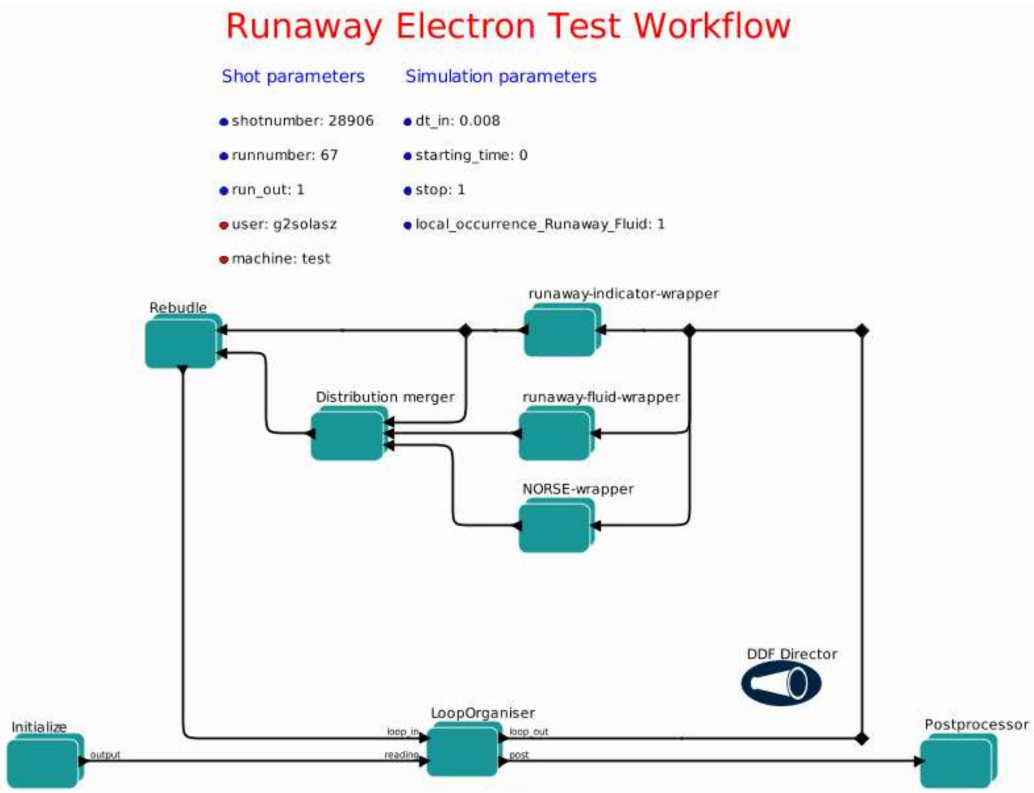

Figure 4.1: *The Runaway Electron Test Workflow.*

was developed using a Matlab-Python interface [114]. The NORSE actor is developed in Python, which calls a Python interface executing Matlab commands. The Python actor handles the communication between NORSE and the CPO data structure both for the reading of input data and writing the output.

NORSE was added to a dedicated runaway electron workflow designed to enable easy comparison of different runaway electron models. The workflow is shown in Figure 4.1. It contains the NORSE actor, the Runaway Fluid actor and the Runaway Indicator actor parallel in a time loop. The boxes are so-called composite actors, each containing a separate workflow themselves, with the input and output provided to the composite actor. The contents of `runaway-fluid-wrapper` composite actor are shown in Figure 4.2. The input bundle is given from the left of the figure, where the data is processed. The input required by the Runaway Fluid actor is extracted from the CPO tree structure and is given to the actor in specified input ports. The output data is given to the distribution output port which passes it on to the level

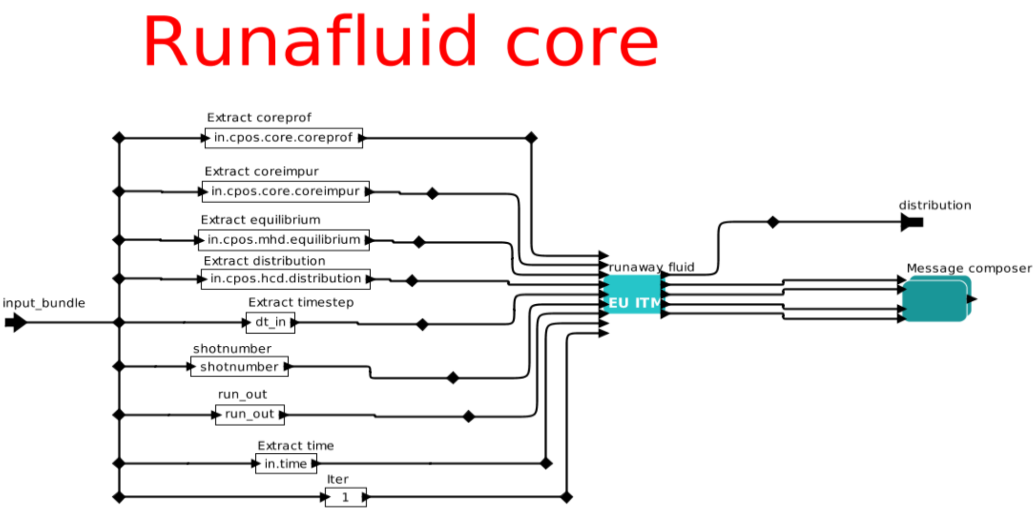

Figure 4.2: *The contents of the `runaway-fluid-wrapper` composite actor.*

above. Runaway Fluid can output messages during the workflow execution which is handled in the `Message composer` composite actor.

The Runaway Electron Test workflow starts in the `Initialize` composite actor. This reads in the input data specified by the shot parameters: `shotnumber` and `runnumber` specifies the CPO instance to be read in, while `run_out` specifies the instance for the output CPO. The CPO structure allows for the importation of experimental data from machines. The `machine` parameter can specify which machine name, given the data is imported to the database of the user. The simulation parameters are used to specify numerical options during the workflow execution: `dt_in` specifies the size of the time step, `starting_time` gives the first time point of the simulation, `stop` tells the workflow the number of iterations in the time loop. NORSE and Runaway Fluid produce data which are stored in the same location in the CPO structure. The parameter `local_occurence_Runaway_Fluid` is used to distinguish the output produced by NORSE and Runaway Fluid.

The next composite actor is the `LoopOrganiser` which starts the time loop where the physical codes are located and keeps iterating until the specific number of iterations is reached. The workflow ends in the `Postprocessor` composite actor, which outputs the calculated data into the specified CPO. The loop contains the physics models and two support actors, the`Distribution merger` and the `Rebundle` actors. The first merges the two output instances from Runaway Fluid and NORSE without overwrite, while the `Rebundle` composite actors merge the output from the three models into the bundle, so it can be used in the next time step. The main advan-

	Low density discharge (LD)	**Start–up phase (SU)**	**End of disruption (ED)**	**Start of disruption (SD)**
Density [m^{-3}]	$5 \cdot 10^{17}$	$5 \cdot 10^{17}$	10^{20}	10^{20}
Temperature [eV]	10000	300	300	10000
Electric field [V/m]	$2.81 \cdot 10^{-3}$	$2.96 \cdot 10^{-2}$	3.66	$4.38 \cdot 10^{-1}$
Critical field [V/m]	$5.06 \cdot 10^{-4}$	$4.16 \cdot 10^{-4}$	$6.98 \cdot 10^{-2}$	$8.77 \cdot 10^{-2}$
Normalized electric field [-]	5.55	71	52.5	5
Coulomb logarithm [-]	19.9	16.3	13.7	17.2
Collision time at critical velocity [s]	$2.58 \cdot 10^{-1}$	$6.84 \cdot 10^{-3}$	$6.42 \cdot 10^{-5}$	$1.74 \cdot 10^{-3}$

Table 4.1: *The plasma parameters for the various scenarios.*

tage of this approach is the ability to run different codes with identical input parameters with ease and having the output in the same format making it easy to compare.

The workflow was used to study the dynamics of Dreicer generation of runaway electrons during rapidly changing plasmas, such as during disruptions. The results from the workflow were complemented by calculations with two additional kinetic models: the kinetic solver DREAM, which solves the kinetic equation with a linearized collision operator and LUKE, a bounce-averaged kinetic solver [115, 116].

Four different scenarios were chosen with a combination of low and high temperature and density, to represent various cases when runaway electron generation is possible. The various physical parameters for each of the cases are given in Table 4.1. The first case aimed to represent a low density discharge (LD) often performed in tokamaks to study runaway electron generation [57, 58], with density $5 \cdot 10^{17}$ m^{-3} and temperature 10 keV. The second scenario has the same low-density value as the low-density discharge but with a small temperature of 300 eV, aimed to replicate the circumstances during a tokamak start-up (SU). The final two cases represent disruptions, the first of the two replicates the start of a disruption (SD) with the high-temperature value from the LD case and a high density of 10^{20} m^{-3}, while the last case represents the circumstances at the end of a disruption with high density and low temperature. These basic plasma parameters were kept constant throughout the simulations as the effects of rapid change in the electric field were studied.

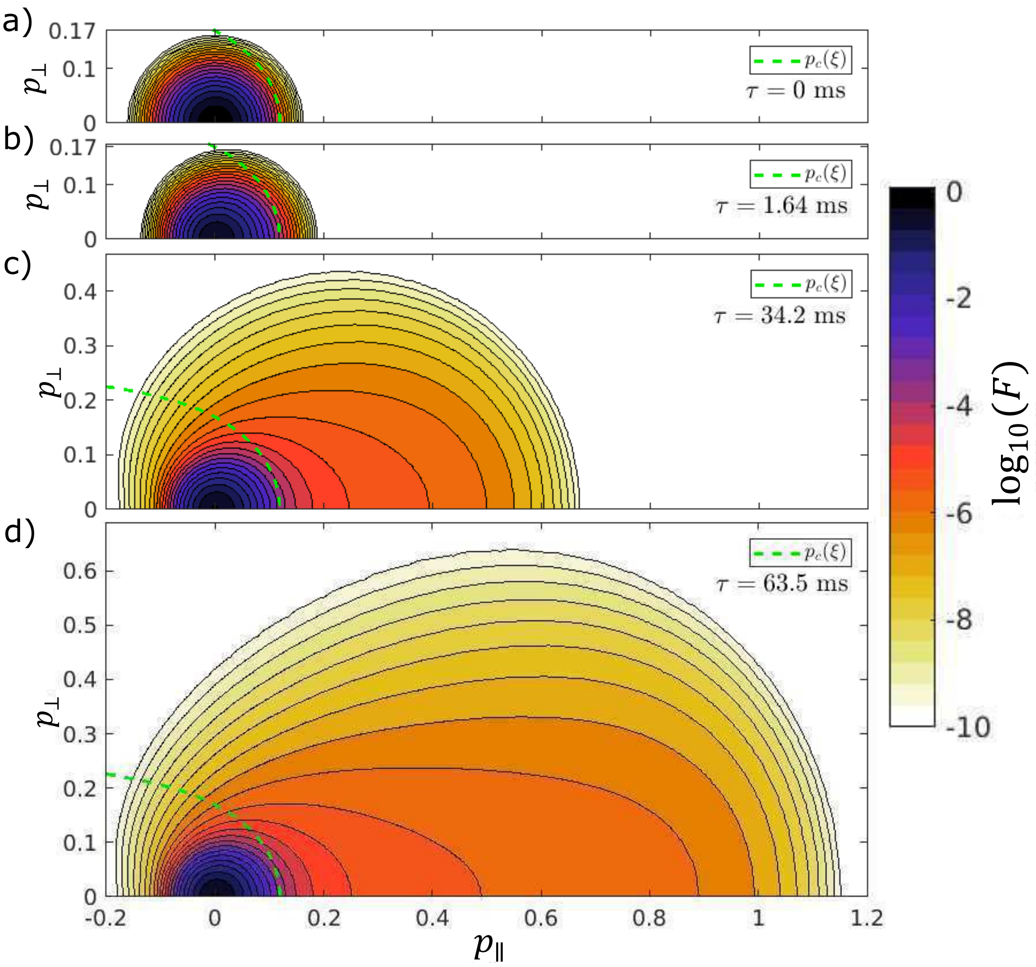

Figure 4.3: *The evolution of the NORSE distribution function for the start–up scenario. The green dashed line indicates the runaway electron boundary.*

The jump in the electric field was modeled by a step function and the response of the system was studied. The electric field was chosen to be moderate for each scenario to avoid slide-away of the whole electron distribution function, where most of the models are invalid. Out of the four codes, only NORSE and DREAM are capable of calculating the synchrotron radiation losses, so the magnetic field strength was chosen to be zero to avoid slowing down from radiation.

The evolution of the distribution function as calculated by the NORSE code is shown in Figure 4.3. The distribution function is plotted in 2-D momentum coordinates $(p_\parallel, p_\perp)$ and the green dashed line is the runaway

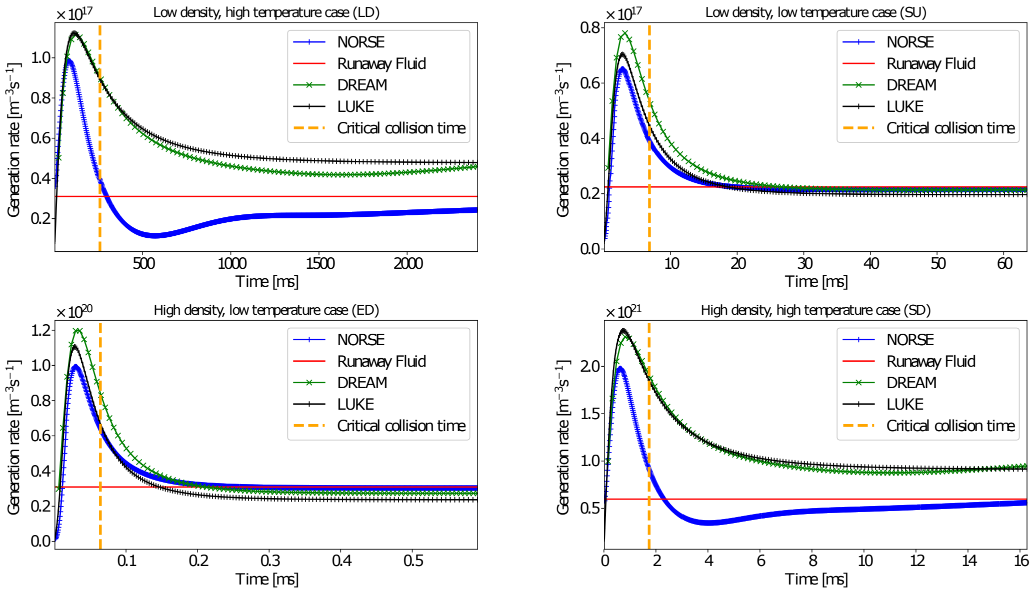

Figure 4.4: *The temporal evolution of the runaway electron growth rate in the four different scenarios. The kinetic codes all produced a large peak in runaway generation when the electric field was applied.*

electron boundary [49]. The jump in the electric field is applied at $\tau = 0$. The initial Maxwellian electron distribution function very quickly shifts due to the applied electric field without significant distortion of the shape. The formation of the high-energy tail happens on a longer timescale, as seen on panels c) and d).

The runaway electron growth rate can be calculated for each code and it is shown in Figure 4.4. The quasi-stationary growth rate from Runaway Fluid is indicated with red and is constant as expected. The kinetic models all follow the same overall evolution with several notable differences. The common features are the sudden peak in generation rate at the beginning of the evolution for each code and the eventual relaxation towards the stationer Dreicer rate. The peak can be explained by the initial shift of the Maxwell distribution into a Spitzer-like distribution, where a significant portion of the original distribution function is shifted into the runaway region [114].

Several differences can be spotted in the plots in Figure 4.4. The maximum of the peak is different in many cases between the kinetic models. This can be explained by the different definitions of runaway electrons in each model. Another significant discrepancy can be observed between the kinetic growth rates during the LD and SD cases compared to the other two. In

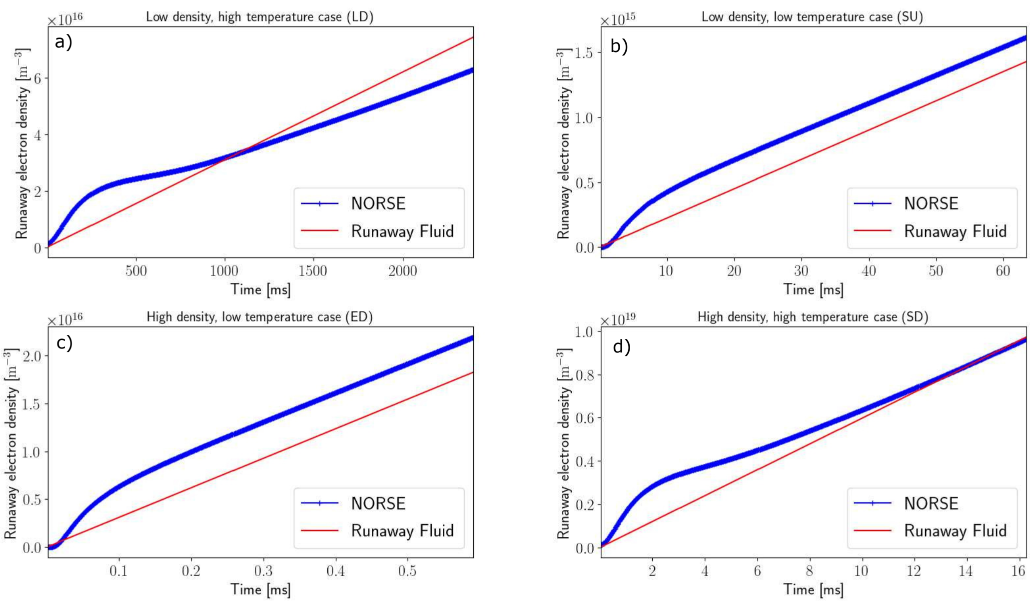

Figure 4.5: *The runaway electron density as a function of time for the four cases as calculated by NORSE and Runaway Fluid.*

the low-density and high-density cases (plots a) and d)) the kinetic growth rates differ from the analytic value, the linearized codes are larger while the non-linear NORSE undershoots the fluid value. It was found that in these two cases significant runaway electron population was generated, roughly about 10% of the electrons turned to runaway electrons. In such cases the interaction between the runaway electron and the bulk populations becomes non-negligible. This invalidates the linearized operators, which do not include the effects of bulk-runaway interactions as well as the quasi-stationer formula can overestimate the generation. NORSE however can be considered accurate even with large runaway electron populations and this explains why the other kinetic codes and the analytic model produce larger rates.

In the other two cases (plots b) and c)) the runaway electron population is smaller and the bulk interactions are less important. Here all the kinetic codes approach the analytic value smoothly. Overall the qualitative agreement can be seen between kinetic codes with the major features appearing in all scenarios with all kinetic codes.

Another noticeable difference between the four scenarios is the timescale of the runaway generation, spanning four orders of magnitude. The timescale of the peak can be related to the electron-electron collision time at the critical velocity

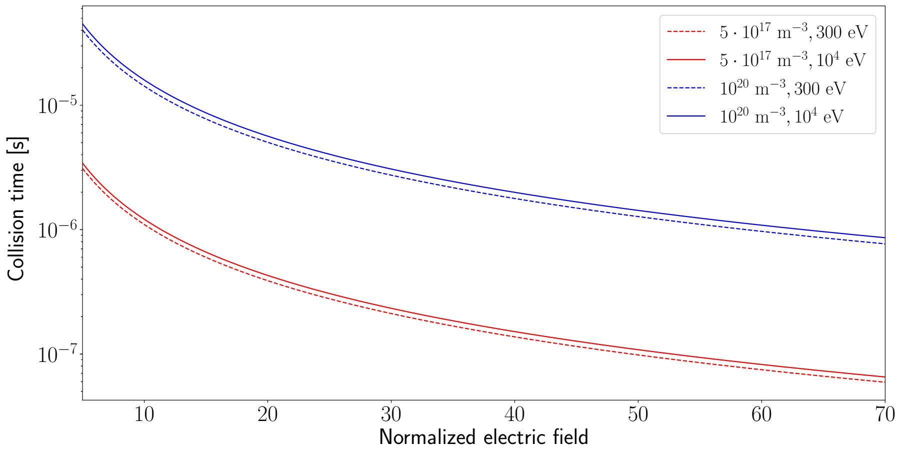

Figure 4.6: *The dependence of the electron-electron collision time on the electric field normalized to the critical field. The colour indicates the low or high-density cases, while the solid and dashed lines distinguish the temperature value.*

$$\hat{\tau}_{ee} = \frac{4\pi\varepsilon_0^2 m_e^2 v_c^3}{n_e e^4 \ln\Lambda}, \tag{4.1}$$

where the critical velocity v_c can be calculated as

$$v_c = \frac{c}{\sqrt{E/E_c}}, \tag{4.2}$$

with E_c being the critical electric field (2.49). This collision time is indicated on each panel with a vertical yellow dashed line.

The runaway electron density from NORSE and Runaway Fluid is shown in Figure 4.5. The initial peak in the generation rate causes an initial discrepancy between the results of the two models. This eventually disappears in the two cases where the runaway electron population is significant compared to the initial electron density, as we have seen NORSE giving lower generation rates in these cases. The difference in the other two cases is constant as the growth rates equalize over time.

The dependence of the collision time at critical velocity on the plasma parameters can be seen in Figure 4.6 and 4.7. Figure 4.6 shows the value of the collision time for the four cases as a function of the normalized electric field. The different colours distinguish the high and low-density cases, while the solid and dashed lines are used for the different temperature values. The

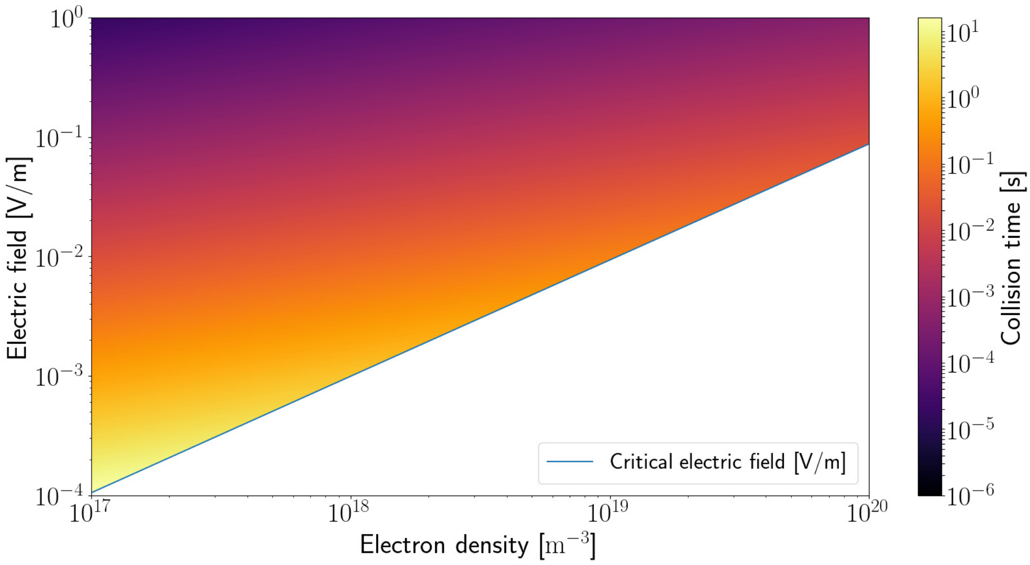

Figure 4.7: *The dependence of the electron-electron collision time on the electric field and the density for a constant temperature of* 10 keV. *The blue line indicates the value of the critical electric field, below which the critical velocity is not defined.*

temperature dependence is negligible, but a strong dependence can be seen on the electric field and the density.

The dependence of the collision time at the critical velocity on the density and electric field is plotted in Figure 4.7. The temperature is kept constant at 10 keV, while the critical electric field is indicated with a blue line. The collision time spans seven orders of magnitude in the studied range of density and electric field. Note that the collision time can reach the order of magnitude of seconds in the low-density range.

The electron-electron collision time at the critical velocity is a robust indicator of the necessity of kinetic modeling. If the timescale of the evolution of plasma parameters is comparable to this critical collision time, then the reduced kinetic models using analytic growth rate formulas cannot be used. This indicator can be used in integrated modeling to estimate when the computationally less expensive models are viable [114].

The input CPO fields of NORSE	
Electron temperature	coreprof/te/value
Electron density	coreprof/ne/value
Parallel electric field	coreprof/profiles1d/eprallel/value
Effective charge	coreprof/profiles1d/zeff/value
Radius	coreprof/rho_tor
Magnetic field	coreprof/toroid_field/b0

Table 4.2: *The input CPO fields required by NORSE.*

4.2 Kinetic modeling in integrated modeling frameworks

Kinetic modeling of runaway electrons in integrated modeling frameworks has not been utilized previously. Most integrated modeling used fluid models with quasi-stationary analytic models to simulate runaway electron generation [117, 112]. The reduced-kinetic models can often be less accurate compared to the full kinetic treatment, but the computational complexity and cost of kinetic models prevented their efficient utilization in integrated modeling tools.

Kinetic models have developed considerably in recent years capable of simulating runaway electron dynamics with better efficiency by restricting kinetic treatment to the relevant momentum space regions, as in DREAM [102] or enabling the simulation of scenarios outside the range of validity of fluid codes, such as NORSE [42]. This promotes the necessity of the integration of kinetic models into the integrated modeling frameworks.

The NORSE non-linear kinetic solver was integrated into the EU-IM framework. The interfacing was done in Python language, utilizing a Matlab engine to call NORSE with the input read in and the output written through the Python interface. The model requires input data from the core profiles CPO describing the basic plasma parameters such as electron temperature and density and the electric field parallel to the magnetic field lines. The full list of CPO fields used by NORSE is given in Table 4.2.

The output from the NORSE code is also saved into the CPO structure including the electron distribution function and the associated momentum space grid. The proper storage of the 2-D distribution function produced by NORSE had to be developed as kinetic runaway electron modeling was not previously used in the CPO structure. The main difference of the NORSE distribution from other codes solving for distribution functions in the EU-IM framework [118], such as the StixReDist Fokker-Planck solver [119] is the

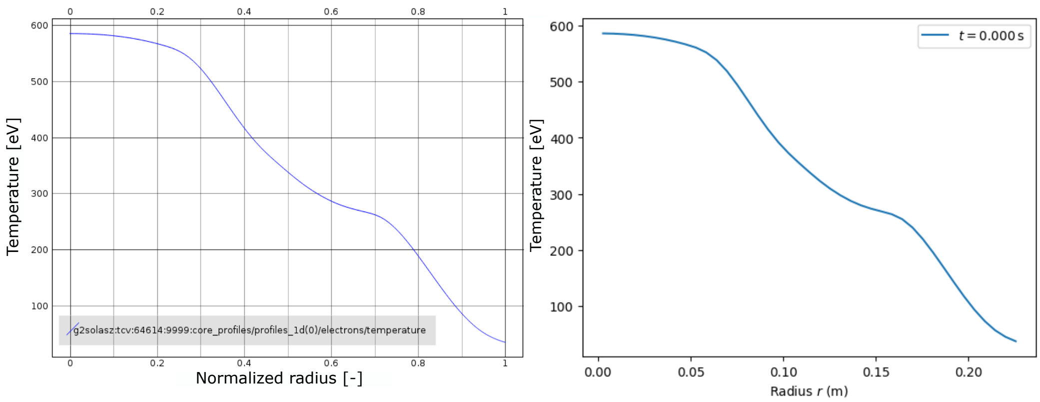

Figure 4.8: *The initial temperature profile used to validate the DREAM-IMAS interface. The left plot is the data as plotted directly from the imported experimental data in IDS, the right shows the DREAM temperature profile at the start of the simulation.*

coordinate system used by NORSE. NORSE solves for the electron distribution in 1-D space and 2-D momentum space coordinates and this coordinate system is stored in a dedicated grid structure in the *Distribution* CPO. The associated momentum coordinates, p, the normalized momentum, and ξ, the pitch angle, and the radial coordinates are stored along the distribution function. Besides the distribution function and the associated coordinate system, the runaway electron density, and runaway electron current are saved in the CPO output.

The interfacing of NORSE was on in a dedicated runaway electron workflow, see Figure 4.1, and it was utilized in the study of Dreicer generation rate in rapidly changing plasmas, see Section 4.1.

To further expand the modeling capabilities of the integrated modeling tools and to make the validation against experimental results easier the interfacing of DREAM into the IMAS framework was developed. The integrated modeling framework was updated from the EU-IM framework to the IMAS framework when the integration of DREAM was proposed, hence the CPO interfacing was not done.

DREAM is developed in C++ with a Python wrapper around the computing core [102]. This enables faster computations compared to a pure Python code as C++ is a compiled language. The use of the model is made easier by the Python wrapper by eliminating the need for recompilation for every simulation. The communication between the C++ core and the Python wrapper is done via HDF5 files. An interface was developed in Python, which enables the communication between DREAM and the IDS structure.

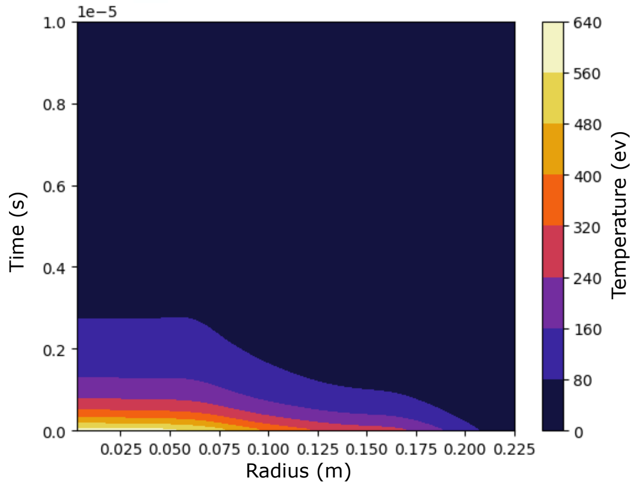

Figure 4.9: *The temperature evolution of the disruption started from the experimental data imported from TCV.*

One of the main advantages of code integration into the IMAS framework is the ability to simulate directly from experimental data. The IMAS framework enables the importation of experimental data directly from devices into the IDS structure which can be used as input by different codes. Machines capable of exporting experimental data to IMAS are [120], TCV [121], ASDEX Upgrade (AUG) [121], MAST [121], JET [35], EAST [122, 123] and of course will be ITER [124], for which the IMAS framework is being developed [107].

The use of the DREAM-IMAS interface was demonstrated by simulating a disruption based on the input from TCV shot 64614. The initial parameters of DREAM were taken from the experimental data and a disruption was simulated by a prescribed exponential temperature drop. The read-in of the data was validated, and the initial temperature profile from the IDS and DREAM is shown in Figure 4.8.

The simulation was set up with an exponential temperature decay to provide sufficient cooling of the plasma to generate runaway electrons. The temperature evolution can be seen in Figure 4.9. Sufficient cooling can be seen along the whole plasma radius, with a final temperature of a few eV.

The disruption produced sufficient runaway electron current, as seen in Figure 4.10. The graphs show the 2-D runaway electron current density as a function of radius on the x-axis and as a function of time on the y-axis.

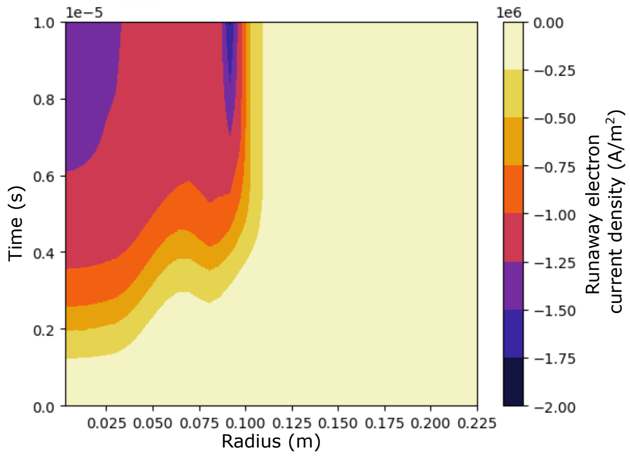

Figure 4.10: *The current density evolution of the disruption started from the experimental data imported from TCV. The negative current density indicates the direction of the current, as required by the convention in the IDS structure.*

The runaway electron beam is dominantly located on the magnetic axis, at small radii, where the initial temperature was higher. This is expected as the primary generations are sensitive to temperature and low temperatures at the plasma edge are not sufficient to produce runaway electrons. The negative values for current density represent the direction of the current.

This simulation used fluid generation of runaway electrons, with the neural network for Dreicer generation, the analytic formula for avalanche generation. This was chosen to be computationally less expensive as the aim of this simulation was to demonstrate the capability of simulating with experimental data and the use of kinetic runaway generation should not affect this.

The interfacing also allows for prescribed simulation based on the input data. This means that the plasma parameters do not evolve self-consistently but follow the time evolution prescribed in the input data. This provides a more robust option for code validation against experimental results. The data imported for testing the interface did not describe a runaway electron experiment, but a standard flat-top experiment. The ability of the code to run with prescribed data was demonstrated, but no runaway electron physics was produced.

The interfacing of codes into the IMAS framework enables a robust solution to validate theoretical models against experiments by the importation of experimental results into the IDS data structure. The models can then be run directly with the experimental input.

4.3 Self-consistent disruption simulations with the ETS

The European Transport Simulator (ETS) was developed in the European Integrated Modeling (EU-IM) framework to simulate core transport processes of tokamak plasmas [125, 126]. It is a 1.5-D transport solver, as it solves a 1-D transport equation at the plasma core with 2-D treatment of the equilibrium and the plasma edge. It is a fully modular tool, with multiple codes integrated for various physical aspects. These models are easily interchangeable for each simulation making ETS a robust tool to simulate various plasma scenarios.

Two different versions of ETS were used in self-consistent disruption simulations: the EU-IM version is referred to as ETS5 while the version developed in the IMAS framework is ETS6. The same principles are used for both versions of the Kepler workflow, the only difference is the data structure used. ETS5 uses the CPO structure, while ETS6 is using IDS-s. Both versions have Runaway Fluid and Runaway Indicator for runaway electron modeling purposes.

The simulation was based on an ASDEX upgrade experiment, shot 33108, where a disruption was induced by massive material injection (MMI) of argon gas. The experimental data is shown in Figure 4.11. A peaked temperature profile was achieved by intense electron cyclotron resonance heating (ECRH) to ensure sufficient runaway electron generation during the disruption. The thermal quench occurs due to the argon injection at 1 s. The radiation peak due to the impurities can be seen on the bottom panel in red. The timescale of the thermal quench and the current quench is on the ms scale and cannot be resolved on the graphs. The runaway electron beam decays on longer timescales however, hence the runaway plateau is visible on the plasma current graph in black on the top panel.

The experimental data was imported into the CPO structure and the resulting data was used in ETS to simulate a self-consistent disruption simulation. The simulation was done in two separate phases. First, an interpretative simulation was done by ETS on the pre-disruption plasma. This phase started from $t = 0.8$ s and lasted until the start of the disruption at $t = 1$ s. The imported experimental data could have missing fields in the CPO structure required by ETS for a predictive simulation, so the interpretative run was performed to fill all necessary fields and simply ensure the

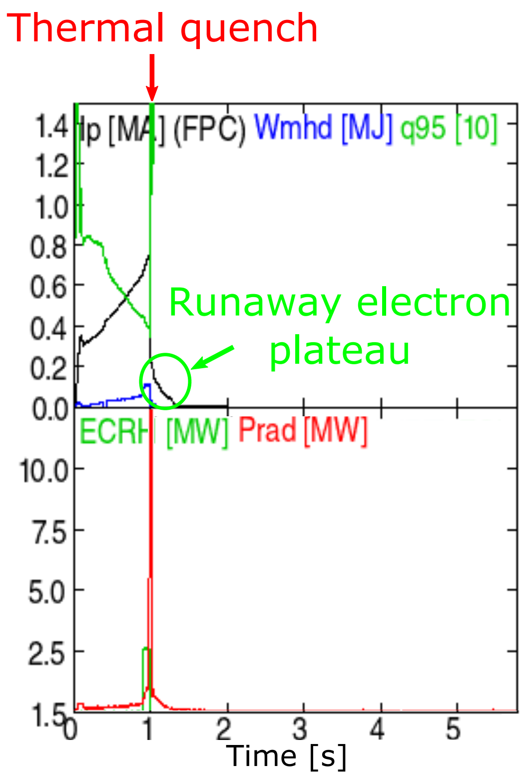

Figure 4.11: *The experimental data of the AUG shot 33108. The thermal quench can be seen at $t = 1s$, indicated most dominantly by the radiation peak on the bottom panel with red. The plasma current is shown in black on the top panel. The argon injection happens during the so-called ramp up phase, when the plasma current is increasing. After the thermal quench, the runaway plateau can be seen.*

consistency of the input data. Such fields include the parallel electric field, which is required to calculate runaway electron generation.

A predictive simulation was performed after the necessary initialization, starting from the injection of the argon gas. The argon injection is simulated by the introduction of an argon density of $3 \cdot 10^{19}$ m^{-3} at the plasma edge in coronal equilibrium. Additional 10^{13} m^{-3} argon in neutral state was added and the total amount was chosen to be equal to the argon used in the experiment. The inward movement is ensured by artificially increasing the advection and diffusion coefficients. This imitates the increased transport due to the breakup of the magnetic surfaces due to the MMI [68] as well as the inward propagation from the injection.

The plasma density evolution is simulated self-consistently for the main ion density and the impurity density for each charge state, while the electron density is solved for by enforcing the quasineutrality of the plasma. The initial profiles were taken from the input data. The plasma composition was taken from the experimental data. The main ion species was deuterium, with no impurities present initially.

The electron and ion temperature evolution are both solved self-consistently governed by radiation losses and energy exchange terms as well as heat transport. The impurity temperature is assumed to be equal to the main ion temperature at all times for simplicity. No heating was applied during the disruption phase. A minimum temperature of 10 eV was set for the ion and 4 eV for the electron temperatures. The plasma current is governed by the current diffusion equation [126] with boundary condition of loop voltage $V_{loop} = 0$ at the plasma edge to simulate a perfectly conducting tokamak wall.

The evolution of the plasma parameters is shown in Figure 4.12. The columns of the graph show different times during the simulations. The first column shows the initial profiles, the second column shows the plasma state halfway through the simulation, and the last column is the final result. The rows show different plasma parameters. The first row shows the evolution of the plasma temperature for both electrons in red and the main ion species in blue. The second row shows the electron and main ion densities in the same colour coding, while the last row shows the q-profile in red and the current density profile in blue. Each plot has the radius on the x-axis.

The temperature evolution is shown on the top row. The argon is injected from the right-hand side. This produces an inward-moving cooling front towards the plasma centre, which clearly shows the progression of the argon impurities. The electron temperature starts cooling first through radiation and heat transport. The cooling of the main ion species is dominated by energy exchange with the cold electron population, hence it lags behind the electron temperature. The final temperature profile is a constant at the minimum allowed temperature except at the boundary where the boundary condition was set to a higher value due to stability reasons.

The initial electron and ion densities, shown on the second row of Figure 4.12 are identical as described by the quasineutrality requirement. The injected argon gas is partially ionized as it reaches higher temperatures resulting in increased electron density compared to the main ion densities. This is best seen on the second panel in the second row where a peaked electron density profile can be seen at the mid radius of the plasma. Some argon has already reached the centre of the plasma, resulting in increased electron density at the magnetic axis. The transport of electrons also contributes to this. The final electron density is peaked in the center but it is reducing due to reconnection and the neutralization of the argon and deuterium at the low

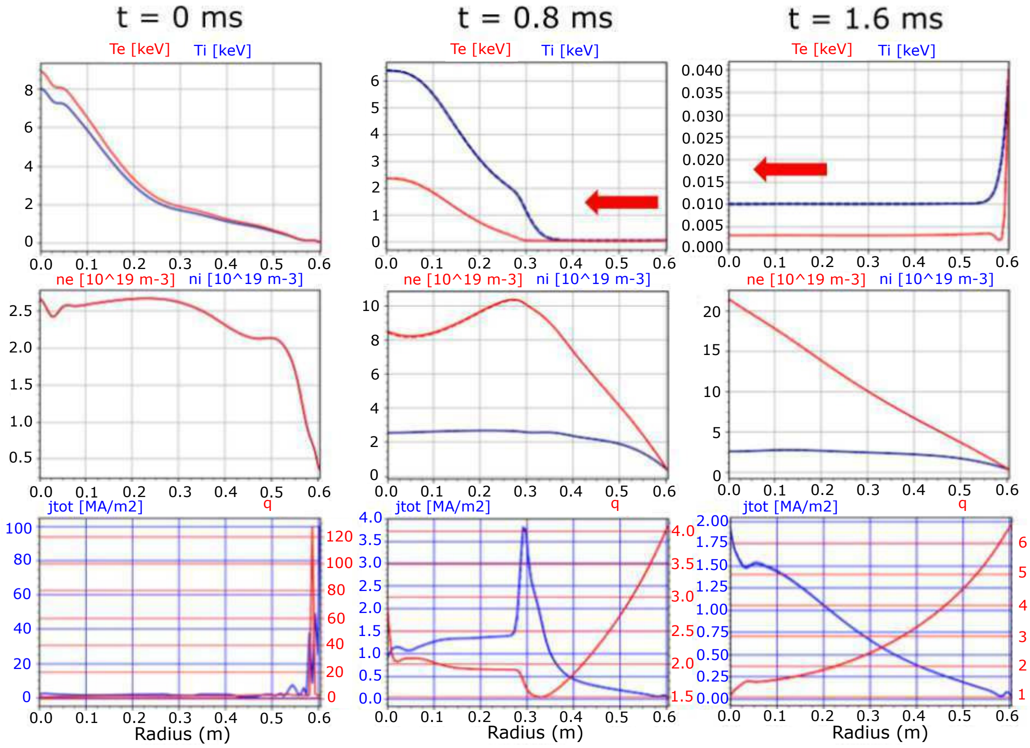

Figure 4.12: *The plasma evolution during the simulated disruption of the AUG shot 33108 by ETS5. The columns show different time points while the rows show different plasma parameters. The first column is the initial state at the start of the argon injection. The second row is the plasma state at halfway through the simulation while the last is the final state. The first row shows the temperature evolution of electrons (red) and ions (blue). The second row shows the electron density (red) and ion density (blue) while the last row shows the q-profile (red) and the total plasma current density (blue).*

temperatures present at the end of the disruption.

The final row shows the evolution of the plasma current and the safety factor. The cooling plasma has increased resistivity, see (1.8), causing a decrease in the plasma current density. The current diffusion pushes the current density toward the higher temperature plasma in front of the cooling front resulting in a current peak best seen on the middle panel in the bottom row. When the plasma is fully cooled the current density is pushed all the way to the magnetic axis, where the current starts to decay. It induces an electric field generating runaway electrons. The peak on the last panel in the last row at the centre is the runaway electron current.

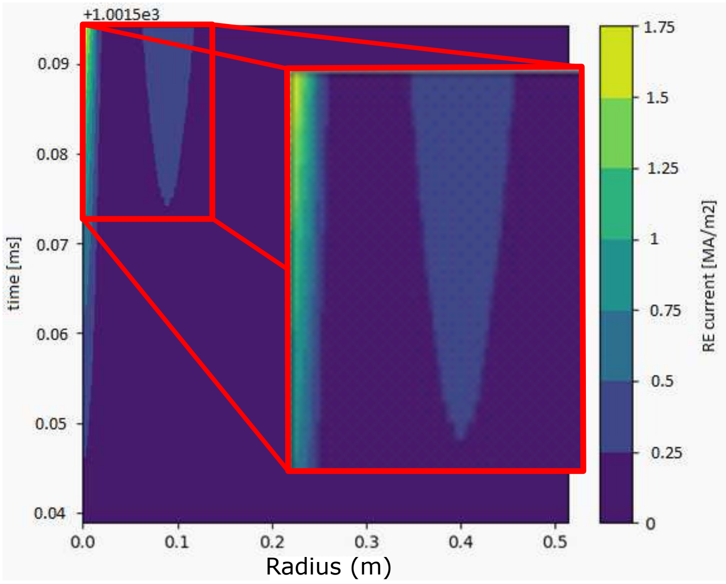

Figure 4.13: *The runaway electron current density as a function of radius and time. The runaway beam forms in the centre of the plasma and a smaller population can be seen at* 0.1 *m.*

The runaway electron current density is shown in Figure 4.13. A significant runaway electron current can be seen on the magnetic axis and a smaller runaway electron population at 0.1 m. These correspond to the peak seen on the last graph of Figure 4.12.

The same simulation was performed with the new, IMAS version of the ETS, referred to as ETS6 [127]. It works with the IDS data structures but the concept is the same as ETS5. The same AUG shot 33108 was imported into the IDS data structure and the interpretative run from $t = 0.8$ s to $t = 1$ s was done to ensure self-consistent input parameters.

The same setup parameters and considerations were used for the ETS6 simulation as it was described above. The temperature evolution of the electrons and ions is shown in Figure 4.14. The same dynamics can be observed for the temperature evolution with ETS5. The argon is injected from the right side of the graphs and the inward propagation pushes a cooling front in front of the injected argon. The final plasma state has a highly peaked ion temperature at the magnetic axis, while the electron temperature is almost constant, reaching a few eV values.

The plasma densities are shown in Figure 4.15 for the same time points. The introduced argon gas at the plasma edge starts to ionize producing increased electron densities. We can see significant argon has already reached

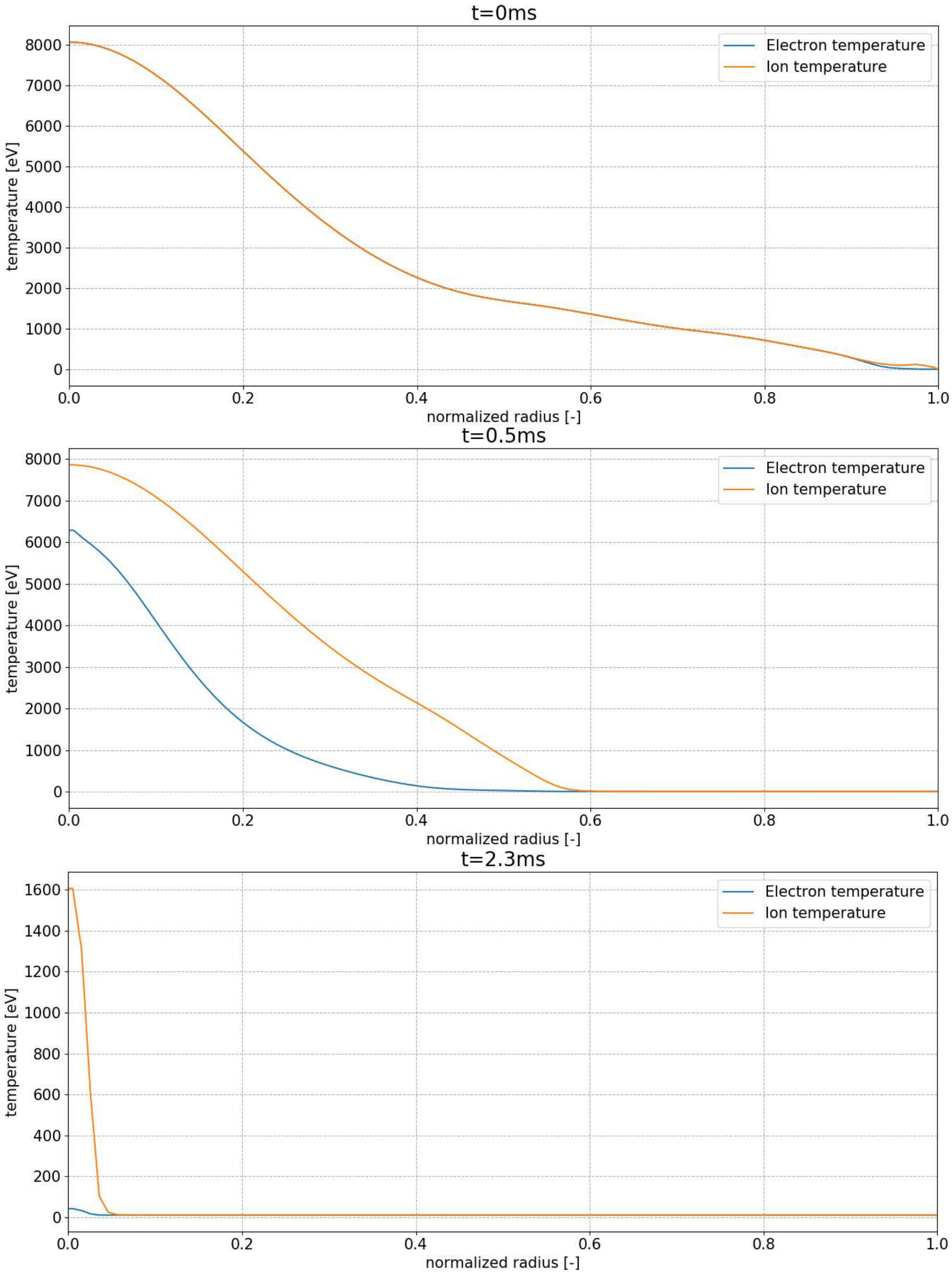

Figure 4.14: *The temperature evolution of the electrons and ions in the disruption as simulated by ETS6.*

the center of the plasma by 0.5 ms resulting in a flat electron density profile. The final electron density is similar to the ETS5 result, see Figure 4.12.

The evolution of the plasma current is shown in Figure 4.16. The total plasma current is shown in blue. It current starts to decay directly from the start of the simulation and the formation of the runaway electron current can be seen at the end of the simulation by the orange curve, showing the non-inductive current part of the total current. This is made out entirely of runaway electrons.

The plasma current calculated by ETS was benchmarked against the current evolution of the experimental results and the simulation results as calculated by the ASTRA-STRAHL modeling tool [112]. The result is shown in Figure 4.17. The ETS6 current is significantly lower than the other two results, which was discovered to be due to an input problem. The current decay is much sharper in the beginning compared to the other two curves, but the time scale current drop is comparable to the experimental and the ASTRA-STRAHL results. This is best seen in Figure 4.18, where the current evolution of ETS was vertically fitted to match the magnitude of the other two results, and remarkable agreement was found.

Further simulation of the current evolution by ETS6 was not possible due to instabilities within the workflow arising from the sharp gradient of the ion temperature at the end of the simulation, see Figure 4.14.

4.4 Simulation of runaway electron radiation in JT-60SA

Runaway electrons are routinely detected in present devices by visible and infrared cameras [128, 129] observing the synchrotron radiation from the relativistic particles. The detected radiation carries information on the electron distribution in real and momentum space which can be reconstructed [77, 78, 79].

The JT-60SA tokamak has recently been completed in Japan [130] with the first plasma demonstrated recently. It is the largest operating superconducting tokamak to date and is planned to provide an important contribution to the ITER and DEMO experiments, including runaway electron studies [131]. JT-60SA does not have a dedicated camera system for runaway electron detection. The Event Detection Intelligent Camera (EDICAM) [132] is installed on the tokamak [133] and it is operating in the visible spectrum, where runaway electron radiation can be expected. EDICAM was not considered for runaway electron detection purposes before and it was proposed

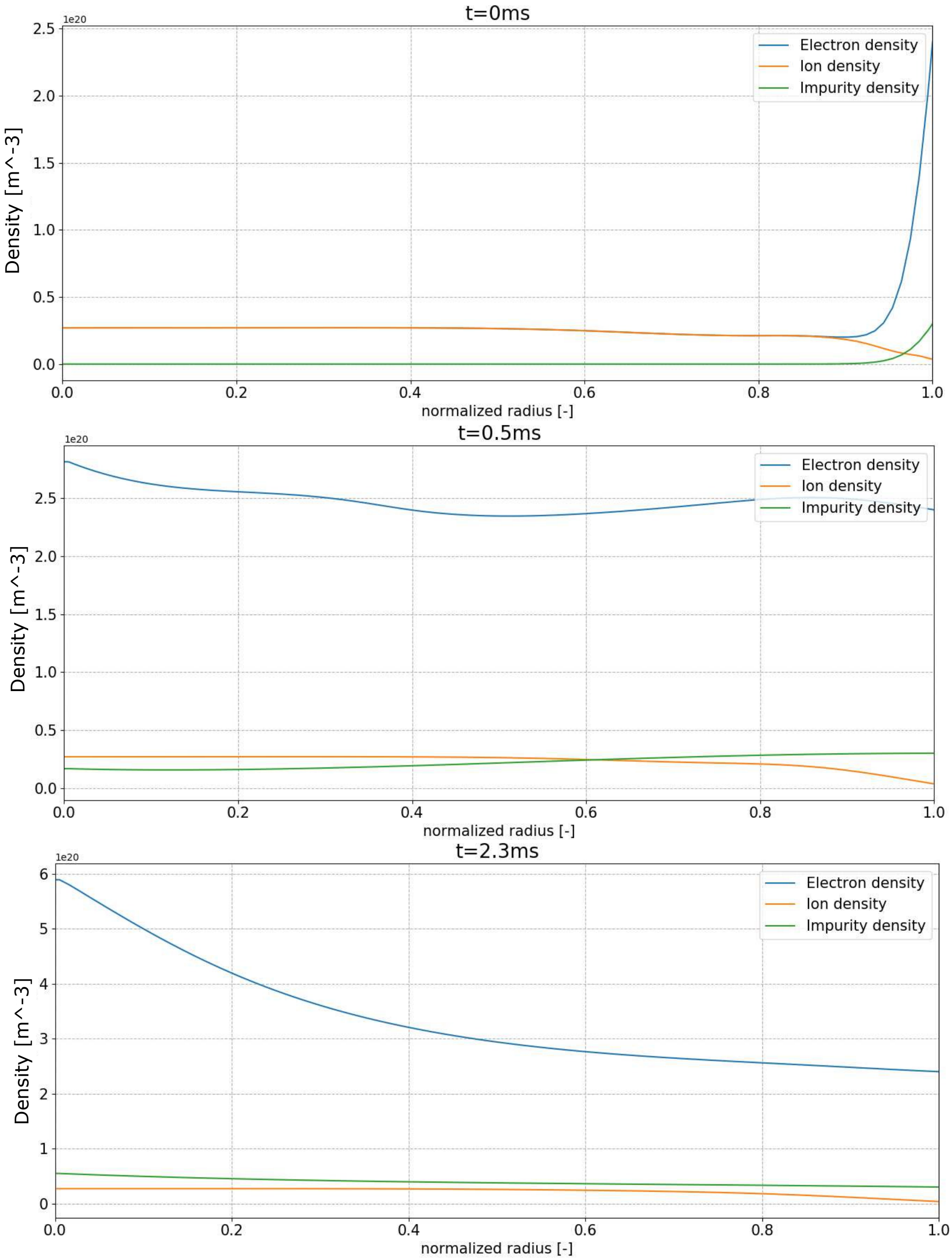

Figure 4.15: *The density evolution of the electrons, ions and impurities in the disruption as simulated by ETS6.*

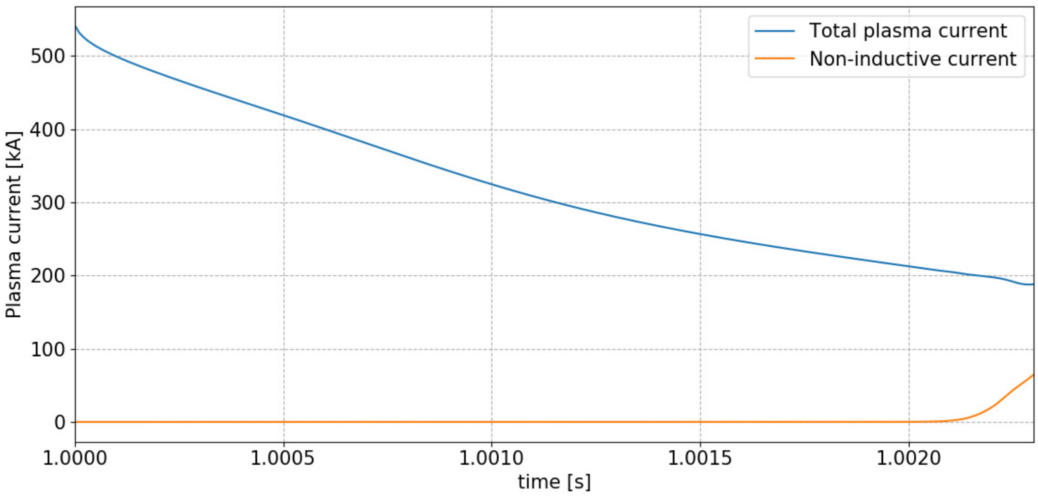

Figure 4.16: *The evolution of the total plasma current (blue) and the non-inductive part of the current (orange). The latter entirely consists of runaway electrons.*

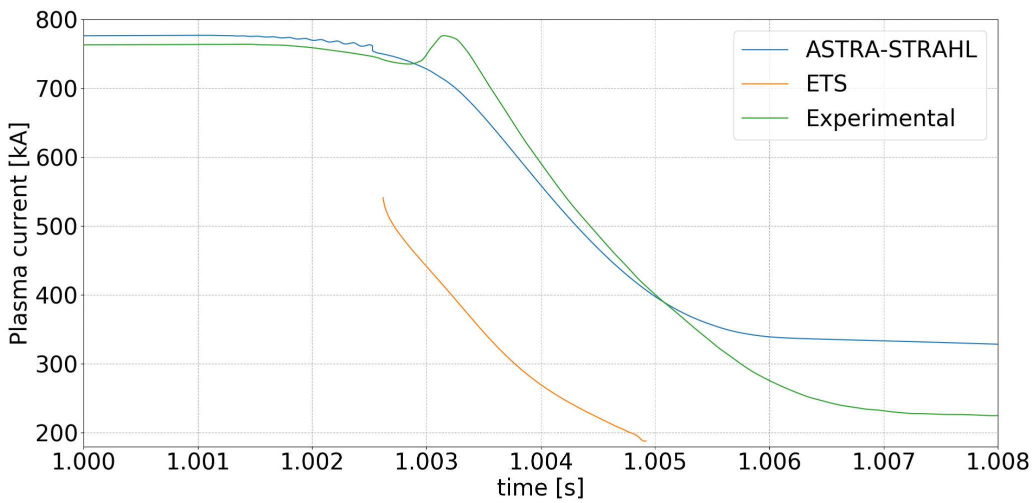

Figure 4.17: *The evolution of the plasma current as a function of time. The orange curve shows the plasma current calculated by ETS, the blue curve shows the results of the ASTRA-STRAHL model [112] and the green curve shows the experimental results.*

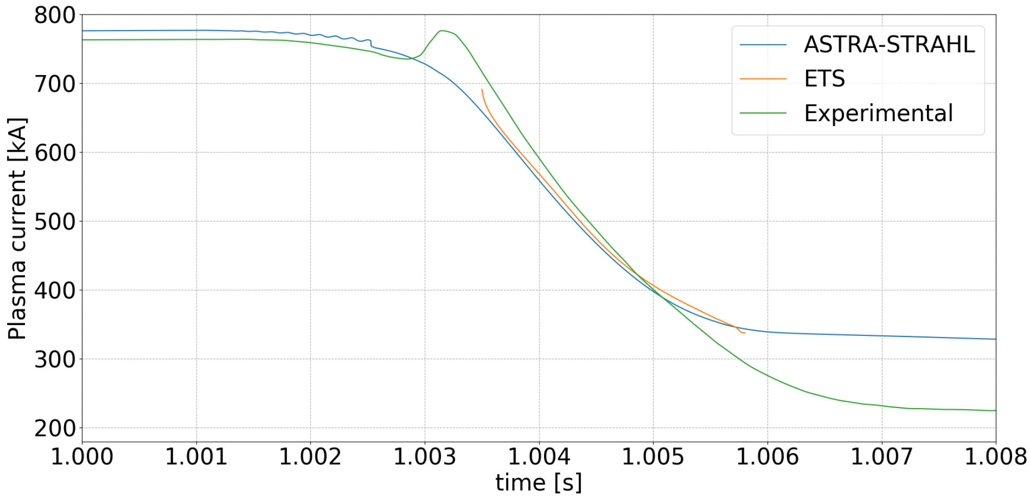

Figure 4.18: *The fitted plasma current shows similar temporal evolution for the simulation with ETS as the results from ASTRA-STRAHL [112] and the experiment.*

Parameter	Value
Position (x,y,z) (m)	$(-4.5304, -1.7552, 0.2312)$
Viewing direction (vector) (m)	$(0.60915, 1.01379, 0)$
Field of view (FOV) (degrees)	80
Spectral range (nm)	520–720
Entrance pupil (diameter) (mm)	5

Table 4.3: *Optical parameters of the EDICAM system as installed on JT-60SA.*

to expand the scope of the diagnostics on JT-60SA [134].

The feasibility of the EDICAM system was assessed for runaway electron detection by a disruption simulation for a JT-60SA-like tokamak using the DREAM code. The resulting runaway electron distribution function was given to the SOFT synthetic diagnostic framework, which calculated the radiation images from the electron population as seen by the EDICAM system on JT-60SA.

The EDICAM characteristics relevant to the SOFT simulation are given in Table 4.3. The coordinate system for the position and viewing direction of the camera is shown in Figure 4.19. The field of view, i.e. the opening angle of the cone seen by the camera is 80° and the spectral range is in the visible spectrum between $520 - 720$ nm. The size of the entrance pupil is 5 mm in diameter.

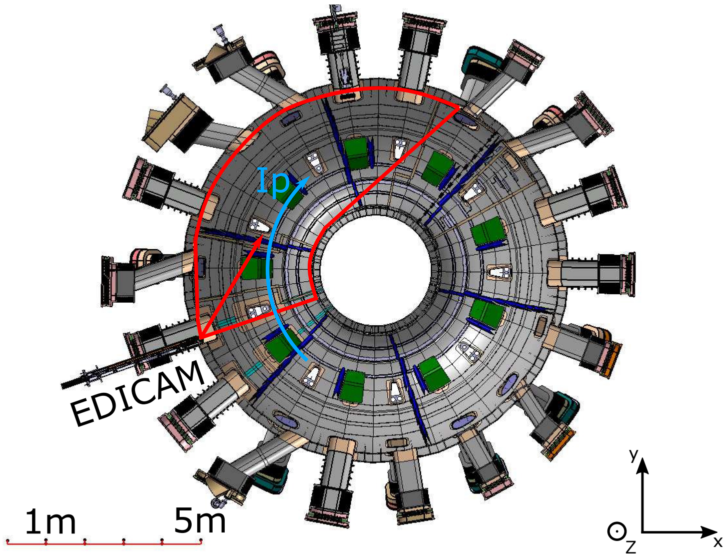

Figure 4.19: *The schematic top-view of the JT-60SA tokamak with the EDICAM location and viewing field indicated. The Direction of the plasma current is shown in blue. The coordinate system directions for the position and viewing direction of the EDICAM system in Table 4.3 is shown in the bottom right.*

The location of the EDICAM system is shown on the schematic top-view of JT-60SA in Figure 4.19. The viewing direction and viewing area are shown in red, and the coordinate system directions for the camera location and viewing vector are indicated in the bottom right. Since synchrotron radiation is highly directional along the velocity vector of the runaway electrons, the first requirement of seeing the radiation with EDICAM is that the electrons move towards the camera. This can be checked by looking at the direction of the plasma current, shown in blue. The electrons travel opposite to the plasma current, so EDICAM is potentially capable of detecting radiation along the electron velocity vectors. The simulated camera view of the EDICAM system on JT-60A is shown in Figure 4.20.

The spectral sensitivity of the EDICAM can be shown in Figure 4.21. Figure 4.21a shows the transmission efficiency of the optical elements in EDICAM between 400 and 1000 nm. The efficiency is high along the plotted range, with a drop below 500 nm. Figure 4.21b shows the camera sensor response as a function of wavelength on the same range. The straight lines indicate various levels of quantum efficiency. Quantum efficiency gives the fraction of photon energy detected, including the non-sensitive parts of the sensor. EDICAM is most sensitive between 500 and 700 nm, with an efficiency of 15%, but it can potentially detect photons up to 1000 nm. EDICAM

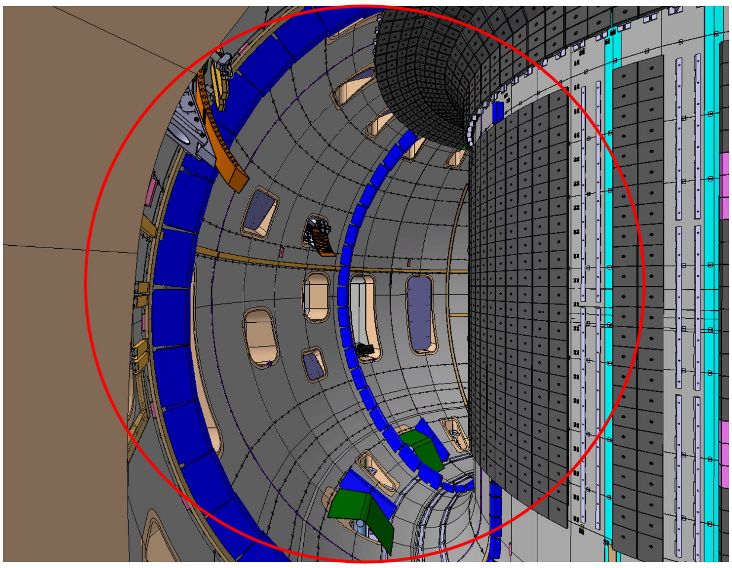

Figure 4.20: *The simulated camera view of the EDICAM on JT-60SA. The red circle indicates the field of view.*

has a nominal range of 520 − 720 nm however, so this was used during the simulations.

A disruption was simulated with DREAM for a JT-60SA-like geometry to produce an energetic runaway electron population with radiation visible by the EDICAM system. The initial profiles were taken from an EFIT [135] magnetic equilibrium calculation done for JT-60SA. The current was chosen based on a high current scenario proposed in the JT-60SA research plan [131], with a total plasma current of 5.5 MA. This scenario was chosen so sufficient runaway electron generation can be achieved. The initial profiles are shown in Figure 4.22. This scenario gave values for the on-axis magnetic field strength, 2.25 T, the major radius, 2.96 m and the minor radius, 1.18 m. The wall distance from the last closed flux surface was chosen to be 25 cm and the wall time was set to 150 s. The wall distance was estimated from JET values [136] and the wall time was taken from simulation for the JT-60SA structure [137]. These quantities are required for the boundary condition of the electric field calculations in DREAM.

The disruption was induced by argon massive gas injection (MGI), as this system is available as a disruption mitigation system [138]. The simulation was done in five different phases. The electric field was not given as an initial condition, so the first phase calculated it based on the provided profiles, such as temperature, density and current density. Then the argon was uniformly

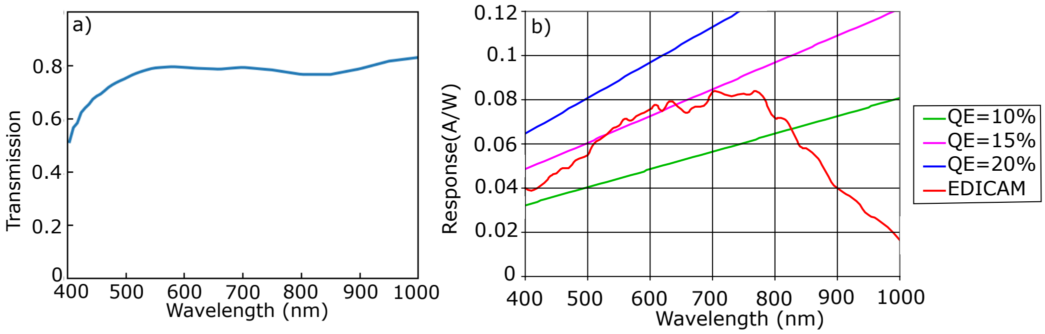

Figure 4.21: *The spectral sensitivity of the EDICAM. The transmission efficiency of the camera components components is shown on the left (graph a)). The transmission is close to constant along the studied range only dropping off below* 500 *nm. The sensitivity of the camera sensor is shown in graph b). The straight lines correspond to* 10%*,* 15% *and* 20% *quantum efficiency, the fraction of the photon energy absorbed by the sensors including the effect of non-sensitive areas of the pixels. EDICAM has a peak efficiency of* 15% *between* 500 *and* 700 *nm.*

introduced on every radial point with a density of 10^{20} m^{-3}. The argon density was chosen to be comparable to the main ion density, deuterium, to produce sufficient cooling. The introduced argon was allowed to ionize in 1 μs. The next phase ensured the cooling of the plasma by enforcing an exponential temperature decay until the plasma temperature reached 100 eV at the centre. The fourth phase had a self-consistent temperature evolution dominated by radiative losses from the injected impurity, and the simulation was finished with the calculation of the runaway electron plateau. The total simulation time was 8.6 ms.

DREAM was used in a fully kinetic mode, meaning the bulk, hot and runaway electrons were resolved kinetically. The radial resolution was limited to 20 radial points to reduce computational costs. The final runaway electron distribution function was given to the SOFT synthetic diagnostic framework, along with the EDICAM parameters from Table 4.3 and the radiation image was simulated. The magnetic geometry is required by SOFT for the calculation. A quadratic q-profile was assumed, with constants chosen to resemble the q-profile at the final time step as calculated by DREAM.

The evolution of the plasma parameters as a function of normalized radius is shown in Figure 4.23. The passing of time is indicated by the colour going from dark to light. The temperature evolution is shown in Figure 4.23a. The exponential decay phase lasts until the temperature reaches 100 eV in the centre. Until this point, the shape of the profiles does not change, as the

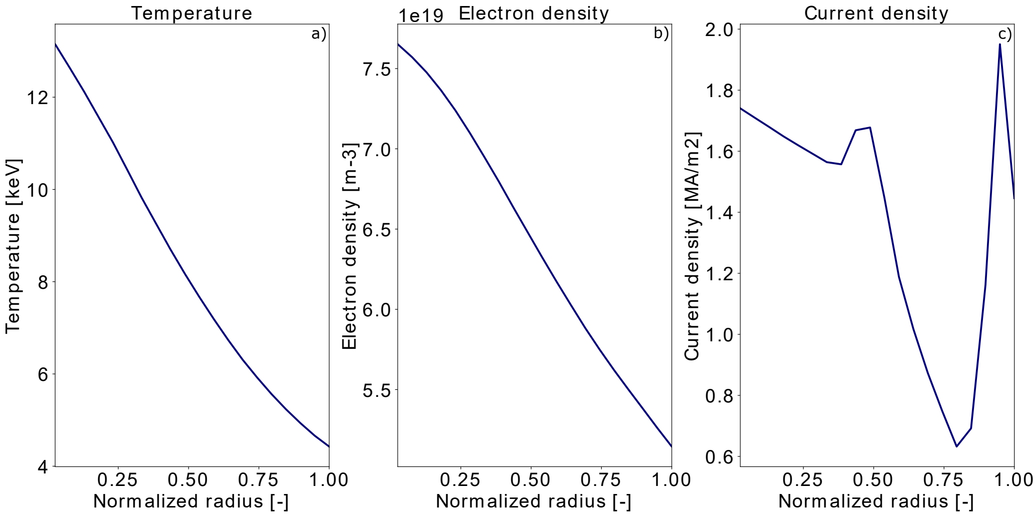

Figure 4.22: *The initial profiles used in DREAM. The first two graphs show the electron density and temperature. The final panel shows the current density profile taken from the EFIT simulation. DREAM was run with a limited radial resolution and the interpolation from the EFIT data caused the current density to be shaped as such.*

exponential decay is identical at every radial point. In the self-consistent temperature evolution phase, the profile shape breaks up, but the plasma eventually cools down to a few eV at every point. The cooling is slower at around 0.6 to 0.8 normalized radius.

It can be seen in Figure 4.23b and d that the electric field will be increased the most at these points. Plot b shows the electric field, while plot (d) shows the normalized electric field. The overall shape of the two plots is the same, as the critical electric field was similar at all radial points. The electric field is induced due to the decay of current. The evolution of the current density is shown in Figure 4.23c. The initial peak in current density at the edge of the plasma quickly decays inducing a large electric field at this region.

The final plot, 4.23e shows the time evolution of the total plasma current. The different phases described above are indicated by different shaded colours. The ionization phase is too short to be visible on the graph, and the initialization phase was omitted as it holds no relevant physical results on the current, and it dominates the timescale compared to the disruption length. The initial plasma current drops to a stable 3.7 MA in about 1 ms consisting entirely of runaway electrons. The runaway plateau phase lasts significantly longer in disruptions than the current quench, see Figure 2.4, so no decay of the runaway current can be seen on this plot.

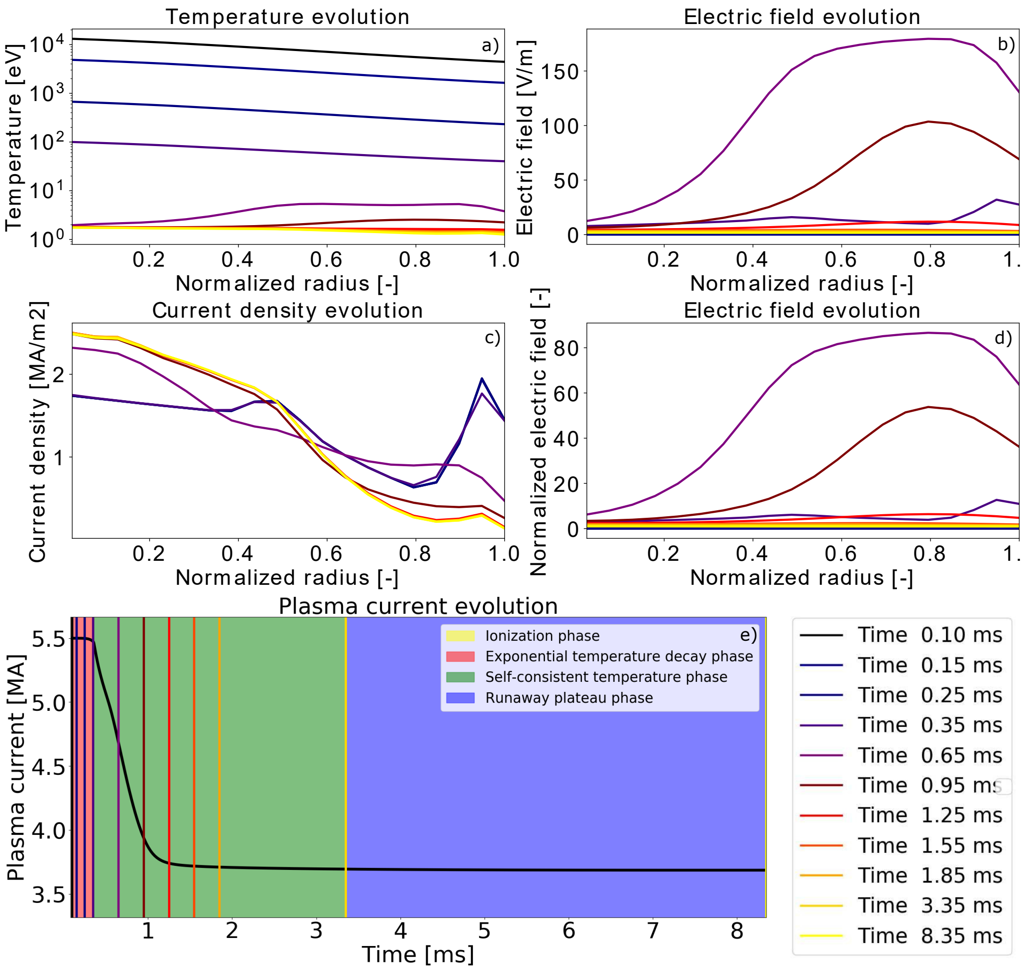

Figure 4.23: *The evolution of the plasma parameters during the JT-60SA-like disruption simulated by DREAM. Graph (a) shows the temperature evolution. The exponential decay phase can be seen to decrease the temperature at every radial point without changing the shape of the profile. The self-consistent temperature phase starts then the centre of the plasma cooled to* 100 *eV. The electric field is shown on graph (b) and the normalized electric field is on (d). The maximum of the electric field is located at the edge of the plasma. The current density is shown in plot (c). The initial peak at the edge relaxes leading to a profile peaked at the center. The evolution of the total current is shown at the bottom of plot (e). The simulation phases are indicated with shaded areas, with the ionization phase not visible before the exponential temperature decay phase and the initialization phase omitted. The colour coding of the lines indicates the passage of time going from dark to light.*

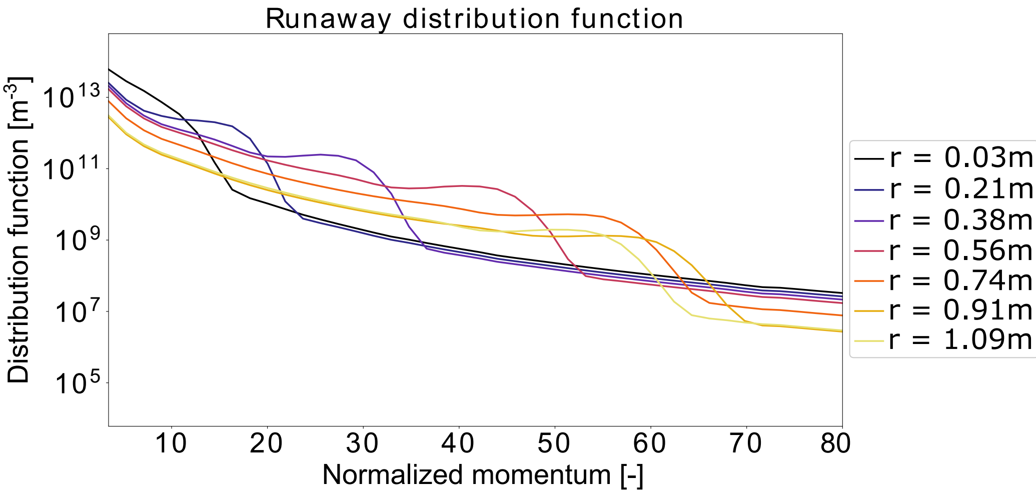

Figure 4.24: *The angle averaged runaway electron distribution function as a function of momentum normalized to $m_e c$ at the final time step of DREAM. The colours going from dark to light show the distribution function at different radial locations going from the centre to the edge.*

The runaway electron distribution function is used to calculate the radiation in SOFT. It is plotted in Figure 4.24 as a function of momentum normalized to $\mathrm{m_e c}$. The different colours correspond to different radial locations, going from the centre indicated by dark colours to the edge shown in lighter colours. The peaks indicated at each radial location are the runaway electron population generated by hot-tail generation and accelerated by different amounts by the electric field. The distribution function does not approach zero after the peaks as the avalanche collision operator generates runaway electrons isotropically on the runaway momentum grid in DREAM. It can be seen that the most energetic particle population is located o further out from the plasma centre, namely at $r = 0.91$ m corresponding to about 0.77 normalized radius. In Figure 4.23 it is shown that the electric field is peaked around this location, generating a higher energy electron population.

The synchrotron radiation is strongly dependent on the particle energy, so the radiation spot will dominantly come from the edge runaway electrons, compared to the electron at the magnetic axis, where the particles only reached about $10 - 20$ $\mathrm{m_e c}$. The outer population reached a maximum of 65 $\mathrm{m_e c}$ or 33 MeV energy.

The location in momentum space most contributing to the radiation image can be identified by the Green's function weighted by the distribution function, shown in Figure 4.25. It shows the contribution to the radiation

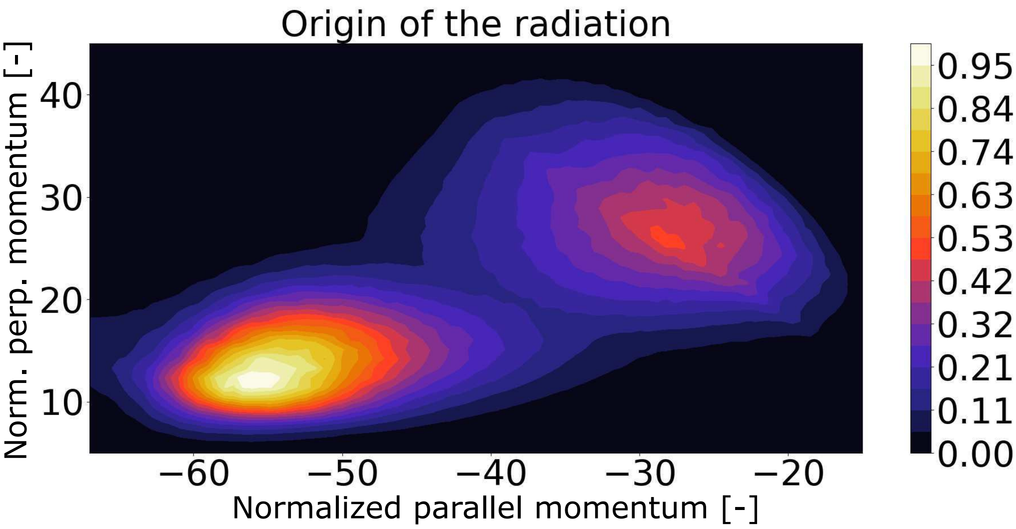

Figure 4.25: *The angle averaged runaway electron distribution function as a function of momentum normalized to $m_e c$ at the final time step of DREAM. The colours going from dark to light show the distribution function at different radial locations going from the centre to the edge.*

intensity from different regions on the momentum space normalized to the maximum value. The Green's function contains the geometry of the tokamak and the momentum dependence of the radiation. The component of the particle momentum parallel to the magnetic field lines, normalized to $m_e c$, is on the x-axis, while the normalized perpendicular momentum is on the vertical axis. The radiation originates from two separate local maxima, one located at $p_{\|} = 27, p_{\perp} = 27$ and the other at $p_{\|} = 57, p_{\perp} = 12$. The two locations are most connected by a ridge with a local minimum, the latter most likely resulting from the low radial resolution used in DREAM, and the interpolation done by SOFT. The plot clearly shows the two dependence of the radiation: the particle energy and the pitch angle, i.e. the ratio of the perpendicular and parallel momenta. The high-energy particle population dominates the radiation spot, while the lower-energy particles in the center can only contribute with higher pitch angles.

The radiation image as simulated by SOFT is shown in Figure 4.26, plotted onto the simulated camera view shown in Figure 4.20. SOFT simulates a rectangular detector in the field of view, with a given pixel resolution. The resulting picture was inserted into the field of view of the camera. The radiation shows a hollow spot, dominantly originating off-axis, where the runaway electron population reaches higher energies. It is located on the high field

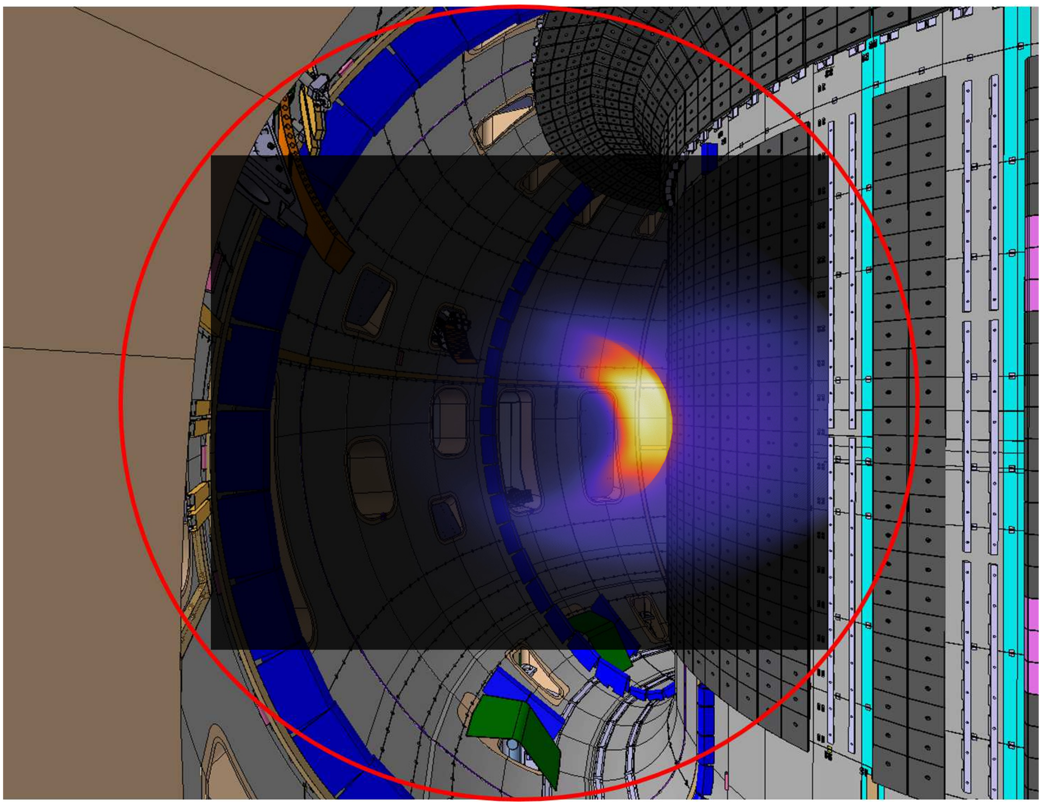

Figure 4.26: *The radiation from a runaway electron population on JT-60SA during a disruption. The image simulated by SOFT (black rectangle) was inserted on the simulated camera view of Figure 4.20.*

side of the tokamak, as the larger magnetic field enhances the synchrotron radiation effects.

The JT-60SA integrated commissioning campaign was completed at the beginning of 2024 [139], where the EDICAM system was operational [140]. Runaway electrons were present in some of the discharges where the EDICAM detected their presence through hard x-ray (HXR) radiation [141]. The high energy photons generate an increased hot pixel density on the Complementary metal oxide semiconductor (CMOS) sensor, hence enabling the detection of HXR photons, typically generated by runaway electron - wall interactions.

In the same discharge, EDICAM also detected synchrotron radiation from runaway electrons [141]. The synchrotron radiation was preceded by large HXR flashes, indicating the presence of runaway electrons in the discharge. The synchrotron radiation image seen by the EDICAM shows a close resemblance to the synthetic image calculated by SOFT, shown in Figure 4.26.

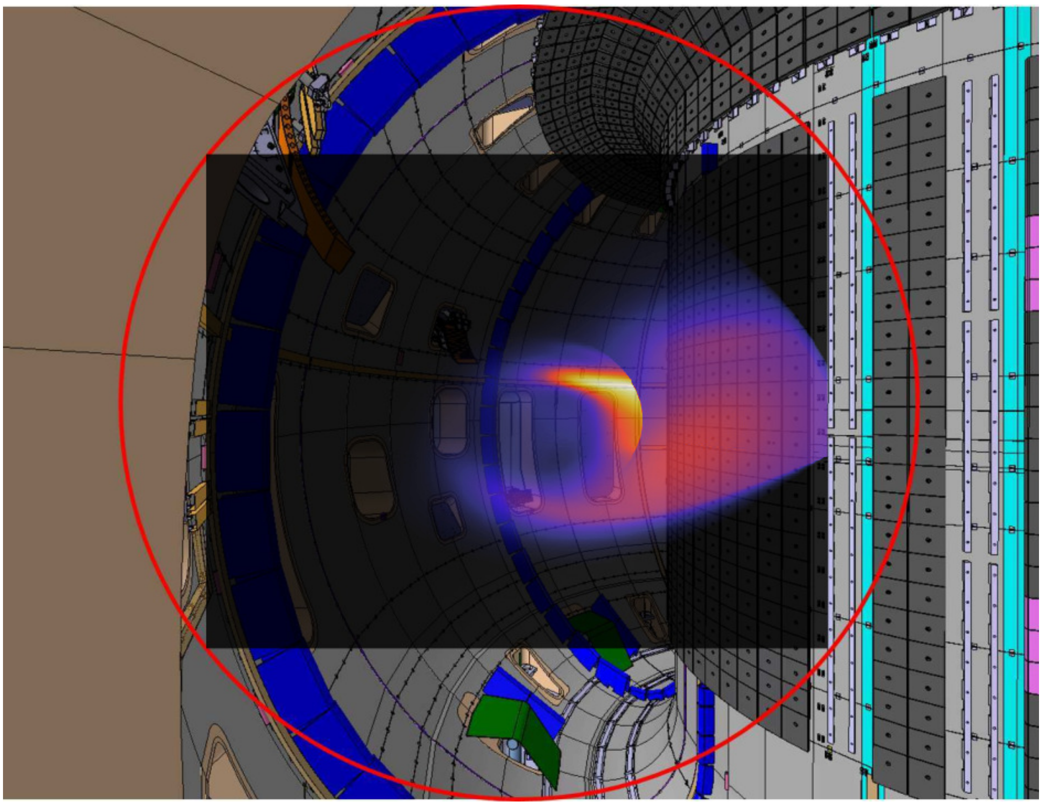

Figure 4.27: *The synthetic synchrotron radiation image of the scattered runaway electron population [142].*

The radiation is coming from the high field side of the tokamak and has a crescent shape, with a dark spot on the magnetic axis. These similarities are encouraging but further investigation is required to understand the phenomena seen by EDICAM in the experiment. One significant difference between the experimental image and 4.26 is in front of the central solenoid, where EDICAM saw stronger radiation in the experiment.

The HXR flashes prior to the synchrotron radiation and the more intense radiation in front of the central solenoid indicate pitch angle scattering in the runaway electron population due to some instability. This idea was further investigated by generating synchrotron images from pitch angle scattered runaway electron population. The high energy part of the runaway electron distribution function was artificially distributed isotropically on pitch angles between 0 deg and 90 deg with particle numbers conserved. The resulting radiation image is shown in Figure 4.27 [142].

We can see the radiation from the central solenoid is more prominent now, showing a closer resemblance to the EDICAM images during the experiment. The crescent shape of the radiation is less dominant than it was in Figure 4.26. To achieve a closer resemblance to the experimental observation, further simulations are planned with experimental inputs from JT-60SA discharges. The acquisition of the data is in progress.

Chapter 5

Summary and Outlook

Runaway electrons pose a serious threat to the safety of tokamak-type fusion devices. They can be generated due to the unique collisional properties between charged particles in fusion plasmas, where the particle population is more energetic than the thermal population experiences reduced drag force due to collisions. An applied electric field can easily accelerate this high-energy population given it is larger than the minimum collisional drag force acting on the population.

The resulting particles gain relativistic energies on short timescales and become runaway electrons. Runaway electron generation typically happens in non-optimal tokamak operations, such as the uncontrolled termination of a tokamak plasma called disruption or the formation of the plasma, when the density is yet low, but large electric fields can be present to ensure sufficient ionization. The generated high energy beam can pose a serious threat to the plasma-facing components if unconfined, causing melting of the first wall, or a localized beam can penetrate the cooling pipes of the superconducting coils and the first wall.

Future high-current devices are at extreme risk due to the exponential dependence of runaway electron population on plasma current. Runaway electron generation hence has been extensively studied both experimentally and in modeling tools, with a recent focus on the mitigation and prevention of runaway electron generation. The present work aims to contribute to the modeling of the runaway electron problem, focusing on the runaway electron generation during disruptions.

This work utilized the integrated modeling concept for the simulation of fusion plasmas. This approach aims to develop modular workflows for complex physical simulations, where the subsets of the physical problems are handled by separate models and these models are coupled together. The easy communication between the various models is ensured by a standardized data structure for the physical quantities, which can be reached by every code integrated into the framework. The tools developed in this approach are graphical workflows created in Kepler where the codes are turned into actors and coupled together.

The main advantage of this concept besides the inherent modularity is the ensured identical initialization of the different actors inside the workflows as the same input is provided to each code. The integrated modeling frameworks also allow the importation of experimental data into standardized data structures. This enables easy benchmarking and comparison of different models and validation of codes directly against experimental results. This aspect was utilized by the development of a dedicated Runaway Electron Test Workflow in the European Integrated Modeling (EU-IM) framework to study the accuracy of analytic runaway electron models compared to the computationally more expensive kinetic codes. The NORSE kinetic solver with a non-linear collision operator was integrated into the EU-IM framework to compare the already added Runaway Fluid analytic code to the kinetic results during rapidly changing plasma evolution. The workflow results were complemented by the LUKE bounce averaged Fokker-Planck solver using a linearized collision operator and the DREAM disruption simulating kinetic solver using a linearized test particle operator.

It was found that the analytic solvers underestimate the Dreicer generation rate of runaway electrons if the change in plasma parameters happens on a short timescale. In such cases, the immediate behavior of the electron distribution function produces a large temporary runaway electron generation which cannot be accurately described by analytic formulas. The minimum timescale where the analytic solvers are not usable was given in terms of the electron-electron collision times at the critical velocity of runaway electron generation. This quantity is easily calculable and can be used to determine the necessity of kinetic solvers in simulations and integrated modeling tools.

Integrated modeling frameworks have dominantly utilized fluid, otherwise called reduced-kinetic runaway electron models. Kinetic modeling of runaway electron dynamics can describe phenomena which cannot be described by fluid models. The capabilities of integrated modeling were extended by the addition of two kinetic models. The NORSE kinetic solver was added to the EU-IM framework and it was used in a dedicated workflow to study the Dreicer generation of runaway electrons. NORSE utilizes a non-linear collision operator to be able to describe scenarios where a significant portion of the electron population is converted to runaway electrons. In such cases, the interaction between the runaway electron population and the bulk electrons can be significant.

The DREAM disruption runaway electron model is capable of self-consistent simulation of tokamak disruptions with the calculation of background plasma parameters and fully or partially kinetic treatment of the electron population. It was integrated into the ITER Modeling and Analysis Suite (IMAS). The integration of DREAM was tested by a disruption simulation starting directly from experimental results imported from the TCV tokamak, demonstrating the capabilities of direct validation against experiments.

The main workflow developed in the integrated modeling frameworks is the European Transport Simulator (ETS). ETS is a 1.5-D transport simulator solving 1-D transport equations at the core plasma while treating the equilibrium and the edge plasma in 2-D. It was developed to simulate flat-top tokamak discharges including particle and heat transport, impurity evolution, radiation effects, equilibrium evolution and runaway electron generation. The latter is calculated by the fluid models Runaway Fluid and Runaway Indicator.

ETS was used to simulate a self-consistent tokamak disruption based on the ASDEX Upgrade shot 33108. The experimental data was imported into the EU-IM framework and was used in the ETS5 version in a simulation in two phases. First, the input data was completed in an interpretative to ensure the consistency of the data for a self-consistent disruption simulation. The disruption in the experiment was induced by the injection of a large quantity of argon gas, called massive gas injection (MGI). This was simulated in ETS5 and the the runaway electron generation was demonstrated.

Further simulations were performed with the ETS version developed in the IMAS framework. ETS6 follows the same concepts as ETS5. The same experimental data was imported into the IMAS framework and both the interpretative and self-consistent simulations were run. The time evolution of the plasma current was benchmarked against the ASTRA-STRAHL integrated modeling tool and the experimentally measured current evolution. The instability of ETS6 prevented full simulation of the runaway electron plateau, but the current decay timescale was found to be in good agreement.

Finally the feasibility of the Event Detection Intelligent Camera (EDICAM) visibly diagnostics for runaway electron detection as assessed. EDICAM is installed on JT-60SA and a disruption was simulated by the DREAM code for the geometry of this tokamak. The initial scenario was based on the JT-60SA research plan with a large plasma current. This scenario was chosen to ensure a large runaway electron population after the argon MGI-induced disruption so the radiation calculated by the SOFT synthetic diagnostic framework is optimal for the EDICAM system. The parameters of the EDICAM were given to the SOFT model with the runaway electron distribution function and the radiation of the produced runaway electron beam was calculated as seen by the EDICAM system, hence demonstrating the applicability of the camera for runaway electron purposes.

Chapter 6

Thesis statements

I. Statement

I created a workflow in the European Integrated Modeling Framework (EU-IM) to study the effects of rapidly changing electric fields on the Dreicer generation of runaway electrons. The workflow consists of a non-linear kinetic solver (NORSE) and a quasi-stationary analytic solver (Runaway Fluid). The results were complemented with a bounce-averaged kinetic solver (LUKE) and a linearized kinetic solver (DREAM). I have determined a time scale for the change of the electric field, on which kinetic solvers are required to accurately simulate the runaway electron dynamics. I have connected this time scale to the collision time of electrons taken at the critical velocity required for runaway electron generation. I found that analytic solvers cannot be used to accurately capture the evolution of runaway electrons for simulations shorter than this time scale.

II. Statement

I developed the kinetic modeling of runaway electrons in integrated modeling frameworks. I have integrated the NORSE non-linear kinetic code into the European Integrated Modeling Framework (EU-IM) into a benchmark workflow and used it in successful simulations. I have also integrated the DREAM kinetic model into the ITER modeling framework (IMAS) and enabled direct simulations with experimental inputs. I demonstrated this by simulating a discharge with experimental inputs from the TCV tokamak.

III. Statement

I created a physical model to simulate self-consistent massive material injection (MMI) induced disruptions with the European Transport Simulator (ETS) workflow to reproduce experimental results from disruptions. I demonstrated the capabilities of integrated modeling tools with the ETS version developed in the European Integrated Modeling Framework (EU-IM) and acquired physically relevant results. I have used the new ETS version, developed in the ITER modeling framework (IMAS) to benchmark the workflow against another integrated modeling code (ASTRA-STRAHL) and validate against experimental results with partially positive results.

IV. Statement

I simulated a disruption for the JT-60SA tokamak with the DREAM self-consistent kinetic code and used the results to model the expected radiation from the generated runaway electron beam with the SOFT synthetic synchrotron diagnostic framework. SOFT used the parameters of the Event Detection Intelligent Camera (EDICAM) visible camera system installed on the JT-60SA to estimate the radiation image as seen by the camera during a disruption. I found that the EDICAM system can be used to detect runaway electrons during disruptions. Later, signs of synchrotron radiation were indeed found.

Acknowledgments

Current work was financed by the Hungarian state, as a state financed PhD scholarships, in compliance with Act CCIV of 2011 on National Higher Education, carried out within the Doctoral School of Physical Sciences at the Faculty of Natural Sciences of the Budapest University of Technology and Economics. The work was also supported by the National Research, Development and Innovation Office (NKFIH) Grant FK132134. This work has been carried out within the framework of the EUROfusion Consortium, funded by the European Union via the Euratom Research and Training Programme (Grant Agreement No 101052200 — EUROfusion). Views and opinions expressed are however those of the author(s) only and do not necessarily reflect those of the European Union or the European Commission. Neither the European Union nor the European Commission can be held responsible for them. Furthermore, I have to give thanks to the Foundation for nuclear engineers (JNEA).

I have to thank a lot of people for making this PhD thesis possible, starting with my wife Szücs Cintia Lia, for the continuous support, and for starting a PhD with me, showing my that every PhD is difficult. I am most grateful for my family, my parents Olaszné Andrea and Olasz Tibor, for their unwavering encouragement over the years, even before starting this endeavor. I am also thankful to my siblings, Dóra, Niki and Bence, for their unending interest and support in my studies, even though they are as far from knowing physics as they possibly can :). I owe a lot of gratitude to my supervisor, Dr. Pokol Gergő, for his encouragement, discussions, ideas, and the occasional beer at various conference locations. I have to give thanks to Dr. Zoletnik Sándor for his support, especially at the end of my doctorate, making it possible to finish my thesis.

I am grateful for my colleagues at the Budapest University of Technology and Economics, Dr. Asztalos Örs, Balázs Péter for always being there when I had a question. I have to also thank Dr. Babcsány Boglárka, Dr. Pór

Gábor, Dr. Veres Gábor, Kovácsik Ákos, Aradi Mátyás and my current and former students, Lengyel Ferenc, Keszthelyi Gábor, Fehérvári Gergő, Pór Dániel and the NTI staff.

I am very grateful to my collegues from up north, starting with Dr. Mathias Hoppe, first from Chalmers University of Technology and now from KTH Royal Institute of Technology for his infinite patience, support, and for writing and supporting most of the codes I used in my work. Many thanks go to Dr. Tünde Fülöp, Dr. István Pusztai, and everyone at the Chalmers runaway electron team for the hospitality during my many visits and the many fruitful discussions over the years. I am very thankful to Dr. Pär Strand, Dmitriy Yadikin from Chalmers University of Technology, and to Dr. Thomas Jonsson from KTH Royal Institute of Technology for helping me in the struggle against ETS, and always being available for my questions.

I am thankful to my colleagues from the Centre for Energy Research for their help and collaboration, Dr. Réfy Dániel Imre, Dr. Szepesi Tamás, Dr. Vécsei Miklós, Dr. Cseh Gábor and of course the whole EK FPL Team. I would like to thank Dr. Gergely Papp, Dr. Eric Nardon and the TSVV 9 Team for the runaway electron discussions and Dr. David Coster, Dr. Irena Ivanova-Stanik, Jorge Ferreira and the WPCD Team for their insights into ETS. Finally I am thankful for my friends and family for the support.

Bibliography

[1] C. Allardice and E. R. Trapnell, *The first pile*. US Atomic Energy Commission. Technical Information Division, 1949, vol. 292.

[2] H. Hart, "Technological acceleration and the atomic bomb," *American Sociological Review*, vol. 11, no. 3, pp. 277–293, 1946.

[3] K. Young, "The hydrogen bomb, Lewis L. Strauss and the writing of nuclear history," *Journal of Strategic Studies*, vol. 36, no. 6, pp. 815–840, 2013. [Online]. Available: https://doi.org/10.1080/01402390.2012.726924

[4] J. Phillips, "Magnetic fusion," *Los Alamos Science*, pp. 64–67, 1983. [Online]. Available: https://library.sciencemadness.org/lanl1_a/lib-www/pubs/00285870.pdf

[5] E. A. Azizov, "Tokamaks: from A. D. Sakharov to the present (the 60-year history of tokamaks)," *Physics-Uspekhi*, vol. 55, no. 2, p. 190, feb 2012. [Online]. Available: https://dx.doi.org/10.3367/UFNe.0182.201202j.0202

[6] L. Spitzer, "The Stellarator Concept," *The Physics of Fluids*, vol. 1, no. 4, pp. 253–264, 07 1958. [Online]. Available: https://doi.org/10.1063/1.1705883

[7] J. Nuckolls, "Early steps toward inertial fusion energy (IFE) (1952 to 1962)," Tech. Rep., 6 1998. [Online]. Available: https://www.osti.gov/biblio/658936

[8] J. Nuckolls, L. Wood, A.Thiessen, and G. Zimmerman, "Laser compression of matter to super-high densities: thermonuclear (CTR) applications," *Nature*, vol. 239, p. 139–142, 1972.

[9] EUROFusion, *European Research Roadmap to the Realisation of Fusion Energy*, 2018. [Online]. Available: https://www.euro-fusion.org/fileadmin/user_upload/EUROfusion/Documents/2018_Research_roadmap_long_version_01.pdf

[10] ITER Oragnization, *ITER Research Plan within the Staged Approach*, sept 2018. [Online]. Available: https://www.iter.org/doc/www/content/com/Lists/ITER%20Technical%20Reports/Attachments/9/ITER_Research_Plan_within_the_Staged_Approach_levIII_provversion.pdf

[11] R. Kembleton, J. Morris, M. Siccinio, and F. Maviglia, "EU-DEMO design space exploration and design drivers," *Fusion Engineering and Design*, vol. 178, p. 113080, 2022. [Online]. Available: https://www.sciencedirect.com/science/article/pii/S0920379622000801

[12] S. D. Drell, "Nuclear radius and nuclear forces," *Phys. Rev.*, vol. 100, pp. 97–112, Oct 1955. [Online]. Available: https://link.aps.org/doi/10.1103/PhysRev.100.97

[13] IEAE, Atomic Mass Data Center, http://www-nds.iaea.org/amdc/. [Online]. Available: http://www-nds.iaea.org/amdc/

[14] G. H. Miley, H. Towner, and N. Ivich, "Fusion cross sections and reactivities," Illinois Univ., Urbana (USA), Tech. Rep. COO-2218-17, jun 1974.

[15] M. Kovari, M. Coleman, I. Cristescu, and R. Smith, "Tritium resources available for fusion reactors," *Nuclear Fusion*, vol. 58, no. 2, p. 026010, dec 2017. [Online]. Available: https://doi.org/10.1088%2F1741-4326%2Faa9d25

[16] L. J. Wittenberg, "Terrestrial sources of helium-3 fusion fuel - a trip to the center of the earth," *Fusion Technology*, vol. 15, no. 2P2B, pp. 1108–1113, 1989. [Online]. Available: https://doi.org/10.13182/FST89-A39841

[17] ——, *Non-lunar ^3He resources*, 1994, vol. UWFDM-967. [Online]. Available: https://fti.neep.wisc.edu/fti.neep.wisc.edu/pdf/fdm967.pdf

[18] I. Friedman, "Deuterium content of natural waters and other substances," *Geochimica et Cosmochimica Acta*, vol. 4, no. 1, pp. 89–103, 1953. [Online]. Available: https://www.sciencedirect.com/science/article/pii/0016703753900660

[19] K. Batani, "Perspectives on research on laser driven proton-boron fusion and applications," *Journal of Instrumentation*, vol. 18, no. 09, p. C09012, sep 2023. [Online]. Available: https://dx.doi.org/10.1088/1748-0221/18/09/C09012

[20] A. Tentori and F. Belloni, "Revisiting p-11b fusion cross section and reactivity, and their analytic approximations," *Nuclear Fusion*, vol. 63, no. 8, p. 086001, jun 2023. [Online]. Available: https://dx.doi.org/10.1088/1741-4326/acda4b

[21] G. Brochard, "Dynamics of ion-driven fishbones in tokamaks : theory and nonlinear full scale simulations," Ph.D. dissertation, 10 2019.

[22] P. Gierszewski, "Tritium supply for near-term fusion devices," *Fusion Engineering and Design*, vol. 10, pp. 399–403, 1989, proceedings of the First International Symposium on Fusion Nuclearf. [Online]. Available: https://www.sciencedirect.com/science/article/pii/0920379689900835

[23] M. Rubel, "Fusion neutrons: Tritium breeding and impact on wall materials and components of diagnostic systems," *Journal of Fusion Energy*, vol. 38, pp. 315–329, 2019.

[24] G. Federici, L. Boccaccini, F. Cismondi, M. Gasparotto, Y. Poitevin, and I. Ricapito, "An overview of the EU breeding blanket design strategy as an integral part of the DEMO design effort," *Fusion Engineering and Design*, vol. 141, pp. 30 – 42, 2019. [Online]. Available: http://www.sciencedirect.com/science/article/pii/S0920379619301590

[25] A. Raffray, M. Akiba, V. Chuyanov, L. Giancarli, and S. Malang, "Breeding blanket concepts for fusion and materials requirements," *Journal of Nuclear Materials*, vol. 307-311, pp. 21 – 30, 2002. [Online]. Available: http://www.sciencedirect.com/science/article/pii/S0022311502011741

[26] J. D. Lawson, "Some criteria for a power producing thermonuclear reactor," *Proceedings of the Physical Society. Section B*, vol. 70, no. 1, pp. 6–10, jan 1957. [Online]. Available: https://doi.org/10.1088%2F0370-1301%2F70%2F1%2F303

[27] A. E. Costley, "On the fusion triple product and fusion power gain of tokamak pilot plants and reactors," *Nuclear Fusion*, vol. 56, no. 6, p. 066003, apr 2016. [Online]. Available: https://doi.org/10.1088%2F0029-5515%2F56%2F6%2F066003

[28] E. I. Moses, "The National Ignition Facility (NIF): A path to fusion energy," *Energy Conversion and Management*, vol. 49, no. 7, pp. 1795–1802, 2008, iCENES'2007, 13th International Conference on Emerging Nuclear Energy Systems, June 3–8, 2007, İstanbul, Turkiye.

[Online]. Available: https://www.sciencedirect.com/science/article/pii/S0196890407004232

[29] A. B. Zylstra, A. L. Kritcher, O. A. Hurricane, D. A. Callahan, K. Baker, T. Braun *et al.*, "Record energetics for an inertial fusion implosion at NIF," *Phys. Rev. Lett.*, vol. 126, p. 025001, Jan 2021. [Online]. Available: https://link.aps.org/doi/10.1103/PhysRevLett.126.025001

[30] P. M. Bellan, *Fundamentals of Plasma Physics*. Cambridge University Press, 2006. [Online]. Available: https://www.cambridge.org/core/books/fundamentals-of-plasma-physics/4E88EC98AA7339A290AD0734641A7970

[31] G. McCracken and P. Stott, "Chapter 9 - tokamaks," in *Fusion (Second Edition)*, second edition ed., G. McCracken and P. Stott, Eds. Boston: Academic Press, 2013, pp. 91–105. [Online]. Available: https://www.sciencedirect.com/science/article/pii/B978012384656300009X

[32] J. Wesson, *Tokamaks, Third edition*. Oxford University Press, 2004.

[33] J. P. Freidberg, *Ideal MHD*. Cambridge University Press, 2014.

[34] F. Wagner, "The physics of magnetic confinement," *EPJ Web of Conferences*, vol. 54, 06 2013.

[35] T. Klinger, T. Andreeva, S. Bozhenkov, C. Brandt, R. Burhenn, B. Buttenschön *et al.*, "Overview of first Wendelstein 7-X high-performance operation," *Nuclear Fusion*, vol. 59, no. 11, p. 112004, jun 2019. [Online]. Available: https://doi.org/10.1088%2F1741-4326%2Fab03a7

[36] M. Wanner, V. Erckmann, J.-H. Feist, W. Gardebrecht, D. Hartmann, R. Krampitz *et al.*, "Status of WENDELSTEIN 7-X construction," *Nuclear Fusion*, vol. 43, no. 6, p. 416, may 2003. [Online]. Available: https://dx.doi.org/10.1088/0029-5515/43/6/304

[37] P. Helander and D. J. Sigmar, *Collisional Transport in Magnetized Plasmas*. Cambridge University Press, 2002.

[38] P. Helander, H. Smith, T. Fülöp, and L.-G. Eriksson, "Electron kinetics in a cooling plasma," *Physics of Plasmas*, vol. 11, pp. 5704–5709, 2004.

[39] M. N. Rosenbluth, W. M. MacDonald, and D. L. Judd, "Fokker-Planck equation for an inverse-square force," *Phys. Rev.*, vol. 107, pp. 1–6, Jul

1957. [Online]. Available: https://link.aps.org/doi/10.1103/PhysRev.107.1

[40] J. Connor and R. Hastie, "Relativistic limitations on runaway electrons," *Nuclear Fusion*, vol. 15, no. 3, p. 415, jun 1975. [Online]. Available: https://dx.doi.org/10.1088/0029-5515/15/3/007

[41] A. Stahl, E. Hirvijoki, J. Decker, O. Embréus, and T. Fülöp, "Effective critical electric field for runaway-electron generation," *Phys. Rev. Lett.*, vol. 114, p. 115002, Mar 2015. [Online]. Available: https://link.aps.org/doi/10.1103/PhysRevLett.114.115002

[42] A. Stahl, M. Landreman, O. Embréus, and T. Fülöp, "NORSE: A solver for the relativistic non-linear Fokker–Planck equation for electrons in a homogeneous plasma," *Computer Physics Communications*, vol. 212, pp. 269–279, 2016. [Online]. Available: http://arxiv.org/abs/1608.02742

[43] H. Dreicer, "Electron and Ion Runaway in a Fully Ionized Gas. I," *Phys. Rev.*, vol. 115, pp. 238–249, Jul 1959. [Online]. Available: https://link.aps.org/doi/10.1103/PhysRev.115.238

[44] ——, "Electron and Ion Runaway in a Fully Ionized Gas. II," *Phys. Rev.*, vol. 117, pp. 329–342, Jan 1960. [Online]. Available: https://link.aps.org/doi/10.1103/PhysRev.117.329

[45] A. A. Solodov and R. Betti, "Stopping power and range of energetic electrons in dense plasmas of fast-ignition fusion targets," *Physics of Plasmas*, vol. 15, no. 4, p. 042707, 04 2008. [Online]. Available: https://doi.org/10.1063/1.2903890

[46] L. Hesslow, O. Embréus, M. Hoppe, T. C. DuBois, G. Papp, M. Rahm *et al.*, "Generalized collision operator for fast electrons interacting with partially ionized impurities," *Journal of Plasma Physics*, vol. 84, p. 905840605, 2018. [Online]. Available: http://arxiv.org/abs/1807.05036

[47] L. Hesslow, L. Unnerfelt, O. Vallhagen, O. Embréus, M. Hoppe, G. Papp *et al.*, "Evaluation of the Dreicer runaway growth rate in the presence of high-Z impurities using a neural network," *Journal of Plasma Physics*, vol. 85, p. 475850601, 2019. [Online]. Available: https://arxiv.org/abs/1910.00356

[48] S. Chiu, M. Rosenbluth, R. Harvey, and V. Chan, "Fokker-Planck simulations mylb of knock-on electron runaway avalanche and bursts in

tokamaks," *Nuclear Fusion*, vol. 38, no. 11, p. 1711, nov 1998. [Online]. Available: https://dx.doi.org/10.1088/0029-5515/38/11/309

[49] H. Smith, P. Helander, L.-G. Eriksson, and T. Fülöp, "Runaway electron generation in a cooling plasma," *Physics of Plasmas*, vol. 12, no. 12, p. 122505, 12 2005. [Online]. Available: https://doi.org/10.1063/1.2148966

[50] H. M. Smith and E. Verwichte, "Hot tail runaway electron generation in tokamak disruptions," *Physics of Plasmas*, vol. 15, no. 7, p. 072502, 07 2008. [Online]. Available: https://doi.org/10.1063/1.2949692

[51] J. Martín-Solís, A. Loarte, and M. Lehnen, "Formation and termination of runaway beams in ITER disruptions," *Nuclear Fusion*, vol. 57, p. 066025, 06 2017.

[52] J. Mailloux, N. Abid, K. Abraham, P. Abreu, O. Adabonyan, P. Adrich *et al.*, "Overview of JET results for optimising ITER operation," *Nuclear Fusion*, vol. 62, no. 4, p. 042026, jun 2022. [Online]. Available: https://dx.doi.org/10.1088/1741-4326/ac47b4

[53] L. Reali, M. Gilbert, M. Boleininger, and S. Dudarev, "Intense γ-photon and high-energy electron production by neutron irradiation: Effects of nuclear excitations on reactor materials," *PRX Energy*, vol. 2, p. 023008, Jun 2023. [Online]. Available: https://link.aps.org/doi/10.1103/PRXEnergy.2.023008

[54] M. Rosenbluth and S. Putvinski, "Theory for avalanche of runaway electrons in tokamaks," *Nuclear Fusion*, vol. 37, no. 10, p. 1355, oct 1997. [Online]. Available: https://dx.doi.org/10.1088/0029-5515/37/10/I03

[55] O. Embréus, A. Stahl, and T. Fülöp, "On the relativistic large-angle electron collision operator for runaway avalanches in plasmas," *Journal of Plasma Physics*, vol. 84, p. 905840102, 2018. [Online]. Available: https://arxiv.org/abs/1708.08779

[56] B. N. Breizman, P. Aleynikov, E. M. Hollmann, and M. Lehnen, "Physics of runaway electrons in tokamaks," *Nuclear Fusion*, vol. 59, no. 8, p. 083001, jun 2019. [Online]. Available: https://dx.doi.org/10.1088/1741-4326/ab1822

[57] V. Plyusnin, V. Kiptily, A. Shevelev, E. Khilkevitch, M. Brix, S. Gerasimov *et al.*, "Parameters and stability of runaway electron dominating discharge in JET with ITER-like wall," in *42nd EPS Conference on Plasma Physics, EPS 2015*, R. Bingham, W. Suttrop,

S. Atzeni, R. Foest, K. McClements, B. Gonçalves *et al.*, Eds. European Physical Society EPS, 2015. [Online]. Available: http://ocs.ciemat.es/EPS2015PAP/pdf/P2.127.pdf

[58] V. Plyusnin, C. Reux, V. Kiptily, G. Pautasso, J. Decker, G. Papp *et al.*, "Comparison of runaway electron generation parameters in small, medium-sized and large tokamaks—a survey of experiments in COMPASS, TCV, ASDEX-Upgrade and JET," *Nuclear Fusion*, vol. 58, no. 1, p. 016014, nov 2017. [Online]. Available: https://dx.doi.org/10.1088/1741-4326/aa8f05

[59] T. Sometani and N. Fujisawa, "Breakdown experiment on a tokamak," *Plasma Physics*, vol. 20, no. 11, p. 1101, nov 1978. [Online]. Available: https://dx.doi.org/10.1088/0032-1028/20/11/002

[60] H.-T. Kim, W. Fundamenski, A. C. C. Sips, and EFDA-JET Contributors, "Enhancement of plasma burn-through simulation and validation in JET," *Nuclear Fusion*, vol. 52, no. 10, p. 103016, sep 2012. [Online]. Available: https://dx.doi.org/10.1088/0029-5515/52/10/103016

[61] P. de Vries and Y. Gribov, "ITER breakdown and plasma initiation revisited," *Nuclear Fusion*, vol. 59, no. 9, p. 096043, aug 2019. [Online]. Available: https://dx.doi.org/10.1088/1741-4326/ab2ef4

[62] M. Hoppe, I. Ekmark, E. Berger, and T. Fülöp, "Runaway electron generation during tokamak start-up," *Journal of Plasma Physics*, vol. 88, p. 905880317, 2022. [Online]. Available: https://arxiv.org/abs/2203.09900

[63] C. Reux, V. Plyusnin, B. Alper, D. Alves, B. Bazylev, E. Belonohy *et al.*, "Runaway electron beam generation and mitigation during disruptions at JET-ILW," *Nuclear Fusion*, vol. 55, no. 9, p. 093013, aug 2015. [Online]. Available: https://dx.doi.org/10.1088/0029-5515/55/9/093013

[64] R. Nygren, T. Lutz, D. Walsh, G. Martin, M. Chatelier, T. Loarer *et al.*, "Runaway electron damage to the Tore Supra Phase III outboard pump limiter," *Journal of Nuclear Materials*, vol. 241-243, pp. 522–527, 1997. [Online]. Available: https://www.sciencedirect.com/science/article/pii/S002231159780092X

[65] G. F. Matthews, B. Bazylev, A. Baron-Wiechec, J. Coenen, K. Heinola, V. Kiptily *et al.*, "Melt damage to the JET ITER-like Wall and divertor,"

Physica Scripta, vol. 2016, no. T167, p. 014070, jan 2016. [Online]. Available: https://dx.doi.org/10.1088/0031-8949/T167/1/014070

[66] C. Reux, C. Paz-Soldan, P. Aleynikov, V. Bandaru, O. Ficker, S. Silburn *et al.*, “Demonstration of safe termination of megaampere relativistic electron beams in tokamaks,” *Phys. Rev. Lett.*, vol. 126, p. 175001, Apr 2021. [Online]. Available: https://link.aps.org/doi/10.1103/PhysRevLett.126.175001

[67] A. H. Boozer, “Theory of tokamak disruptions,” *Physics of Plasmas*, vol. 19, no. 5, p. 058101, 04 2012. [Online]. Available: https://doi.org/10.1063/1.3703327

[68] E. Nardon, K. Särkimäki, F. Artola, S. Sadouni, the JOREK team, and JET Contributors, “On the origin of the plasma current spike during a tokamak disruption and its relation with magnetic stochasticity,” *Nuclear Fusion*, vol. 63, no. 5, p. 056011, mar 2023. [Online]. Available: https://dx.doi.org/10.1088/1741-4326/acc417

[69] C. Sommariva, E. Nardon, P. Beyer, M. Hoelzl, G. Huijsmans, and JET Contributors, “Electron acceleration in a JET disruption simulation,” *Nuclear Fusion*, vol. 58, no. 10, p. 106022, aug 2018. [Online]. Available: https://dx.doi.org/10.1088/1741-4326/aad47d

[70] R. Mitteau, M. Sugihara, R. Raffray, S. Carpentier-Chouchana, H. Labidi, M. Merola *et al.*, “Lifetime analysis of the ITER first wall under steady-state and off-normal loads,” vol. T145, 2011, Conference paper. [Online]. Available: https://www.scopus.com/inward/record.uri?eid=2-s2.0-84857617427&doi=10.1088%2f0031-8949%2f2011%2fT145%2f014081&partnerID=40&md5=84fae81cec61a394eef1bf5d612ee5e2

[71] R. Pitts, S. Carpentier, F. Escourbiac, T. Hirai, V. Komarov, S. Lisgo *et al.*, “A full tungsten divertor for ITER: Physics issues and design status,” *Journal of Nuclear Materials*, vol. 438, pp. S48–S56, 2013, proceedings of the 20th International Conference on Plasma-Surface Interactions in Controlled Fusion Devices. [Online]. Available: https://www.sciencedirect.com/science/article/pii/S0022311513000160

[72] M. Lehnen, K. Aleynikova, P. Aleynikov, D. Campbell, P. Drewelow, N. Eidietis *et al.*, “Disruptions in ITER and strategies for their control and mitigation,” *Journal of Nuclear Materials*, vol. 463, pp. 39–48, 2015, pLASMA-SURFACE INTERACTIONS 21. [Online]. Available: https://www.sciencedirect.com/science/article/pii/S0022311514007594

[73] D. C. Pace, C. M. Cooper, D. Taussig, N. W. Eidietis, E. M. Hollmann, V. Riso *et al.*, "Gamma ray imager on the DIII-D tokamak," *Review of Scientific Instruments*, vol. 87, no. 4, p. 043507, 04 2016. [Online]. Available: https://doi.org/10.1063/1.4945566

[74] J. Cerovsky, O. Ficker, V. Svoboda, E. Macusova, J. Mlynar, J. Caloud *et al.*, "Progress in HXR diagnostics at GOLEM and COMPASS tokamaks," *Journal of Instrumentation*, vol. 17, no. 01, p. C01033, jan 2022. [Online]. Available: https://dx.doi.org/10.1088/1748-0221/17/01/C01033

[75] C. Paz-Soldan, C. M. Cooper, P. Aleynikov, D. C. Pace, N. W. Eidietis, D. P. Brennan *et al.*, "Spatiotemporal evolution of runaway electron momentum distributions in tokamaks," *Phys. Rev. Lett.*, vol. 118, p. 255002, Jun 2017. [Online]. Available: https://link.aps.org/doi/10.1103/PhysRevLett.118.255002

[76] A. Shevelev, E. Khilkevitch, S. Lashkul, V. Rozhdestvensky, S. Pandya, V. Plyusnin *et al.*, "Runaway electron studies with hard x-ray and microwave diagnostics in the FT-2 lower hybrid current drive discharges," *Nuclear Fusion*, vol. 58, no. 1, p. 016034, nov 2017. [Online]. Available: https://dx.doi.org/10.1088/1741-4326/aa8cea

[77] R. A. Tinguely, R. S. Granetz, M. Hoppe, and O. Embréus, "Spatiotemporal evolution of runaway electrons from synchrotron images in Alcator C-Mod," *Plasma Physics and Controlled Fusion*, vol. 60, no. 12, p. 124001, oct 2018. [Online]. Available: https://dx.doi.org/10.1088/1361-6587/aae6ba

[78] M. Hoppe, O. Embréus, C. Paz-Soldan, R. Moyer, and T. Fülöp, "Interpretation of runaway electron synchrotron and bremsstrahlung images," *Nuclear Fusion*, vol. 58, no. 8, p. 082001, jun 2018. [Online]. Available: https://dx.doi.org/10.1088/1741-4326/aaae15

[79] T. Wijkamp, A. Perek, J. Decker, B. Duval, M. Hoppe, G. Papp *et al.*, "Tomographic reconstruction of the runaway distribution function in TCV using multispectral synchrotron images," *Nuclear Fusion*, vol. 61, no. 4, p. 046044, mar 2021. [Online]. Available: https://dx.doi.org/10.1088/1741-4326/abe8af

[80] A. Tema Biwole, L. Porte, S. Coda, A. Fasoli, and T. Team, "Vertical electron cyclotron emission diagnostic on the tokamak à configuration

variable," *Review of Scientific Instruments*, vol. 94, no. 10, p. 103504, 10 2023. [Online]. Available: https://doi.org/10.1063/5.0156000

[81] B. Esposito, J. Martín-Solís, F. Poli, J. Mier, R. Sánchez, and L. Panaccione, "Dynamics of high energy runaway electrons in the Frascati Tokamak Upgrade," *Physics of Plasmas*, vol. 10, no. 6, pp. 2350–2360, 2003. [Online]. Available: https://doi.org/10.1063/1.1574328

[82] M. Rabinski, L. Jakubowski, K. Malinowski, M. Sadowski, J. Zebrowski, M. Jakubowski *et al.*, "Development of a Cherenkov-type diagnostic system to study runaway electrons within the COMPASS tokamak," *Journal of Instrumentation*, vol. 12, no. 10, p. C10014, oct 2017. [Online]. Available: https://dx.doi.org/10.1088/1748-0221/12/10/C10014

[83] R. Kwiatkowski, M. Rabinski, M. J. Sadowski, J. Zebrowski, P. Karpinski, COMPASS *et al.*, "Cherenkov probes and runaway electrons diagnostics," 2021.

[84] G. Rattá, J. Vega, A. Murari, D. Gadariya, and J. Contributors, "PHAD: a phase-oriented disruption prediction strategy for avoidance, prevention, and mitigation in JET," *Nuclear Fusion*, vol. 61, no. 11, p. 116055, oct 2021. [Online]. Available: https://dx.doi.org/10.1088/1741-4326/ac2637

[85] A. Murari, M. Lungaroni, M. Gelfusa, E. Peluso, J. Vega, and J. Contributors, "Adaptive learning for disruption prediction in non-stationary conditions," *Nuclear Fusion*, vol. 59, no. 8, p. 086037, jul 2019. [Online]. Available: https://dx.doi.org/10.1088/1741-4326/ab1ecc

[86] J. Vega, A. Murari, S. Dormido-Canto, G. Rattá, M. Gelfusa, and JET Contributors, "Disruption prediction with artificial intelligence techniques in tokamak plasmas," *Nature Physics*, vol. 18, no. 7, pp. 741–750, 2022.

[87] N. Eidietis, W. Choi, S. Hahn, D. Humphreys, B. Sammuli, and M. Walker, "Implementing a finite-state off-normal and fault response system for disruption avoidance in tokamaks," *Nuclear Fusion*, vol. 58, no. 5, p. 056023, mar 2018. [Online]. Available: https://dx.doi.org/10.1088/1741-4326/aab62c

[88] U. Sheikh, B. Duval, C. Galperti, M. Maraschek, O. Sauter, C. Sozzi *et al.*, "Disruption avoidance through the prevention of ntm destabilization in tcv," *Nuclear Fusion*, vol. 58, no. 10, p. 106026, aug 2018. [Online]. Available: https://dx.doi.org/10.1088/1741-4326/aad924

[89] L. Baylor, "Disruption mitigation system developments and design for ITER," *Fusion Science and Technology*, vol. 68, 09 2015.

[90] T. Luce, U. Kruezi, M. Lehnen, S. Jachmich, M. De Bock, G. Ellwood *et al.*, "Progress on the ITER DMS design and integration 28th IAEA Fusion Energy Conf." TECH/1-4Ra](https://conference. iaea. org/event/214/contributions/), 2021.

[91] N. Commaux, D. Shiraki, L. Baylor, E. Hollmann, N. Eidietis, C. Lasnier *et al.*, "First demonstration of rapid shutdown using neon shattered pellet injection for thermal quench mitigation on DIII-D," *Nuclear Fusion*, vol. 56, p. 046007, 04 2016.

[92] O. Vallhagen, I. Pusztai, M. Hoppe, S. Newton, and T. Fülöp, "Effect of two-stage shattered pellet injection on tokamak disruptions," *Nuclear Fusion*, vol. 62, p. 112004, 2022. [Online]. Available: https://arxiv.org/abs/2201.10279

[93] L. Hesslow, O. Embréus, O. Vallhagen, and T. Fülöp, "Influence of massive material injection on avalanche runaway generation during tokamak disruptions," *Nuclear Fusion*, vol. 59, p. 084004, 2019. [Online]. Available: http://arxiv.org/abs/1904.00602

[94] S. Zoletnik, E. Walcz, S. Jachmich, U. Kruezi, M. Lehnen, G. Anda *et al.*, "Shattered pellet technology development in the ITER DMS test laboratory," *Fusion Engineering and Design*, vol. 190, p. 113701, 2023. [Online]. Available: https://www.sciencedirect.com/science/article/pii/S0920379623002843

[95] R. Yoshino and S. Tokuda, "Runaway electrons in magnetic turbulence and runaway current termination in tokamak discharges," *Nuclear Fusion*, vol. 40, no. 7, p. 1293, jul 2000. [Online]. Available: https://dx.doi.org/10.1088/0029-5515/40/7/302

[96] M. Lehnen, S. A. Bozhenkov, S. S. Abdullaev, and M. W. Jakubowski, "Suppression of runaway electrons by resonant magnetic perturbations in TEXTOR disruptions," *Phys. Rev. Lett.*, vol. 100, p. 255003, Jun 2008. [Online]. Available: https://link.aps.org/doi/10.1103/PhysRevLett.100.255003

[97] U. Sheikh, J. Decker, M. Hoppe, M. Pedrini, B. Sieglin, L. Simons *et al.*, "Benign termination of runaway electron beams on ASDEX Upgrade and TCV," *Plasma Physics and Controlled Fusion*, vol. 66, 01 2024.

[98] R. de Luca, P. Fanelli, S. Mingozzi, G. Calabrò, F. Vivio, F. Maviglia *et al.*, "Parametric design study of a substrate material for a DEMO sacrificial limiter," *Fusion Engineering and Design*, vol. 158, p. 111721, 2020. [Online]. Available: https://www.sciencedirect.com/science/article/pii/S0920379620302696

[99] C. Stefanini, P. Fanelli, R. De Luca, D. Paoletti, F. Vivio, V. Belardi *et al.*, "Parametric FE model for the thermal and hydraulic optimization of a Plasma Facing Component equipped with sacrificial lattice armours for First Wall limiter application in EU-DEMO fusion reactor," *Fusion Engineering and Design*, vol. 192, p. 113604, 2023. [Online]. Available: https://www.sciencedirect.com/science/article/pii/S0920379623001886

[100] G. I. Pokol, "Open Source Runaway Electron Physics (OSREP)," https://github.com/osrep.

[101] G. Falchetto, D. Coster, R. Coelho, B. Scott, L. Figini, D. Kalupin *et al.*, "The European Integrated Tokamak Modelling (ITM) effort: achievements and first physics results," *Nuclear Fusion*, vol. 54, no. 4, p. 043018, mar 2014. [Online]. Available: https://dx.doi.org/10.1088/0029-5515/54/4/043018

[102] M. Hoppe, O. Embreus, and T. Fülöp, "DREAM: A fluid-kinetic framework for tokamak disruption runaway electron simulations," *Computer Physics Communications*, vol. 268, p. 108098, 2021. [Online]. Available: https://arxiv.org/abs/2103.16457

[103] M. Hoppe, "DREAM github repository," https://github.com/chalmersplasmatheory/DREAM.

[104] M. Hoppe, O. Embréus, R. Tinguely, R. Granetz, A. Stahl, and T. Fülöp, "SOFT: a synthetic synchrotron diagnostic for runaway electrons," *Nuclear Fusion*, vol. 58, p. 026032, 2018. [Online]. Available: https://arxiv.org/abs/1709.00674

[105] M. Hoppe, "SOFT github repository," https://github.com/hoppe93/SOFT2.

[106] F. Imbeaux, J. Lister, G. Huijsmans, W. Zwingmann, M. Airaj, L. Appel *et al.*, "A generic data structure for integrated modelling of tokamak physics and subsystems," *Computer Physics Communications*, vol. 181, pp. 987–998, 02 2010.

[107] F. Imbeaux, S. Pinches, J. Lister, Y. Buravand, T. Casper, B. Duval *et al.*, “Design and first applications of the ITER integrated modelling and analysis suite,” *Nuclear Fusion*, vol. 55, no. 12, p. 123006, oct 2015. [Online]. Available: https://dx.doi.org/10.1088/0029-5515/55/12/123006

[108] http://kepler-project.org.

[109] p. Aleynikov and B. Breizman, “Theory of two threshold fields for relativistic runaway electrons,” *Physical Review Letters*, vol. 114, p. 155001, 2015. [Online]. Available: https://link.aps.org/doi/10.1103/PhysRevLett.114.155001

[110] E. Nilsson, J. Decker, Y. Peysson, R. Granetz, F. Saint-Laurent, and M. Vlainic, “Kinetic modelling of runaway electron avalanches in tokamak plasmas,” *Plasma Physics and Controlled Fusion*, vol. 57, no. 9, p. 095006, jul 2015. [Online]. Available: https://dx.doi.org/10.1088/0741-3335/57/9/095006

[111] M. Hoppe, “Runaway-electron model development and validation in tokamaks,” 2021. [Online]. Available: https://research.chalmers.se/publication/527630

[112] O. Linder, E. Fable, F. Jenko, G. Papp, G. Pautasso, the ASDEX Upgrade team *et al.*, “Self-consistent modeling of runaway electron generation in massive gas injection scenarios in ASDEX Upgrade,” *Nuclear Fusion*, vol. 60, no. 9, p. 096031, aug 2020. [Online]. Available: https://dx.doi.org/10.1088/1741-4326/ab9dcf

[113] M. Owsiak, M. Plociennik, B. Palak, T. Zok, C. Reux, L. D. Gallo *et al.*, “Running simultaneous Kepler sessions for the parallelization of parametric scans and optimization studies applied to complex workflows,” *Journal of Computational Science*, vol. 20, pp. 103–111, 2017. [Online]. Available: https://www.sciencedirect.com/science/article/pii/S1877750316304884

[114] S. Olasz, O. Embreus, M. Hoppe, M. Aradi, D. Por, T. Jonsson *et al.*, “Validity of models for Dreicer generation of runaway electrons in dynamic scenarios,” *Nuclear Fusion*, vol. 61, no. 6, p. 066010, apr 2021. [Online]. Available: https://dx.doi.org/10.1088/1741-4326/abf0de

[115] Y. Peysson and J. Decker, “Numerical simulations of the radio-frequency–driven toroidal current in tokamaks,” *Fusion Science and*

Technology, vol. 65, no. 1, pp. 22–42, 2014. [Online]. Available: https://doi.org/10.13182/FST13-643

[116] J. Decker, E. Hirvijoki, O. Embreus, Y. Peysson, A. Stahl, I. Pusztai *et al.*, "Numerical characterization of bump formation in the runaway electron tail," *Plasma Physics and Controlled Fusion*, vol. 58, no. 2, p. 025016, jan 2016. [Online]. Available: https://dx.doi.org/10.1088/0741-3335/58/2/025016

[117] G. I. Pokol, S. Olasz, B. Erdos, G. Papp, M. Aradi, M. Hoppe *et al.*, "Runaway electron modelling in the self-consistent core European Transport Simulator," *Nuclear Fusion*, vol. 59, no. 7, p. 076024, jun 2019. [Online]. Available: https://dx.doi.org/10.1088/1741-4326/ab13da

[118] P. Strand, D. Yadikin, J. Ferreira, A. Figueiredo, R. Coelho, E. Lerche *et al.*, "Towards a predictive modelling capacity for DT plasmas: European Transport Simulator (ETS) verification and validation," in *27th IAEA Fusion Energy Conference, Ahmedabad, India*, 2018.

[119] D. V. Eester and E. Lerche, "Simple 1D Fokker–Planck modelling of ion cyclotron resonance frequency heating at arbitrary cyclotron harmonics accounting for Coulomb relaxation on non-Maxwellian populations," *Plasma Physics and Controlled Fusion*, vol. 53, no. 9, p. 092001, jul 2011. [Online]. Available: https://dx.doi.org/10.1088/0741-3335/53/9/092001

[120] M. Romanelli, R. Coelho, D. Coster, J. Ferreira, L. Fleury, S. Henderson *et al.*, "Code integration, data verification, and models validation using the iter integrated modeling and analysis system (IMAS) in EUROfusion," *Fusion Science and Technology*, vol. 76, no. 8, pp. 894–900, 2020. [Online]. Available: https://doi.org/10.1080/15361055.2020.1819751

[121] H. Meyer, T. Eich, M. Beurskens, S. Coda, A. Hakola, P. Martin *et al.*, "Overview of progress in European medium sized tokamaks towards an integrated plasma-edge/wall solutiona," *Nuclear Fusion*, vol. 57, no. 10, p. 102014, jun 2017. [Online]. Available: https://dx.doi.org/10.1088/1741-4326/aa6084

[122] B. Wan, Y. Liang, X. Gong, J. Li, N. Xiang, G. Xu *et al.*, "Overview of EAST experiments on the development of high-performance steady-state scenario," *Nuclear Fusion*, vol. 57, no. 10, p. 102019, jul 2017. [Online]. Available: https://doi.org/10.1088%2F1741-4326%2Faa7861

[123] L. Xiaojuan and Z. Yu, "A data integration tool for the integrated modeling and analysis for EAST," *Fusion Engineering and Design*, vol. 195, p. 113933, 2023. [Online]. Available: https://www.sciencedirect.com/science/article/pii/S092037962300515X

[124] V. Mukhovatov, M. Shimada, A. N. Chudnovskiy, A. E. Costley, Y. Gribov, G. Federici *et al.*, "Overview of physics basis for ITER," *Plasma Physics and Controlled Fusion*, vol. 45, no. 12A, pp. A235–A252, nov 2003. [Online]. Available: https://doi.org/10.1088%2F0741-3335%2F45%2F12a%2F016

[125] D. Kalupin, V. Basiuk, P. Huynh, L. Alves, T. Aniel, J. F. Artaud *et al.*, "The European Transport Solver: an Integrated Approach for Transport Simulations in the Plasma Core," Sep 2012.

[126] D. Kalupin, I. Ivanova-Stanik, I. Voitsekhovitch, J. Ferreira, D. Coster, L. Alves *et al.*, "Numerical analysis of JET discharges with the European Transport Simulator," *Nuclear Fusion*, vol. 53, no. 12, p. 123007, nov 2013. [Online]. Available: https://doi.org/10.1088/0029-5515/53/12/123007

[127] M. Romanelli, P. Strand, D. Coster, J. Ferreira, D. Yadikin, T. Jonnson *et al.*, "Predictive multi-physics integrated modelling of tokamak scenarios using the ITER Integrated Modelling and Analysis Suite (IMAS) in support of ITER exploitation," in *28th IAEA Fusion Energy Conference (FEC 2020)*, 2021.

[128] K. Wongrach, K. Finken, S. Abdullaev, R. Koslowski, O. Willi, L. Zeng *et al.*, "Measurement of synchrotron radiation from runaway electrons during the TEXTOR tokamak disruptions," *Nuclear Fusion*, vol. 54, no. 4, p. 043011, mar 2014. [Online]. Available: https://dx.doi.org/10.1088/0029-5515/54/4/043011

[129] Z. Popović, E. M. Hollmann, D. del Castillo-Negrete, I. Bykov, R. A. Moyer, J. L. Herfindal *et al.*, "Polarized imaging of visible synchrotron emission from runaway electron plateaus in DIII-D," *Physics of Plasmas*, vol. 28, no. 8, p. 082510, 08 2021. [Online]. Available: https://doi.org/10.1063/5.0058927

[130] Y. Kamada, E. D. Pietro, M. Hanada, P. Barabaschi, S. Ide, S. Davis *et al.*, "Completion of JT-60SA construction and contribution to ITER," *Nuclear Fusion*, vol. 62, no. 4, p. 042002, mar 2022. [Online]. Available: https://dx.doi.org/10.1088/1741-4326/ac10e7

[131] G. Giruzzi, M. Yoshida, N. Aiba, J. F. Artaud, J. Ayllon-Guerola, O. Beeke *et al.*, "Advances in the physics studies for the JT-60SA tokamak exploitation and research plan," *Plasma Physics and Controlled Fusion*, vol. 62, no. 1, p. 014009, oct 2019. [Online]. Available: https://dx.doi.org/10.1088/1361-6587/ab4771

[132] S. Zoletnik, T. Szabolics, G. Kocsis, T. Szepesi, and D. Dunai, "EDICAM (Event Detection Intelligent Camera)," *Fusion Engineering and Design*, vol. 88, no. 6, pp. 1405–1408, 2013, proceedings of the 27th Symposium On Fusion Technology (SOFT-27); Liège, Belgium, September 24-28, 2012. [Online]. Available: https://www.sciencedirect.com/science/article/pii/S0920379613000641

[133] T. Szepesi, S. Davis, N. Hajnal, K. Kamiya, G. Kocsis, Ákos Kovácsik *et al.*, "Wide-angle visible video diagnostics for JT-60SA utilizing EDICAM," *Fusion Engineering and Design*, vol. 153, p. 111505, 2020. [Online]. Available: https://www.sciencedirect.com/science/article/pii/S0920379620300533

[134] S. Olasz, M. Hoppe, T. Szepesi, K. Kamiya, P. Balazs, and G. I. Pokol, "Feasibility of the EDICAM camera for runaway electron detection in JT-60SA disruptions," *Fusion Engineering and Design*, vol. 195, p. 113940, 2023. [Online]. Available: https://www.sciencedirect.com/science/article/pii/S0920379623005227

[135] L. Lao, H. S. John, R. Stambaugh, A. Kellman, and W. Pfeiffer, "Reconstruction of current profile parameters and plasma shapes in tokamaks," *Nuclear Fusion*, vol. 25, no. 11, p. 1611, nov 1985. [Online]. Available: https://dx.doi.org/10.1088/0029-5515/25/11/007

[136] C. Guillemaut, P. Drewelow, G. Matthews, A. Kukushkin, R. Pitts, P. Abreu *et al.*, "Main chamber wall plasma loads in JET-ITER-like wall at high radiated fraction," *Nuclear Materials and Energy*, vol. 12, pp. 234–240, 2017, proceedings of the 22nd International Conference on Plasma Surface Interactions 2016, 22nd PSI. [Online]. Available: https://www.sciencedirect.com/science/article/pii/S2352179116300977

[137] M. Takechi, S. Sakurai, K. Masaki, G. Matsunaga, and A. Sakasai, "Disruption simulations for JT-60SA design and construction," *Fusion Engineering and Design*, vol. 146, pp. 2738–2742, 2019, sI:SOFT-30. [Online]. Available: https://www.sciencedirect.com/science/article/pii/S0920379619306507

[138] M. Dibon, S. Nakamura, G. Matsunaga, A. Isayama, G. Phillips, C. Sozzi *et al.*, "Conceptual design of the MGI system for JT-60SA," *Fusion Engineering and Design*, vol. 176, p. 113042, 2022. [Online]. Available: https://www.sciencedirect.com/science/article/pii/S0920379622000424

[139] M. Yoshida and the JT-60SA Integrated Project Team, "Start-up of plasma operation and control in the large superconducting tokamak JT-60SA," in *50th EPS Conference on Plasma Physics, EPS 2024*, J. Kirk, L. Volpe, M. Reiffers, and P. Helfenstein, Eds. European Physical Society EPS, Jul 2024. [Online]. Available: https://lac913.epfl.ch/epsppd3/2024/html/TitlePage.html

[140] T. Szepesi, A. Buzás, G. Cseh, G. Kocsis, . Kovácsik, D. Réfy *et al.*, "Analysis of the first plasmas of JT-60SA using EDICAM video diagnostic," in *50th EPS Conference on Plasma Physics, EPS 2024*, J. Kirk, L. Volpe, M. Reiffers, and P. Helfenstein, Eds. European Physical Society EPS, Jul 2024. [Online]. Available: https://lac913.epfl.ch/epsppd3/2024/html/TitlePage.html

[141] D. Réfy, T. Szepesi, G. Kocsis, G. Cseh, A. Buzás, T. Szabolics *et al.*, "Hard X-ray dosimetry with the EDICAM visible CMOS camera," in *50th EPS Conference on Plasma Physics, EPS 2024*, J. Kirk, L. Volpe, M. Reiffers, and P. Helfenstein, Eds. European Physical Society EPS, Jul 2024. [Online]. Available: https://lac913.epfl.ch/epsppd3/2024/html/TitlePage.html

[142] S. Olasz, M. Hoppe, T. Szepesi, K. Kamiya, P. Balazs, G. Keszthelyi *et al.*, "Detection of runaway electron radiation at JT-60SA," in *Joint Runaway Electron Modelling (REM) and JET SPI Analysis meeting*, Jun 2024.